ABSTRACT

Title of Dissertation:	LASER WAKEFIELD ACCELERATOR EXPERIMENTS: COHERENT INJECTION RADIATION AND OPTICAL FIELD IONIZATION-BASED PLASMA WAVEGUIDES
	Bo Miao Doctor of Philosophy, 2020
Dissertation directed by:	Professor Howard Milchberg Department of Physics

Laser wakefield electron accelerators (LWFAs) can support accelerating gradients three orders of magnitude higher than conventional radio frequency linear accelerators, enabling compact laser-driven devices. In this dissertation, I explore two regimes of LWFA physics, one at high plasma density, and the other at low density.

The first part of this thesis characterizes bright broadband coherent radiation emitted during wakefield acceleration driven by femtosecond laser interaction with high, near-critical density plasma. Detailed measurement is presented of the radiation spectrum, polarization and angular distribution. The results are consistent with synchrotron radiation emission from laser-assisted injection into wakefields, with this picture supported by particle-in-cell simulations.

The second part of this thesis demonstrates the use of high intensity Bessel beams of various orders for generating low density plasma waveguides that guide high intensity laser pulses over tens of centimeters. Methods are presented for Bessel beam generation and focus optimization using adaptive optics.

LASER WAKEFIELD ACCELERATOR EXPERIMENTS: COHERENT INJECTION RADIATION AND OPTICAL FIELD IONIZATION-BASED PLASMA WAVEGUIDES.

by

Bo Miao

Dissertation submitted to the Faculty of the Graduate School of the
University of Maryland, College Park, in partial fulfillment
of the requirements for the degree of
Doctor of Philosophy
2020

Advisory Committee:
Professor Howard Milchberg, Chair
Professor James Drake
Professor Julius Goldhar
Professor Ki-Yong Kim
Professor Phillip Sprangle

Dedication

For Sihong

Acknowledgements

I would like to thank my advisor, Prof. Howard Milchberg for the opportunity to work and learn in his lab. Howard sets a role model by his scientific inspiration and pursuit of outstanding research. I am indebted to his invaluable mentorship, guidance and support.

This dissertation cannot be completed without the help from many brilliant lab colleagues and staffs. I am indebted to Dr. Andy Goers and Dr. George Hine for teaching me lab operation and maintenance. I am grateful for sharing the long nights of experiments, as well as the frustration and joy of discovery with Dr. Jared Wahlstrand, Dr. Fatholah Salehi, Linus Feder. I would like to thank Dr. Jennifer Elle, Dr. Nihal Jhajj , Dr. Eric Rosenthal, Dr. Sina Zahedpour, Ilia Larkin, Daniel Woodbury, Robert Schwartz, Scott Hancock for all the discussion and assistance. The newer lab members, Andrew Goffin, Manh Le, Lucas Railing and Jaron Shrock have demonstrated their creativity and potential as future scientists. I look forward to their exciting research.

I acknowledge the IREAP and facilities staff members, especially Jay Pyle, Nolan Ballew and Thomas Weimar for instructions on machining projects, Thomas Loughran for lithography, and Bryan Quinn for assistance in lab infrastructure maintenance.

Finally, I would like to thank my love, Sihong Yang, my parents Yukun Miao and Dongmei Zhao for their love and support without reservation.

Table of Contents

List of Figures

List of Abbreviations

LWFA	Laser Wakefield Acceleration
LINAC	Linear Accelerator
SSSI	Single-shot Supercontinuum Spectral Interferometry
SPP	Spiral Phase Plate
ER	Error Reduction
HIO	Hybrid Input-Output
DM	Deformable Mirror
SLM	Spatial Light Modulator
OFI	Optical Field Ionization

Chapter 1 Introduction

1.1 Motivation

Accelerator science and technology have made significant progress since the invention of cyclotrons by Ernest Lawrence in 1929 [1]. High energy particle beams from accelerators have been a workhorse not only in fundamental and applied research, but also in commercial and industrial applications. The Large Hadron Collider at CERN enables scientists to study and validate the Standard model [2]. Synchrotron radiation provides high-flux and ultrashort X-rays for a wide range of research, such as molecular crystallography [3] and nanotechnology. In the medical market, particle accelerators deliver high energy electrons, ions, and gamma rays for cancer treatment [4] and nuclear isotopes [5] for medical imaging [6].

Here we consider linear accelerators as an example. A standard linear accelerator (LINAC) consists of an array of plates or cavities, driven by phased AC electric fields typically supplied by high power radio frequency (RF) waves for the highest energy LINACs. The AC field (voltage) amplitude, phase and frequency is carefully controlled such that an electron bunch will be accelerated in successive cavities (see Figure 1.1(a)). The accelerating fields are limited to ~100 MV/m due to surface breakdown of the RF cavities. Therefore, high energy electron accelerators (>10 GeV) usually extend to over kilometers long, such as the Stanford Linear Accelerator (3.2 km) in Figure 1.1(b).

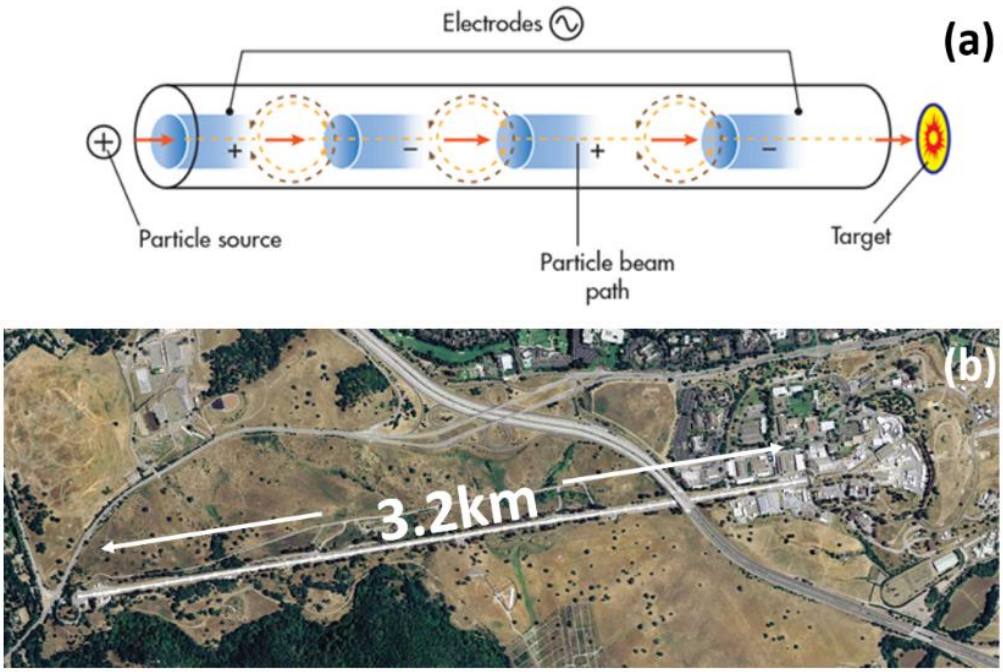

Figure 1.1 Working principle of a linear accelerator [7] (b) An aerial photo of SLAC [8]

One way to overcome this constraint is to use plasma as the acceleration medium, as it supports electric fields up to ~1TV/m, which is many orders of magnitude higher than RF accelerators. A plasma version of an RF cavity is realized by using the axial electrostatic field of relativistic plasma waves driven by lasers, as proposed by Tajima and Dawson in 1979 [9] and later extended by Sprangle *et al* [10].

In laser wakefield acceleration (LWFA), an intense laser pulse propagates through plasma and drives a plasma density perturbation with the ponderomotive force. The plasma wave propagates at the group velocity of the laser pulse and can trap and accelerate properly phased electrons to high energy, as shown in Figure 1.2.

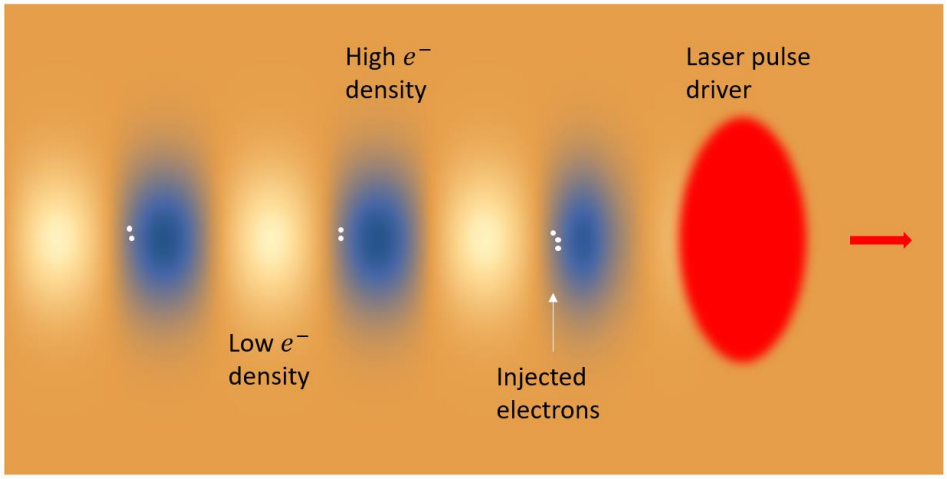

Figure 1.2 Schematic drawing of laser wakefield acceleration

The LWFA field has witnessed numerous milestones in its development, such as the first demonstration of low energy spread beams at ~100 MeV [11–13] and multi-GeV electron acceleration [14]. In 2019, Lawrence Berkeley National Lab demonstrated a record 7.8 GeV electron beam [15], pushing the field one step further toward developing a high energy electron collider [16].

A laser wakefield accelerator reaching multi-GeV energy gain requires high repetition rate guiding of high intensity laser pulses ($I \gtrsim 10^{18} W/cm^2$) over tens of centimeters in low density plasma ($N_e \sim 10^{17} cm^{-3}$). One of the topics of this dissertation is the demonstration of a method to realize such a low density guiding structure for multi-GeV laser wakefield accelerators. Such experiments will eventually take place at petawatt (10^{15} W) laser facilities, such as one of the facilities of the recently formed LaserNetUS infrastructure [17] or at the European ELI (Extreme Light Infrastructure) [18–20].

In another direction for LWFA research, it is of great interest to develop sources of high repetition rate (> 1 kHz) relativistic electron bunches for scientific, medical,

and security imaging applications. To this end, our group at UMd and a French group at Ecole Polytechnique have developed such sources [21–23], with quasi monoenergetic electron bunches up to ~15 MeV generated at 1 kHz with as little as ~2 mJ [24]. Key to the UMd effort in high repetition rate LWFA is the use of near-critical density gas jets. The electron acceleration process in such dense jets produces a remarkably bright, coherent, and broadband optical radiation flash—the detailed study of this flash is another topic of this dissertation.

1.2 Outline

The rest of this chapter provides a short introduction to laser wakefield acceleration (LWFA). Chapter 2 describes experiments on coherent broadband radiation emitted in laser wakefield acceleration in near-critical density gas jets. These are experiments associated with the UMd efforts to develop a high repetition rate, low laser pulse energy LWFA source. The following chapters describe our experiments using low order and high order Bessel beams to generate long, low density plasma waveguides for application to > GeV electron acceleration. Chapter 3 demonstrates high order Bessel beam generation and its optimization. Chapter 4 presents generation of low density plasma waveguides using low and high order Bessel beams. The dissertation concludes with a discussion of prospective research directions.

1.3 Ionization with intense laser pulses

Short pulse laser ionization of atoms or molecules successively moves through three regimes as laser intensity is increased: multi-photon ionization (MPI) [25],

tunneling ionization, and barrier-suppression-ionization [26](see Figure 1.3). The dimensionless Keldysh parameter, $\gamma = \sqrt{E_i/2U_p}$, characterizes the three regimes, where E_i is the ionization energy and $U_p = \frac{e^2E^2}{4m_e\omega^2}$ is the laser ponderomotive energy [27]. In the MPI regime ($\gamma \gg 1$), $n = \lceil E_i/\hbar\omega \rceil$ photons are required to liberate a bound electron to the continuum, where $\hbar\omega$ is the laser photon energy and $\lceil\ \rceil$ is the ceiling function. The ionization rate is $W_n = \sigma_n I_L^n$, where σ_n is the n-photon absorption cross section, and I_L is the laser intensity. In tunneling ionization ($\gamma \sim 1$), the laser electric field adds to the atomic Coulomb field so that a bound electron can tunnel through the resulting humped potential barrier. In barrier-suppression-ionization ($\gamma \ll 1$), the laser electric field strongly dominates the atomic coulomb field, depressing the potential hump below the binding energy. An estimate for the critical intensity for barrier suppression ionization is obtained by $I_{BSI} = \frac{cE_i^2}{128\pi Z^2 e^6}$, where Z is the ionization state of the product ion. For the hydrogen atom, $I_{BSI} \approx 1.4 \times 10^{14} W/cm^2$.

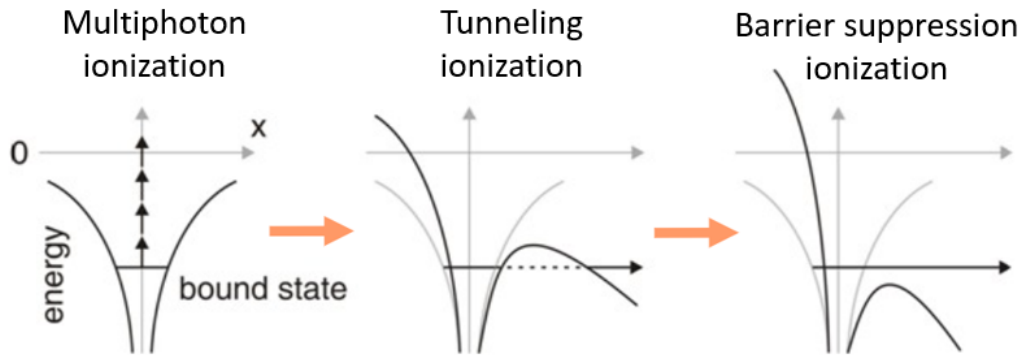

Figure 1.3 Potentials in multiphoton, tunneling and barrier suppression ionization.

1.4 Laser wakefield acceleration (LWFA)

1.4.1 Linear plasma wakefield

In laser plasma accelerators, wakefields are driven by the ponderomotive force. The ponderomotive force $\boldsymbol{F}_p$ is derived by solving the electron momentum equation $\frac{d\boldsymbol{p}}{dt} = -e(\boldsymbol{E} + \frac{\boldsymbol{v}\times\boldsymbol{B}}{c})$ to second order in $|\boldsymbol{a}| = a$, where $\boldsymbol{a} = e\boldsymbol{A}/m_e c^2$ is the normalized vector potential of the laser. In the linear regime ($a \ll 1$), $\frac{d\boldsymbol{\delta p}}{dt} = \boldsymbol{F}_p = -m_e c^2 \nabla(\boldsymbol{a}^2/2)$. In the nonlinear regime, using the normalized momentum $\boldsymbol{u} = \frac{\boldsymbol{p}}{\gamma m_e c}$ (with $\gamma = (1 - u^2/c^2)^{-1/2}$) and normalized scalar potential $\Phi = \frac{e\phi}{m_e c^2}$, we rewrite the momentum equation as [28]

$$\frac{d\boldsymbol{u}}{cdt} = \nabla\Phi + \frac{1}{\mathrm{c}}\frac{\partial \boldsymbol{a}}{\partial t} - \frac{\boldsymbol{u}}{\gamma} \times (\nabla \times \boldsymbol{a}). \tag{1.1}$$

Using the identity $(\boldsymbol{a}\cdot\nabla)\boldsymbol{a} = \frac{1}{2}\nabla\boldsymbol{a}^2 - \boldsymbol{a}\times\nabla\times\boldsymbol{a}$ and defining $\delta\boldsymbol{u} = \boldsymbol{u} - \boldsymbol{a}$, it can be shown [28] that $\frac{\partial \boldsymbol{\delta u}}{c\partial t} = \nabla(\Phi - \gamma)$. Therefore, we recognize the generalized ponderomotive force $\boldsymbol{F}_p = -m_e c^2 \nabla\gamma$.

Assuming $a \ll 1$, the plasma wave driven by the ponderomotive force can be solved using the momentum, continuity, and Poisson equations (assuming a cold fluid),

$$\frac{d\boldsymbol{p}}{dt} = -e(\boldsymbol{E} + \frac{\boldsymbol{v}\times\boldsymbol{B}}{c}), \tag{1.2}$$

$$\frac{\partial n}{\partial t} + \nabla \cdot (n\boldsymbol{v}) = 0, \tag{1.3}$$

$$\nabla^2\phi = 4\pi(n - n_0), \tag{1.4}$$

where n_0 is the unperturbed plasma density

Solving the above three equations to second order in a, the density perturbation and electrostatic potential are [10,29]

$$\left(\frac{\partial^2}{\partial t^2}+\omega_p^2\right)\frac{\delta n}{n_0}=c^2\nabla^2 a^2/2, \tag{1.5}$$

$$\left(\frac{\partial^2}{\partial t^2}+\omega_p^2\right)\phi=\omega_p^2 a^2/2, \tag{1.6}$$

where $\omega_p^2=4\pi N_{e0}e^2/m_e$.

The above equations show driven simple harmonic oscillator behavior. Therefore, the wakefield will be generated most efficiently when the driving laser pulse envelope is of the same order as half the plasma oscillation period. The plasma wakefield travels at the speed of the driving ponderomotive force, which propagates with the laser envelope at the group velocity. Equations (1.5) and (1.6) are solved for the plasma density perturbation and electric field using a Green's function to give

$$\delta n/n_0=(c^2/\omega_p)\int_0^t dt'\,\sin\left[\omega_p(t-t')\right]\nabla^2 a^2(r,t')/2, \tag{1.7}$$

and

$$E/E_0=-c\int_0^t dt'\,\sin\left[\omega_p(t-t')\right]\nabla a^2(r,t')/2. \tag{1.8}$$

Most experiments fall in the nonlinear regime ($a\gtrsim 1$), where analytical expression becomes complicated and computer simulations are needed. With the quasi-static, an analytical expression of a 1D nonlinear wakefield can be found in [30,31]. Wakefields in 3D typically require particle-in-cell (PIC) simulations.

1.4.2 Pulse propagation and self-modulation

In the linear regime, the laser group velocity is derived from the 1D dispersion relation $\omega^2=c^2k^2+\omega_p^2$, yielding the group velocity relativistic factor $\gamma_g=\frac{\omega}{\omega_p}$. However, the group velocity can be affected by 3D effects. For tightly focused laser

pulses, off-axis rays reduce the effective group velocity as well as sample plasma dispersion. Taking this 3D effect into consideration, the group velocity relativistic factor is [32] $\gamma_g \approx \left(\frac{\omega_p^2}{\omega^2} + \frac{2c^2}{\omega^2 r_0^2}\right)^{-1/2}$.

If the laser pulse duration is longer than multiple plasma oscillation periods, the laser pulse can be periodically diffracted and focused by the plasma wakefield it drives. This can lead to breakup of a single long laser pulse into a train of short pulses, with each short pulselet having a width on the order of half a plasma wavelength. Accompanying the formation of the pulse train is a large amplitude plasma wave. This process is called self-modulation [28,33]. A laser wakefield accelerator operating in this regime typically accelerates high charge electron bunches with a broad (exponential-like) energy distribution. The experiment described in chapter 2 fits in this regime.

1.4.3 Electron injection and wave breaking

Electrons must be properly phased in order to be trapped by the plasma wave and accelerated. One source of trapped electrons is the background plasma electrons, where self-injection occurs by wave breaking. This is the injection source for the high density jet experiments described in Chapter 2. An example of another source, not used in this dissertation, is ionization injection [34–36]. In ionization injection, inner shell electrons of high-Z atoms are tunneling ionized near the peak of the laser pulse, at a particular phase inside the wakes and subsequently slip back with respect to the wakes. If the electrons gain enough energy from the longitudinal electric field to catch up with the wakes, then the electrons are trapped and accelerated to higher

energy. As the electrons are born near the peak of the wake potential, the high potential difference between the front and back of the wakes results in lower laser intensity required to trap electrons than self-injection.

For proper phasing, the injected electron velocity must be at least the wakefield phase velocity. For the case of wavebreaking, this occurs when the plasma wakefield amplitude approaches the wave breaking limit $E_{WB} = \sqrt{2(\gamma_p - 1)}E_0$ [37] (1D cold plasma), where $E_0 = mc\omega_p/e$ is the cold nonrelativistic wave breaking field [38] and $\gamma_p = \gamma_g = \omega/\omega_p$ is the relativistic factor for the plasma wave phase velocity. When wave breaking occurs, the electron excursion is of the order of a plasma wavelength and the plasma wave loses coherence.

In higher dimensions, plasma wave fronts are curved due to the finite transverse extent of the driving laser pulses. When the electron excursion amplitude is similar to the radius of curvature of a plasma wavefront, the trajectories of different electrons can cross, and the plasma wave loses coherence. This scenario is called “transverse wave breaking”, and the wave breaking field can be significantly reduced in this scenario [39].

Numerous methods, including ionization injection, have been proposed to control electron injection spatially and temporally with much better precision than wavebreaking. For descriptions of those techniques, we refer readers to [40]

1.4.4 Dephasing and energy scaling

Electrons accelerated by a laser wakefield gain energy until they outrun the laser pulse, posing a fundamental limit to the maximum energy gain. This mechanism is dephasing. Dephasing occurs when high energy electrons move forward in in phase

by $\lambda_p/4$ with respect to the plasma wake, as only 1/4 of the plasma wave is simultaneously accelerating and focusing [41]. The dephasing length is [40]

$$L_d \approx \frac{\lambda_p^3}{2\lambda^2} \times \begin{cases} 1, & a_0^2 \ll 1 \\ \sqrt{\frac{2}{\pi}} \frac{a_0}{n_p}, & a_0^2 \gg 1 \end{cases}, \tag{1.9}$$

where n_p is the number of plasma periods behind the laser pulse. The maximum electron energy picked up in a standard laser wakefield accelerator (pulse length~λ_p), if limited by dephasing alone, is [41]

$$\Delta W_d(MeV) \approx \frac{630 I(W/cm^2)}{N_e(cm^{-3})} \times \begin{cases} 1, & a_0^2 \ll 1 \\ \frac{2}{\pi n_p}, & a_0^2 \gg 1 \end{cases}. \tag{1.10}$$

Therefore, multi-GeV electron acceleration typically requires $N_e \sim 10^{17} cm^{-3}$ with dephasing length of several tens of centimeters.

Chapter 2 Coherent ultra-broadband laser-assisted injection radiation from a laser plasma accelerator

2.1 Introduction

The accelerating structure in a laser wakefield electron accelerator is provided by the relativistic nonlinear plasma wave driven by the ponderomotive force of the laser pulse. The plasma wave, which follows the pulse as a wake, can support axial electric fields >100 GV/m [10,40]. Electrons can be accelerated after self-injection of background plasma electrons or external injection of relativistic electrons into the wake structure. In the self-injection process [42–44], trapping of background electrons in the wake potential can lead to acceleration of high charge bunches from rest to nearly the speed of light over very short distances, generating radiation. At low plasma densities, this radiation has been observed to be weak and incoherent, even with a high-energy laser driver [45]. However, with near-critical plasma densities, using low energy millijoule-scale lasers, our preliminary experiments showed that injection generates an intense *coherent* broadband ($\Delta\lambda/\lambda \sim 1$) flash of radiation [46] owing to acceleration over distances short compared to the radiated wavelength. Flashes occur axially in the plasma at electron injection locations, which closely follow relativistic self-focusing beam collapse and nonlinear plasma wave generation. A flash is estimated to contain up to a few percent of the laser energy, and can overwhelm optical diagnostics such as probe laser beams [46]. In astrophysics, coherent radio wave emission from pulsars is an analogous process, as it may originate from extreme acceleration of dense electron bunches over distances much shorter than the radiated wavelength [47].

In this chapter, we present detailed measurements showing that under our conditions of near critical density plasma the flash is an ultrashort pulse optical radiation source of at most few-cycle duration, whose coherence, pulsewidth, angular distribution, and polarization are consistent with synchrotron radiation emission from *laser-assisted* injection of dense electron bunches into the plasma wave accelerating structure. The emission is remarkably bright for a non-laser source, with a brightness temperature estimated to be ~10^{18} K. At lower laser power, we observe the flash spectrum peaked at harmonics of the plasma frequency (the first measurement of such harmonics), a signature of sequential trapping in successive plasma wave potential buckets. At higher laser power, the flash spectrum is more continuous, characteristic of electron trapping largely in the main bucket following the laser pulse, with the following buckets strongly dissipated by beam loading.

Our analysis of injection flash radiation provides a detailed picture of the dynamics inside the laser plasma accelerator. If one considers "wave-breaking" to imply destruction of plasma wave coherence [48], our results lead us to identify the flash radiation as originating from laser-assisted injection rather than wave-breaking, as the radiation shows a characteristic polarization signature and coherent periodic features necessitating plasma wave survival through the injection process.

2.2 Experimental setup

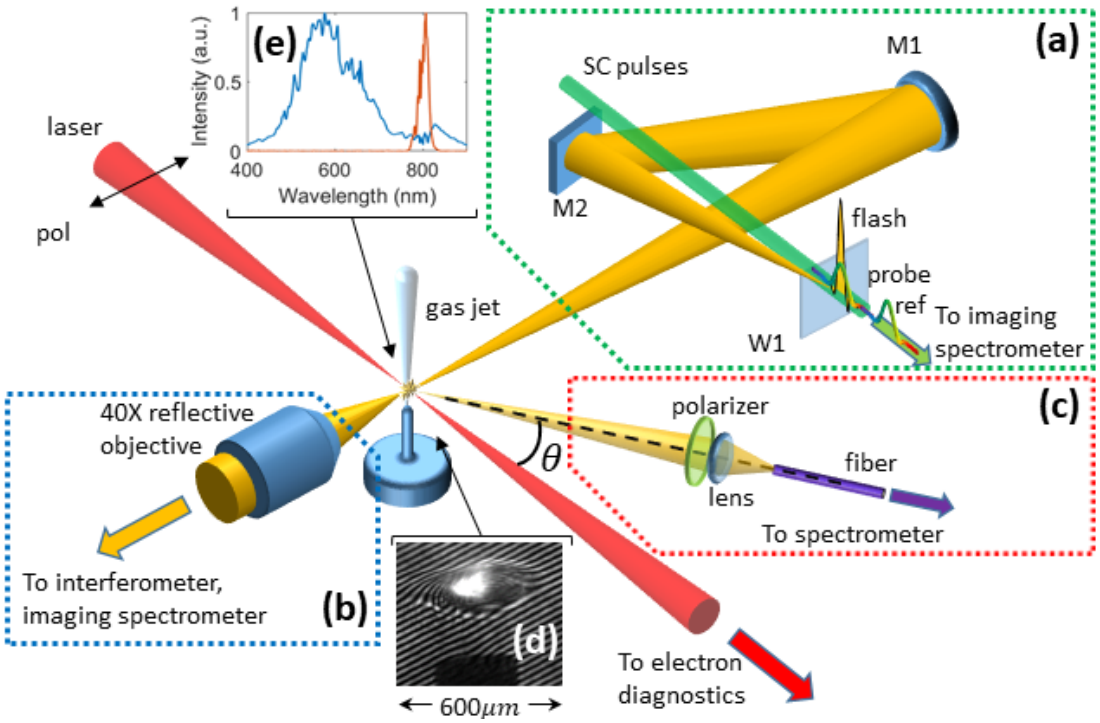

Figure 2.1 Experimental diagram showing laser-gas jet interaction and diagnostics. (a) Setup for single-shot-supercontinuum spectral interferometry (SSSI) for either direct spectral interferometry of the flash (no glass window W1) or for measurement of the flash temporal envelope using flash-induced cross phase modulation in W1. (b) 40× all-reflective objective and imaging spectrometer for high-resolution space-resolved spectra. The objective can be taken out for plasma interferometry and neutral gas density measurement using a folded wave-front interferometer (not shown). (c) Fiber-coupled spectrometer setup for flash angular distribution and polarization measurements. (d) Image of flash superimposed on interferogram of laser-plasma interaction; the flash image is brighter than the interferometer fringes. The rectangular shadow at the bottom of the image is the gas jet orifice. (e) Typical transverse (90°) flash spectrum (blue curve) and laser spectrum (brown curve) for comparison.

The experimental setup is shown in Figure 2.1. Pulses of up to 40 mJ energy from a Ti:Sapphire laser (λ=800nm, 50 fs) are focused into a dense helium or hydrogen gas jet with an *f*/9.5 off-axis parabolic mirror to a full width at half maximum (FWHM) spot size w_{FWHM}=8 μm. In either helium or hydrogen, the plasma peak density is in the range $N_e/N_{cr} \sim 0.1 - 0.3$ with a density profile width d_{FWHM}~$300\mu m$. The neutral gas and plasma density profiles were measured using a λ=400 nm, 70 fs probe

pulse (derived from the main pulse) directed transversely through the jet to a folded wavefront interferometer (not shown in the figure, but in the direction indicated in Figure 2.1(b)). As the flash is produced by electron injection into relativistic plasma waves, it is always associated with the generation of forward directed relativistic electron beams. For all experiments at a given laser energy and plasma profile, flash emission was measured under conditions of maximum charge for accelerated beam energy > 125 keV, as measured by integrating the electron beam images on a LANEX scintillating screen shielded by a 100μm thick Al foil [46].

High-resolution spatio-spectral images of the flash were taken transversely using a 40× all-reflective objective and imaging spectrometer (Figure 2.1(b)), while angle and polarization resolved flash spectra were recorded by fiber-coupled spectrometers (Figure 2.1(c)). A typical image of the bright flash, collected along with an interferogram of the laser interaction with helium plasma, is shown in Figure 2.1(d). The image and interferogram are collected by the interferometer optics (not shown) in the direction shown in Figure 2.1(b). A single-shot flash spectrum collected in the same direction is shown in Figure 2.1(e), with the pump laser spectrum overlaid for reference. The flash spectrum, centered at approximately $\lambda \sim 550$nm, has an extremely wide bandwidth, $\Delta\lambda/\lambda > 0.5$. The modulations in the flash spectrum are not noise—their physical significance will be discussed in the following sections.

The flash spatio-temporal evolution was measured using single shot supercontinuum spectral interferometry (SSSI), a technique developed by our group [49,50]. The single shot capability of SSSI is essential, as the flash can vary from shot-to-shot even with nominally similar laser and gas jet parameters. We use

SSSI in two ways. In method (1), radiation from a single flash (yellow beam in Figure 2.1(a)) is collected at *f*/3 with 3× magnification by silver mirror M1, 0.2 *m* from the source, and directly interfered with a single well-characterized supercontinuum (SC) probe pulse at the imaging spectrometer in Figure 2.1(a), with 1D space resolution 5 μm along the direction of the slit, oriented perpendicular to the laser propagation direction. In the case of multiple, spatially distributed flashes in a single shot, this resolution is sufficient to image a single flash when it appears in the field of view. The SC pulse is generated by filamentation of a small portion of the laser pulse in a 2-atm xenon cell. This measurement enables determination of the flash spectral coherence and extraction of its spectral phase. In method (2), we use a pair of SC pulses—a reference pulse and a probe pulse-- to measure the ultrashort transient Kerr effect induced by the flash in a 200 μm-thick BK7 glass window W1. Here, a single SC pulse is first generated by filamentation in the Xe cell, followed by a Michelson interferometer to generate the pair, and then followed by dispersing prisms that chirp the pulses to ~1 ps. The reference and probe pulses spatially overfill the flash image in the glass, with the reference pulse preceding the flash, and the probe temporally overlapped with it. Fourier analysis of the reference-probe interferogram at the spectrometer focal plane yields the 1D space-resolved transient Kerr phase shift in the glass, which is proportional to the flash spatiotemporal intensity profile $I_{flash}(x,t)$, where *x* is along a 1D slice in the plasma perpendicular to the laser propagation direction.

2.3 Coherent radiation and pulse length measurement

The spectral phase of the supercontinuum is measured by modulations in the probe pulse spectrum due to flash induced cross phase modulation as a function of delay between flash and probe [50] as shown in Figure 2.2. Using a 4th order polynomial fit, we extract the spectral phase to be $\phi(\omega) = \sum_{n=0}^{4} \beta_n (\omega - \omega_0)^n$, where $\beta_2 = 1570 \pm 52\ fs^2, \beta_3 = 222 \pm 51 fs^3, \beta_4 = -3 \pm 70\ fs^4, \omega_0 = 3.6\ PHz$.

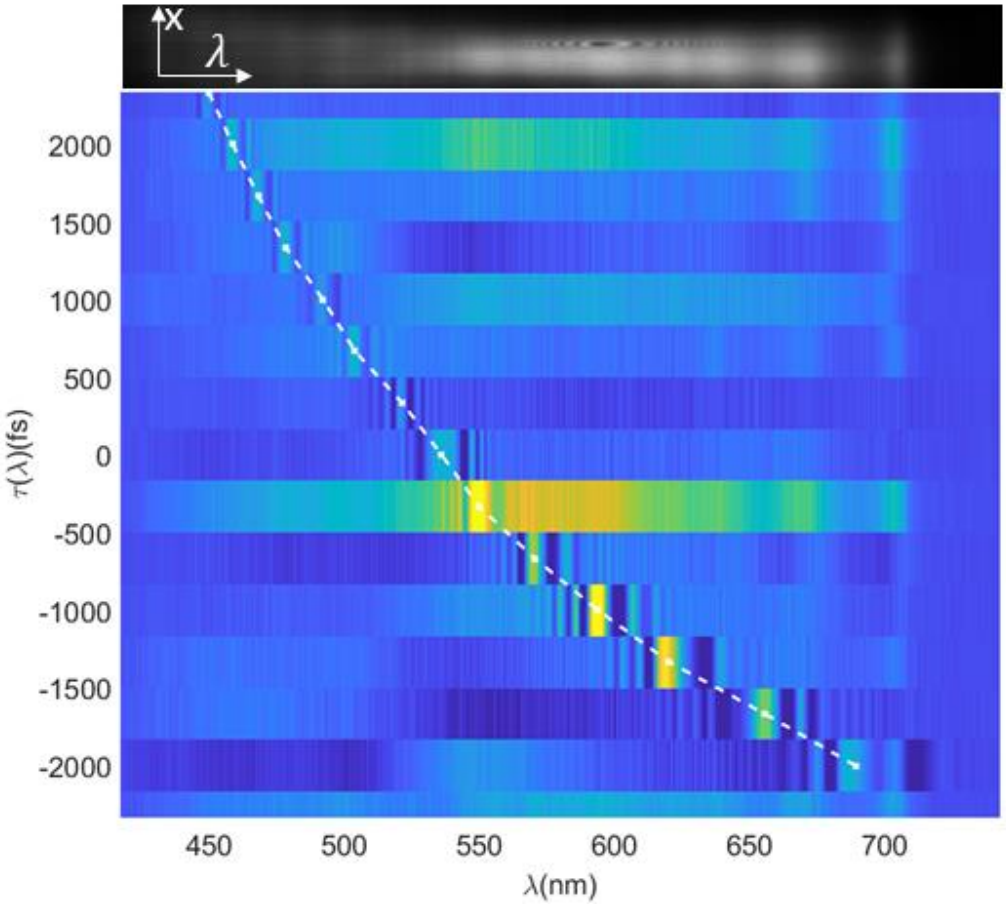

Figure 2.2 Determination of SC spectral phase. Top: Sample SC spectrogram showing modulation due to cross phase modulation. Bottom: Group delay τ(λ) vs λ using a 25-spectrogram average at each delay.

The spectral coherence of the flash is demonstrated in Figure 2.3, which shows a broadband spatio-spectral interferogram (Figure 2.3(a)) and corresponding lineout

(Figure 2.3(b)) from spectral domain interference between the flash and a SC probe pulse using method (1) described above. The high contrast fringes (visibility~0.62 near ~650 nm) in the λ=425-710 nm overlap region of the SC and flash spectra demonstrate spectral coherence of the flash. The curvature of the fringes arises from interference between the planar wavefronts of the SC probe and the spherical wave fronts from the point-like flash emission imaged at the source. In Figure 2.3(a), the fringe period is largest near λ~535nm, which is where, in this case, the flash temporally overlaps the chirped probe pulse and then deceases at longer and shorter wavelengths. Knowledge of the spectral phase of the SC probe allows extraction of the spectral phases of single flashes, which are flat to within the uncertainty of the probe spectral phase [51].

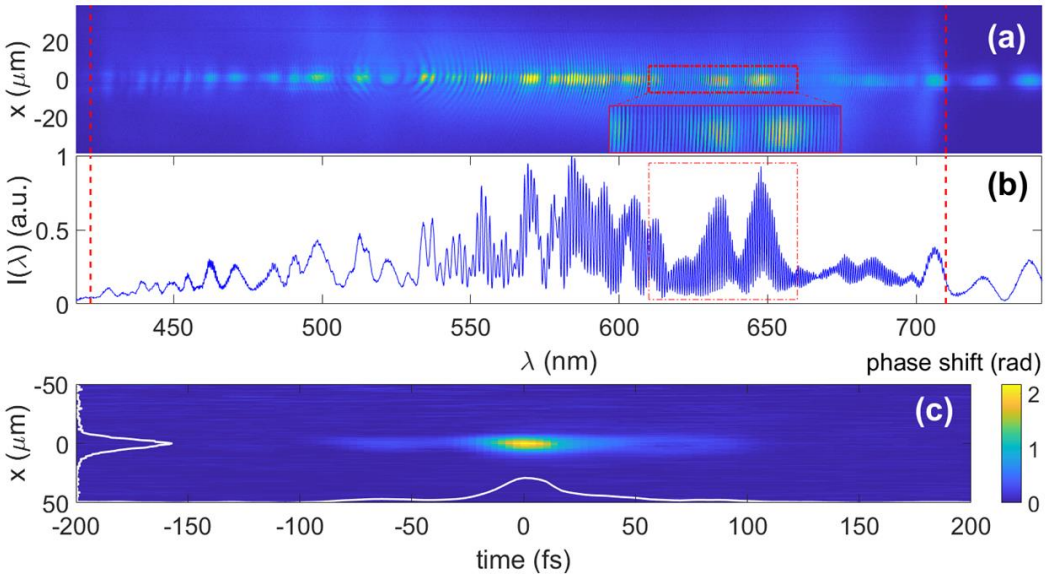

Figure 2.3 (a) Spectral interferogram of flash and supercontinuum (SC) probe pulse. Curved fringes result from interference between the point-source-like flash and the planar phase fronts of the SC probe. The center of fringe curvature at λ~535nm is where the flash temporally overlaps the chirped probe pulse. The larger red outlined box is an expanded section of the spectrum to show the actual aliasing-free fringe spacing. (b) Lineout of (a) at z=0 μm. The vertical red dashed lines indicate the extent of the SC spectrum and the interference fringes, and the box corresponds to the

smaller rectangle in (a). (c) SSSI reconstruction of the flash spatio-temporal profile. Space and time lineouts along z=0 and t=0 are shown as white curves. The spatial and temporal FWHM are ~9 μm and ~30 fs, both limited by space and time and resolution (see text). Laser energy 30 mJ, helium plasma density $N_e/N_{cr} = 0.26$.

Higher-resolution flash spectra, 1D space-resolved with a resolution of ~2 μm, were imaged with a 40× reflective microscope objective to the entrance slit of another imaging spectrometer (Figure 2.1(b)). This setup avoids chromatic aberration of the broadband flash images. Lower resolution polarization- and angle-resolved flash spectra were collected by fiber-coupled spectrometers [51] in the range λ= 0.2 -2.5 μm (Figure 2.1(c)).

The flash spatio-spectral complexity is analyzed using high-resolution images taken with the reflective microscope and imaging spectrometer setup of Figure 2.1(b), with results shown in Figure 2.4 for the laser vacuum focus position at the centre of the jet. Here, the imaging spectrometer has its slit aligned along the laser propagation direction (shown by white arrow in Figure 2.4(a)) and records the evolution of the radiation spectrum along z. The pump laser energy was varied 20 - 40 mJ for peak plasma density $N_e/N_{cr} = 0.08$ or 0.16 $(1.3 \text{ or } 2.7 \times 10^{20}\text{cm}^{-3})$. For our conditions, flashes are mostly emitted at two axial (z) locations and spectra appear either with clearly separated peaks or with more continuous features, with the latter appearing with increasing laser energy or plasma density. At lower laser energy and density (Figure 2.4(a), 20 mJ, $N_e/N_{cr} = 0.08$) the spectrum at z~ 60μm consists of discrete peaks with equal spacing close to the plasma frequency, $\Delta\omega \sim \omega_p$=0.61 PHz at density $N_e = 1.3\times10^{20} cm^{-3}$, and from their frequency ratio of 4:5:6 they are identified as the 4th, 5th and 6th harmonic of ω_p. This is the first observation of optical

electromagnetic radiation at harmonics of the plasma frequency. Another flash occurs ~20 μm downstream in the propagation direction, where the wavelength spacing of the peaks decreases slightly and they shift to higher wavelength, consistent with locally lower plasma frequency along the density downramp. At higher density (Figure 2.4(b)), the peaks are less distinct and more closely spaced, with the first flash slightly earlier in *z* and a second flash occurring ~40 μm downstream of the first.

The spectral interferograms and flash spectral phase are used to determine the time dependence of single flashes. Figures 2.4(a′) and 2.4(b′) show the square magnitude of the Fourier transforms of Figure 2.4(a) and 2.4(b) (using the extracted approximately flat spectral phase from the SSSI measurement), yielding the time dependence of the radiation intensity for the *z* position strips indicated by the black and red line segments on the left of the plots. It is seen for all cases that the flash is a sharp emission burst of duration < 5 fs followed by decaying modulations at the local plasma period $\tau_p = 2\pi/\omega_p$. At higher laser energies (panels (c′)-(f′)), the temporal modulations following the initial burst become less distinct, with more rapid decay. Also at higher energy, the spatial location of the first flash moves upstream, consistent with the earlier onset of relativistic self-focusing beam collapse. As the measured flash spectrum is limited at the high and low frequency ends by coherence and plasma absorption (see later), the initial flash burst is likely significantly shorter than 5 fs.

Among electromagnetic radiation sources from a LWFA, injection flash radiation is the only temporally coherent source measured thus far originating from the plasma accelerating structure. Another temporally coherent source is transition radiation from

accelerated electron bunches exiting the plasma-vacuum boundary [52], while betatron radiation is spatially but not temporally coherent [53]. The observation of coherent emission *at* the harmonics of the plasma frequency is distinct from Raman scattering of the pump laser pulse [40,54], where spectral features would be shifted from the pump frequency by integer multiples of ω_p. The physical interpretation of flash radiation at harmonics of the plasma frequency is straightforward: as the nonlinearly steepening plasma wave propagates forward at the laser group velocity, it traps and accelerates background electrons. For the case of lower laser energy and density, the plasma wake potential is still sufficiently weak to allow some of these electrons to slip back and be trapped by later successive plasma wave buckets, separated in time by τ_p. As the plasma wake propagates past a fixed spatial location viewed transversely by the imaging spectrometer, the repeated trapping and acceleration of background electrons at intervals of τ_p gives rise to the modulated spectrum. For the larger amplitude plasma waves driven at higher laser intensity and higher density, strong trapping of background electrons occurs in the bucket closest to the laser pulse, and beam loading decreases the amplitude of successive buckets and their associated trapping.

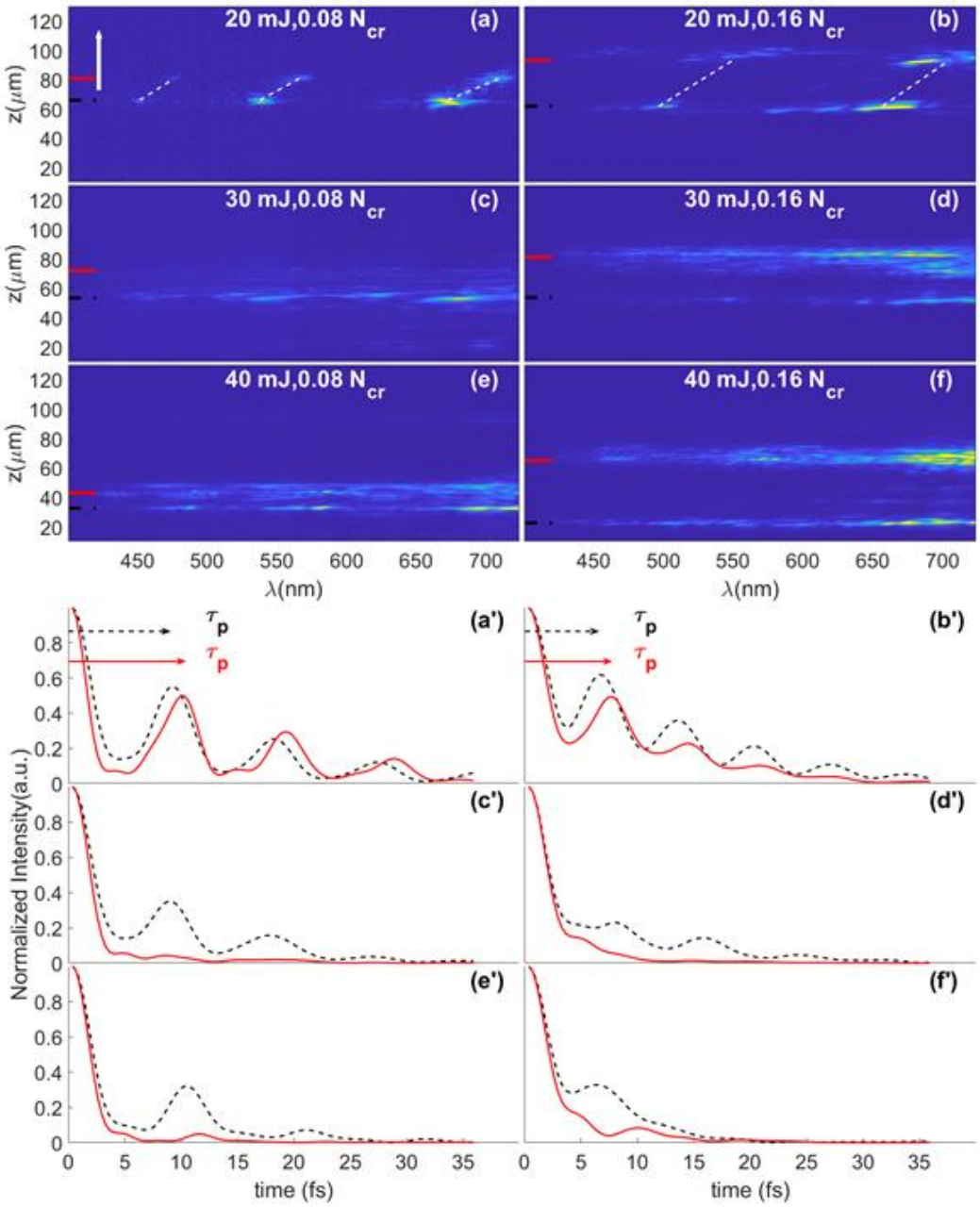

Figure 2.4 (a)-(f): Space-resolved flash spectra for laser energies 20, 30, 40 mJ and peak densities $N_e/N_{cr} = 0.08$ and 0.16 . The laser propagates in the direction of the white arrow in (a). (a′)-(f′): Square of the frequency-to-time Fourier transforms of the (a)-(f) spectra at fixed z positions indicated by the black (dashed) and red (solid) line segments (20 rows of CCD camera pixels), which correspond to the black (dashed) and red (solid) curves. The oscillations are spaced by the local plasma period τ_p. The white dashed lines in (a) and (b) show the density downramp dependence of the harmonics of plasma frequency ω_p(from left to right): (a) 6th, 5th, 4th, and (b) 4th, 3rd.

We can estimate the number of injected electron buckets by the width of the harmonics peaks. The total electric field radiated by a sequence of N identical flashes separated by $\tau = 2\pi/\omega_p$ is expressed as $E_{tot}(t) = \sum_{n=1}^{N} E(t - n\tau)e^{-i\omega_0(t-n\tau)}$, where E(t) is the field envelope for a single flash, and ω_0 is a flash central frequency. Its spectrum, $\left|\widetilde{\boldsymbol{E}}_{tot}(\omega)\right|^2 = \left|\widetilde{\boldsymbol{E}}(\omega - \omega_0)\right|^2 \frac{\sin^2(\omega N\tau/2)}{\sin^2(\omega\tau/2)}$, has peaks at the harmonics of the plasma frequency, agreeing with the experimental spectrum of Figure 2.4(a), and peak width (FWHM) is $\Delta\omega \sim \omega_p/N$. From the width of the spectral peaks in Figure 2.4(a), one can estimate that a train of ~9 buckets contributes to the emission, which at this plasma density is >90 fs, extending well behind the 40fs laser pulse.

We also measured the temporal envelope of single flashes using SSSI, described above as method (2) and depicted in Figure 2.1(a). The overall temporal resolution of this measurement is limited by the SC bandwidth and spherical aberration of the collection optics to $\Delta t_{min} \sim 20$ fs [51]. The spatio-temporal trace in Figure 2.3(c) shows a flash emission $\tau_{FWHM} \sim$ 30fs, with a long tail extending beyond ~50fs. To within the temporal resolution, this is consistent with the curves shown in Figure 2.4(a′)-(f′), where the emission consists of multiple ~5 fs peaks, with fewer peaks and faster decay at higher laser energy. From Figure 2.4(a) and (b), the flash extent along the propagation direction indicated by the arrow is $d_{flash} \sim$2.5 μm, near the imaging resolution limit, which suggests the acceleration radiation timescale is, at most, $\tau_{accel} < d_{flash}/c \sim 10\ fs$. It is remarkable that a demagnified image in the glass of only a small portion of this coherent source emission generates a nonlinear phase shift of ~2 radians (Figure 2.3(c))—equivalent to flash intensity at the image plane of

2×10^{12} W/cm^2 . Using this result and the measured flash angular distribution (see below), we estimate the flash energy as ~0.4 mJ with a 4π average peak brightness of ~250 J cm^{-2}sr^{-1}, conservatively assuming a resolution-limited 2μm source radius (see later discussion for Figure 2.5(c)). Assuming a smaller source size from the simulation (see Sec. III) of 150nm×300nm and a ~5 fs emission burst as seen in Figure 2.4 at higher density, gives an intensity brightness of ~3×10^{18} W cm^{-2}sr^{-1}. For the flash bandwidth measured, this corresponds to a brightness temperature of T_b~ 10^{18} K. As comparisons, the brightness temperature of the sun is <10^4 K and is in the range 10^{25}-10^{31} K for pulsars [47].

In our experiment, the temporal resolution of SSSI in method (2) mainly depends on aberrations in the collection optics and on the intrinsic resolution of SSSI [50]. For simplicity, we only estimate the effect of spherical aberration of the concave silver mirror. According to Eq. (15) of [55], the total delay caused by spherical aberration of the concave mirror can be estimated as $\tau_{SA} \approx \frac{1.5Ar^4}{\omega_0}$, where A is a dimensionless number characterizing the 3rd order spherical aberration and r is normalized to the maximum aperture radius. For a concave mirror, it can be shown that $A = -\frac{k_0 a^4}{4R^3}$ [56] where k_0 is the center wave number, a the maximum aperture radius and R the radius of curvature of the concave mirror. In our case, for λ_0~$600\ nm$, A ~ 24 (where A is calculated assuming focusing of a collimated beam). This gives $\tau_{SA} = 11.4\ fs$ as an estimate for spherical aberration stretching by the concave mirror.

The limited spectral resolution of the imaging spectrometer in Figure 2.1(a) limits our temporal resolution according to $\tau_w \geq 4\pi|\beta_2\tau_r^{-1}|$, where τ_r is the maximum available temporal separation between the probe and reference pulse, $\beta_2 = \frac{\partial^2\phi(\omega)}{\partial\omega^2}$ the first order chirp of the reference pulse [50]. In our experiment, $\tau_r \approx 1\ ps, \beta_2 \approx 1570\ fs^2$, giving $\tau_w \approx 19.7\ fs$. An estimate of the overall temporal resolution is then $\tau_{res} \approx \sqrt{(\tau_{SA}^2 + \tau_w^2)}$ ≈23 fs.

2.4 Polarization and angular distribution

The angular distribution and polarization of the flash spectrum is shown in Figure 2.5 for incident laser energy 40 mJ and a hydrogen gas jet with peak plasma density N_e/N_{cr}~0.1. The setup is shown in Figure 2.1(c). The spectrum is collected by fiber-coupled broadband visible and IR spectrometers covering a combined range 200–2500 nm [51]. The optical fiber is mounted to a rotating arm which scans in azimuthal angle θ=30–150° with respect to the pump propagation direction, with the flash radiation passing through a broadband polarizer before entering the fiber. The collection acceptance solid angle is $\Delta\Omega = 1.8 \times 10^{-3}$ sr, set by the fiber collimator aperture, giving an angular resolution of $\delta\theta \sim \sqrt{\Delta\Omega} \sim 2.5^\circ$. This measurement has no spatial resolution at the flash source; multiple flash locations contribute to the collected spectra. The flash polarization is sampled over ϕ = 0–90°, where ϕ = 0° refers to P-polarization (in the plane of the pump pulse direction, the fiber arm, and the pump polarization), and ϕ=90° describes S-polarization perpendicular to that plane. Only P-polarization (∥) and S-polarization (⊥) results are shown here, with full polarization scans shown in [51]. The fiber collection efficiency was normalized over

the full angular scan range by the isotropic and unpolarized 3*d*-2*p* hydrogen recombination emission at λ=656 nm [57]. As the transmission cone angle of the laser and laser-induced SC at the jet exit is approximately $\Delta\theta_{laser} < 10\,°$, there was no laser contribution to the flash radiation collected at θ=30°, the smallest forward angle sampled.

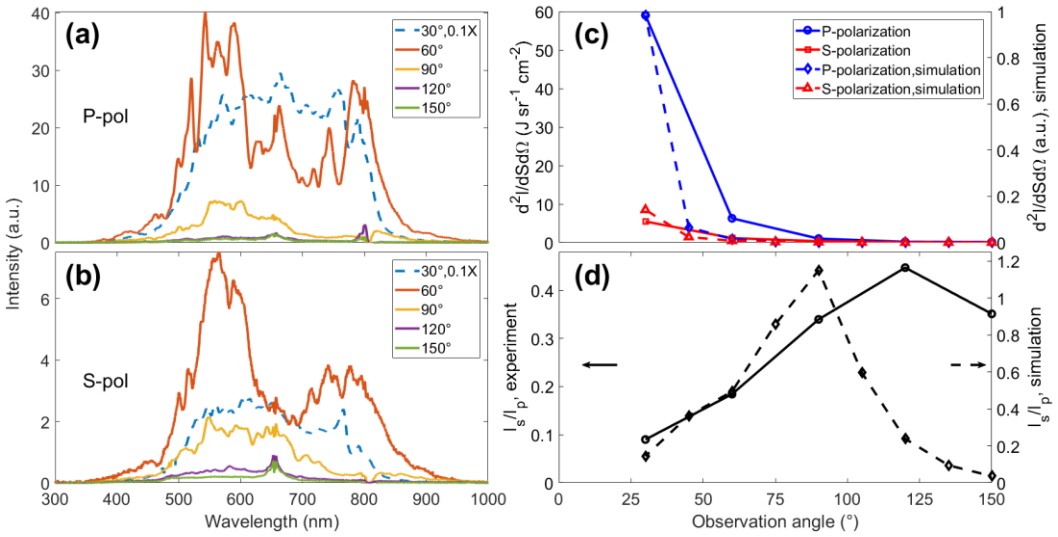

Figure 2.5 (a) (b) Spectrally resolved angular distribution of P- and S-polarized radiation. The angle in the legend is θ in Figure 2.1(c). The spectra at 30° are shown in dashed lines and the spectra of 60° to 150 ° are shown in solid lines from top to bottom in both figures. (c) Flash brightness integrated over λ=380–1000 nm for S- and P-polarization as a function of observation angle. Solid curves: experiment; dashed curves: simulation. The simulation curves are normalized to the experimental P-polarization brightness at θ=30°. (d) Ratio of S- to P-polarized radiation vs. angle θ. Solid curve: experiment; dashed curve: simulation.

Examining Figure 2.5(a)-(c), it is seen that for both P- and S- polarization, the flash angular distribution peaks in the forward direction and decays rapidly with increasing azimuthal angle. Under all conditions, little to no radiation is collected at $\lambda \lesssim 350\ nm$ or $\lambda \gtrsim 950\ nm$. In the forward direction, the collected radiation is dominantly P-polarized. The spectrally integrated brightness $(d^2I/dSd\Omega)_{\perp\parallel}$ of S- and P-polarized emission is plotted vs. angle in Figure 2.5(c). The vertical scale is based

on the collection solid angle and absolute energy calibration of the spectrometer [51], and a conservative estimate of the source area *dS* uses the resolution-limited half-width-at-half maximum of ~2 μm from the spatio-spectral image of single flashes in Figure 2.4(b). The scale is consistent with the estimate based on the nonlinear phase shift induced by the flash in glass (Figure 2.3(c)). As the angle increases away from forward, there is an increasing S- polarization component, as shown in Figure 2.5(d), which plots $I_s/I_p = (d^2I/dSd\Omega)_\perp[(d^2I/dSd\Omega)_\parallel]^{-1}$.

As a check on the polarization sensitivity of the flash emission, we inserted either a λ/2 plate or a λ/4 plate before the off-axis parabolic mirror to rotate the linear polarization or to produce circular polarization. Figure 2.6 shows the ratio I_s/I_p measured at θ=90° for S- , P-, and circularly polarized pump-driven flash radiation. Here, in a more qualitative measurement, the relative flash energy was obtained from integrating its image on a CCD camera (see Figure 2.1(d)), which imposes its spectral response, cutting off below ~400 nm and above ~900 nm. In each case, the flash spectrum has little direct contribution from the laser, as seen in Figure 2.5. For the S-polarization case, it is possible that side Thomson scattering at θ=90°of laser-generated supercontinuum is contributing to$(I_s/I_p)_{S\,pump} > 1/(I_s/I_p)_{P\,pump}$. The fact that $(I_s/I_p)_{circ\,pump} \lesssim (I_s/I_p)_{S\,pump}$ shows the weak contribution to the flash polarization by orthogonally polarized laser field components.

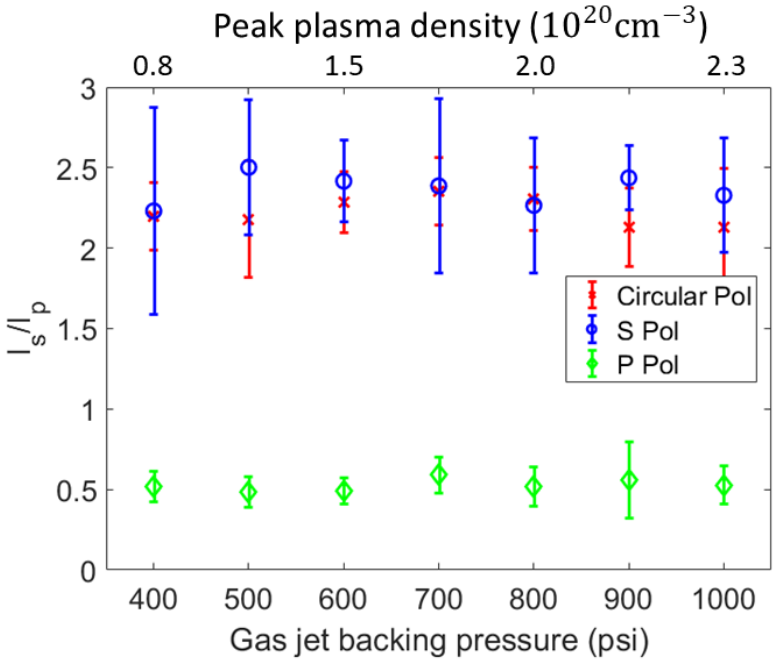

Figure 2.6 Ratio of S-polarized flash emission to P-polarized emission I_s/I_p as observed at θ=90° for P-polarized, S-polarized, and circularly polarized pump laser. Relative flash energy obtained by integrating CCD camera image of flash. For pump energy 30 mJ, plasma FWHM 450μm, H_2 gas jet. Gas jet backing pressure and corresponding peak plasma density is shown on the horizontal axis.

2.5 Flash simulations and discussion

The flash spectrum, angular distribution and polarization are characteristic of synchrotron emission from laser-assisted injection of electrons into the wakefield from off-axis locations on the curved plasma wave crest. The physical picture for this emission scenario is provided by 3D particle-in-cell (PIC) simulations using the code TurboWAVE [58]. The number of grid points is $512 \times 512 \times 768$ and the grid size is $\Delta x = \Delta y = 64.5\ nm, \Delta z = 32.3\ nm$. The time step size is $\Delta t = 0.086\ fs$ to follow the Courant condition. For each grid cell there are 8 particles. The laser is linearly polarized in the *y* direction and propagates in +*z* direction. The laser pulse has a peak normalized vector potential $a_0 = 1$ at the vacuum focus, pulse width $\tau_{FWHM} =$

13.4 fs and focal spot size $w_{FWHM} = 3.1\ \mu m$. The plasma profile contains a plateau of 13 μm with $N_e/N_{cr} = 0.15$ and 14 μm linear ramps on both sides.

The parameters were chosen to save computation time while allowing for multiple pulse lengths (here ~7) to fit inside the jet and for a pulse envelope longer than one plasma period (here ~2). In these respects, the laser-induced plasma wave buckets are similar to the first few following a longer pulse. Figure 2.7 shows simulation results for a laser pulse linearly polarized along *y* with normalized vector potential $a_0 = 1$, pulse width $\tau_{FWHM} = 13.4$ fs and focal spot size $x_{FWHM} = 3.1\mu m$.

To examine the flash radiation field B_z just before and after electron injection is plotted in Figure 2.7(a). Before injection (inset panel), the near-planar phase fronts correspond to the relativistically self-focused laser pulse, whereas after injection there appears a short burst of radiation with spherical phase fronts. The radiation spectrum, shown in Figure 2.7(d), is obtained by Fourier transforming, in the *x* direction, the red-boxed region of Figure 2.7(a). The central wavelength of ~500 nm is in qualitative agreement with the experiment. The trajectory of a trapped electron contributing to this radiation burst is shown in Figure 2.7(b). An expanded view in the inset shows the initial relativistic figure eight-like motion (labeled as 1) of an off-axis plasma background electron in the plane of polarization of the laser field. The electron is first pushed to the left (2) by the E_z component of the self-focused laser field and then is abruptly injected from the electron crest by the E_y component (3) and trapped by the deep potential well that just precedes the crest. The trapped electron is then swept into the on-axis accelerated bunch (4). A movie tracking the electron injection is shown in [51].

The simulation reveals that off-axis injection by the laser is the dominant mechanism: For total electron displacement $\delta s(t) \approx \delta s_p + \delta s_{las}$, where δs_p is the oscillation of a background electron in the plasma wave and δs_{las} is the laser-induced excursion, the latter is sufficient to preferentially kick electrons from the crest, via polarization plane trajectories, into the accelerating potential well of the plasma wave. This is shown in Figure 2.7(c), which plots the normalized electron velocity components $\beta_{x,y,z}$, confirming that the dominant acceleration is in the laser polarization plane (*yz*) and that the injection is laser-assisted. The strongly forward-curved plasma wave fronts [39] make this injection mechanism 3D in nature, with a less stringent dependence on electron velocity than in 1D. In 1D, there would be no laser assist and injected electrons would need to match the plasma wave's phase velocity, inducing wave breaking. By contrast, laser-assisted injection preserves the plasma wave coherence, enabling multiple successive injections as seen in the modulated spectra of Figure 2.4.

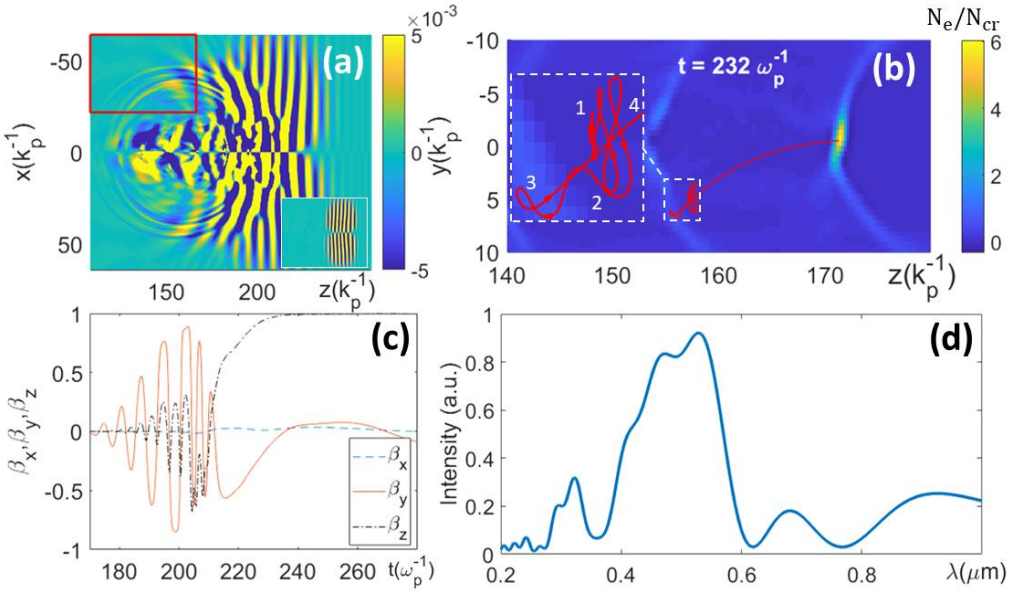

Figure 2.7 Results from 3D particle-in-cell simulation. The laser pulse propagates from left to right. (a) B_z before (inset) and after (main panel) electron injection. The red box encloses a portion of the spherical wave radiated by the injected electron bunch. (b) Lab frame trajectory of electron trapped and accelerated by plasma wave bucket. Orbit phases (1) – (4) are described in the text. Forward curved light blue features are electron crests of the relativistic plasma wave. (c) Normalized velocity components of the electron tracked in panel (b), showing laser-assisted injection. (d) Square of Fourier transform (in *x*-direction) of spherical wave radiation in red box of (a).

To examine which electrons are trapped by the first plasma wave bucket after the laser pulse, we track the trajectories of ~2×10^4 injected electrons with $\gamma - 1 > 0.001$ in a 3D rectangular volume enclosing the accelerated electron bunch as shown in Figure 2.8(a)(b), where the colormap scale is for N_e/N_{cr}. Figure 2.8(c) shows a snapshot of the tracked and injected particles in the beginning of injection, where each dot represents a particle. The injected particles originate mainly from trajectories in the region of the *yz* plane whereas trajectories in the region of the *xz* plane yield many fewer trapped electrons, a fraction $\lesssim 0.1$. The rotational symmetry is broken by the laser polarization. As discussed before, laser-driven excursions preferentially kick electrons from the plasma wave crest into the accelerating potential well of the plasma wave via polarization-plane (*yz* plane) trajectories. Electrons with laser-driven trajectories in the *yz* plane will become preferentially trapped, whereas electrons do not have such laser-assisted trajectories in the *xz* plane; electrons with *xz* trajectories from the plasma oscillation alone will remain untrapped. Thus, Figure 2.8(c) shows a higher density of tracked particles clustered near the *yz* plane, with many fewer near the *xz* plane.

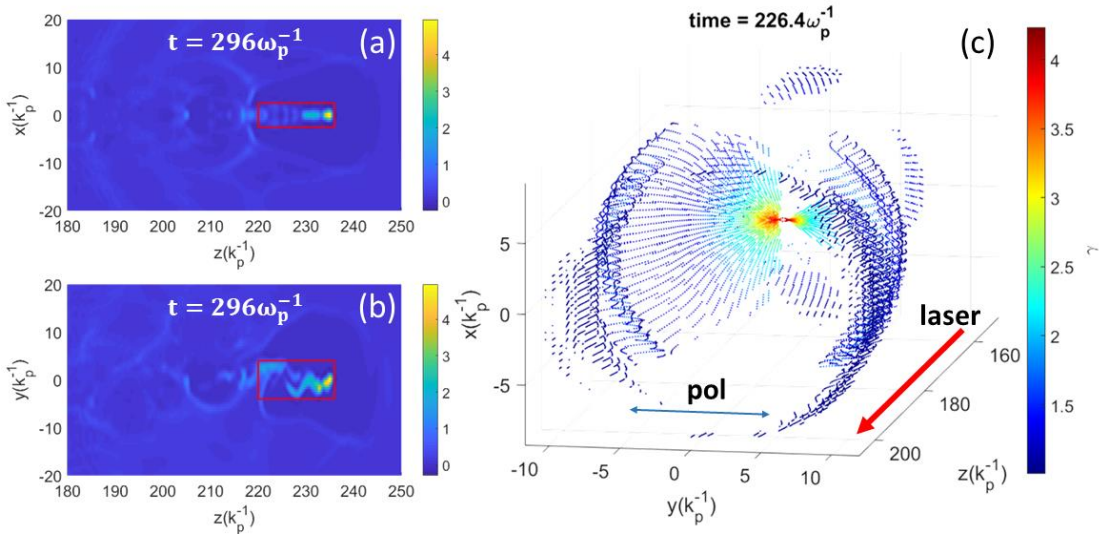

Figure 2.8 (a)(b) Tracked electrons distributions in *xz* and *yz* planes. The red box represents the rectangular volume for selection of electrons with γ>1. The colormap shows N_e/N_{cr}. (c) 3D spatial distribution of tracked particles in an earlier frame. Each dot represents a tracked particle. The colormap is in electron energy normalized to $m_e c^2$. In all plots, $k_p^{-1} \approx 129$ nm.

The angular distribution, polarization, and frequency dependence of the flash are simulated by calculating the total field radiated from the trajectories of the same $\sim 2 \times 10^4$ electrons described above. The polarization-, angle- , and frequency-dependent energy distribution of the injection radiation is [59]

$$\left(\frac{d^2I}{d\omega d\Omega}\right)_{\perp,\parallel} = \frac{e^2}{4\pi^2 c}\left|\hat{\boldsymbol{\varepsilon}}^*_{\perp,\parallel} \cdot \int_{-\infty}^{\infty} dt \sum_j \frac{\hat{\mathbf{n}}\times[(\hat{\mathbf{n}}-\boldsymbol{\beta}_j)\times\dot{\boldsymbol{\beta}}_j]}{(1-\boldsymbol{\beta}_j\cdot\hat{\mathbf{n}})^2} e^{i\omega\left(t-\frac{\hat{\mathbf{n}}\cdot\mathbf{r}_j(t)}{c}\right)}\right|^2, \qquad (2.1)$$

where $\hat{\mathbf{n}}$ is a unit vector pointing from the source to the observation point, $\hat{\boldsymbol{\varepsilon}}_{\perp,\parallel,}$ is the unit vector for S- and P-polarization, and $\boldsymbol{r}_j, \boldsymbol{\beta}_j$ and $\dot{\boldsymbol{\beta}}_j$ are the position, normalized velocity, and acceleration of electron j, and where the sum is over the 2×10^4 electrons. The simulation results explain the measured flash angular distribution and polarization dependence, as well as the coherence. The spectrally integrated source brightness $(d^2I/dSd\Omega)_{\perp,\parallel}$ of S- and P- polarized radiation is plotted in arbitrary

units as a function of θ in Figure 2.5(c) and agrees with the measurements: As the off-axis electron injection to relativistic velocities is dominantly forward directed, the radiation associated with this acceleration will also be forward-directed, accounting for the forward-peaked angular distributions. The dominance of P-polarization of the flash is a direct signature of the laser-polarization-plane orbits favored by laser-assisted injection. By contrast, for the case of wave-breaking-dominated injection, there would be no preferred flash polarization as there would be no preferred electron trajectories.

The observation angle-dependent flash spectrum is also computed using (2.1) and is shown in Figure 2.9. The squared magnitude of its Fourier transform in Figure 2.9(b′) shows a sharp initial burst followed by pulse train structure with approximate ~τ_p spacing, in qualitative agreement with Figure 2.4(a) and (b), τ_p being the plasma period. It is seen that emission harmonics at the local plasma frequency are evident for transverse observation angle (Figure 2.9(b)) but less clear for forward or backward angles (Figure 2.9(a) and (c)). This is consistent with our transverse observation (Figure 2.5) of a source modulated at τ_p at a fixed spatial location. Observation at non-transverse angles is susceptible to either or both of inter-flash (in the case of several flash spatial locations), intra-flash spectral interference or plasma density variation. As the spectra is not spatially resolving, the slower and faster spectral modulations in Figure 2.9(a) and (c) respectively can be explained by interference between multiple flash locations depending on the observation angle.

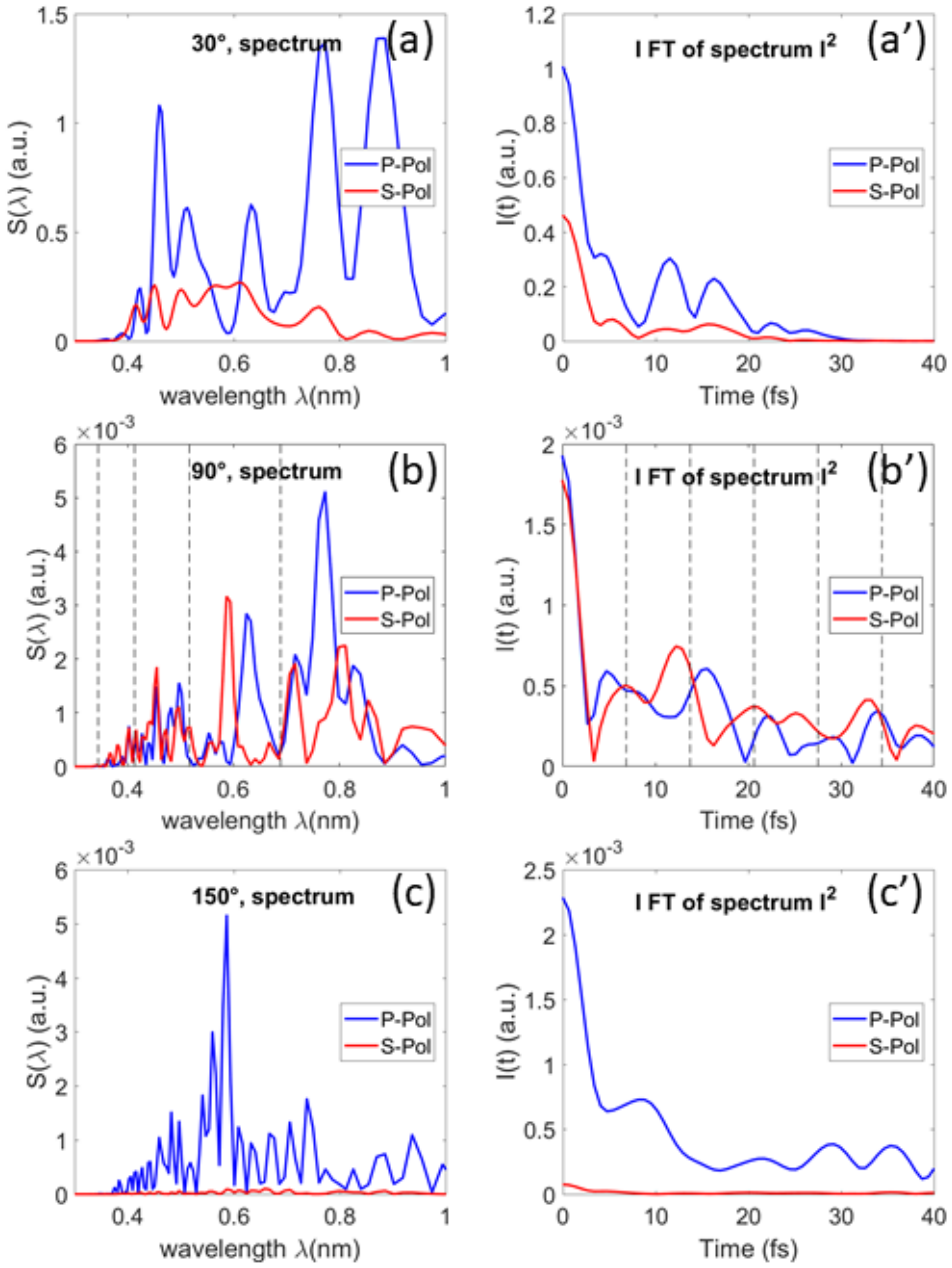

Figure 2.9 (a)(b)(c) Simulated single flash spectrum in forward, transverse and backward directions ($\theta = 30, 90$ and 135°) in the laser polarization plane. (a′)(b′)(c′) Magnitude squared of Fourier transform of (a) (b) (c), showing sub-5fs initial flash burst followed by modulations at $\tau_p = 2\pi/\omega_p$, corresponding to laser-assisted injection, which are most clearly seen at $\theta = 90°$. The harmonics of ω_p and oscillations at τ_p are shown as vertical dashed lines. Here the plasma period is $\tau_p \approx 6.9\ fs$

As in the experiment, the simulation of I_S/I_P (Figure 4(d)) shows an increasing contribution of S-polarized radiation at transverse observation angles, except that at its peak, I_S/I_P is <1 in the experiment and >1 in the simulation. The peaking of I_S/I_P at transverse observation angles is likely an effect of coherence, as discussed below.

Aside from its detailed spectral dependence on the injected electron trajectories as discussed above, the flash's approximate overall wavelength range can be inferred from considerations of coherence and absorption. The effect of coherence is described by the structure factor $F(\mathbf{q}) = \left|\int d^3\mathbf{r}\, N_{e,rad}(\mathbf{r}) e^{i\mathbf{q}\cdot\mathbf{r}}\right|^2 \propto N_{e0}^2 e^{-\frac{1}{2}q^2(w^2 cos^2\theta + a^2 sin^2\theta))}$ applied to injection radiation originating from trapping at the plasma wave crest. Here **q** is the radiation wavevector and we take the distribution of radiating electrons through and across the crest as $N_{e,rad}(r) = N_{e0} e^{-z^2/w^2 - \rho^2/a^2}$, where the crest FWHM thickness from the simulation is $w_{fwhm} = 2\sqrt{ln2}\, w \sim 150nm$ and the bunch width is $a_{fwhm} = 2\sqrt{ln2}\, a \sim k_p^{-1} \sim 300nm$ (see Figure 5(b)). The structure factor predicts a short wavelength $1/e^2$ "coherence cutoff" at λ_{short}~ 300~400nm over a wide range of θ, in reasonable agreement with the experimental spectra . The long wavelength cutoff is set by the electron density in the crest, which at the time of injection peaks at $N_e/N_{cr} \sim 1 - 1.3$ in the simulation, giving a long wave cutoff $\lambda_{long} = 850 - 950nm$, also in reasonable agreement with the measured spectra.

While the laser-assisted injection mechanism ensures that S-polarized flash emission is weak at all angles θ, its relative contribution I_S/I_P peaks at transverse angles as seen in the experimental and simulation plots of Figure 4(d). This can be explained as a consequence of coherence by considering the classes of electrons

likely to radiate either more S-polarized radiation or more P-polarized radiation. The "class P" electron orbits originate in the laser polarization plane (*yz*), while class S orbits contributing to S-polarized radiation must originate close to the *xz* plane. At observation angle θ ~ 90°, $F_{P,S}(\mathbf{q}) \propto N_{e0,P,S}^2 e^{-\frac{1}{2}q^2 a_{P,S}^2}$, where $F_{P,S}$ is the structure factor applied to class P or class S electrons, $N_{e0,P,S}$ is the effective loc al electron density of injected class P or S electrons, and $a_{P,S}$ is the extent of their transverse distribution as viewed from θ~90°. Therefore, we take $a_S \sim 0$ and $a_P \sim k_p^{-1}$, and a rough estimate gives $I_s/I_p \sim F_s/F_p \sim (N_{e0,S}/N_{e0,P})^2 \, e^{\frac{1}{2}(\lambda_p/\lambda)^2}$, where λ_p is the plasma wavelength and λ can be taken as the peak flash wavelength. Using parameters from the simulation, $N_{e0,S}/N_{e0,P} \sim 0.1$ and $\lambda_p/\lambda \sim 3$, gives $I_s/I_p \sim 1$, in qualitative agreement with the experiment and simulation results.

2.6 Conclusions

In conclusion, we have measured in detail and characterized for the first time spectrally coherent radiation generated directly from a laser wakefield accelerator. This coherent, ultra-broadband, bright, and ultrashort pulse radiation flash originates from laser-assisted injection of electrons into the accelerating structure of the relativistic plasma wave. The flash is sufficiently bright to induce large nonlinear refractive index shifts in optical materials. Analysis of this injection radiation provides a detailed picture of the dynamics inside the laser plasma accelerator. We conclude that the injection process does not occur from pure wave-breaking: electrons are kicked into the accelerating phases of the plasma wave by the laser field. Under some conditions, periodic injections at the plasma period, which give rise to the first

observation of coherent radiation at harmonics of the plasma frequency, show that the plasma wave can remain coherent through the injection process. The initial burst of injection flash radiation was found to be no longer than approximately a single optical cycle in the visible spectrum. However, our measurements were limited by our probe pulse bandwidth and the low and high frequency cutoffs of the flash spectrum. It is likely that the flash burst duration is considerably shorter.

Chapter 3 Generation and optimization of Bessel beams

3.1 Introduction

In this chapter we present results on the generation of high intensity Bessel beams and optimization of their focal profiles using phase retrieval algorithms and adaptive optics. Section 3.2 gives a brief introduction to Bessel beam generation, particularly with reflective axicons. Section 3.3 presents fabrication of spiral phase plates for generation of high order Bessel beams. Section 3.4 discusses the effect of aberrations on focal profiles using analytical calculations and numerical simulations. Section 3.5 proposes a method using phase retrieval to extract the aberrations from a Bessel beam focal profile. Section 3.6 demonstrates the experimental optimization of Bessel focal profiles using adaptive optics.

3.2 Bessel beams

A generalized Bessel beam $E(\mathbf{r}_\perp, z) = u(\mathbf{r}_\perp)e^{i\beta z}$ is a type of propagation-invariant beam [60] constructed from the solution of the Helmholtz equation

$$\nabla_\perp^2 u + k_\perp^2 u = 0, \tag{3.1}$$

where $k_\perp^2 + \beta^2 = k^2 = n^2\omega^2/c^2$ and n is the local refractive index of the propagation medium. As all the rays of a Bessel beam are at the same angle $\gamma = \tan^{-1}(k_\perp/\beta)$ with respect to its propagation axis (z), a Bessel beam can reform after an obstacle in its propagation path. This "self-healing" property of Bessel beams leads to many applications. Bessel beams have been applied in a wide range of fields [61], such as optical trapping [62] , laser machining [63,64], optical coherence tomography [65].

High intensity Bessel beam have been applied to generating plasma waveguides for advanced accelerators [66] and to frequency conversion [67].

A Bessel beam based on a solution to Eq. (3.1) in cylindrical coordinates is $E(r,\phi,z) = A_0 \exp(ik_z z) J_m(k_\perp r)\exp(\pm im\phi)$, where J_m is the m-th order Bessel function, $k_z(=\beta)$ and $k_\perp$ are the longitudinal and transverse wave vectors, and ϕ is the azimuthal angle. A Bessel beam has infinite energy (as it is unbound in r), so only a quasi-Bessel beam with a finite radial cutoff can be generated in practice. However, we will still refer to our experimentally realized beams as Bessel beams.

There are many ways to generate a Bessel beam. Since the spatial frequency spectrum of a Bessel beam is an annulus in $k_x - k_y$ space, a Bessel beam can be generated by imposing a conical phase shift on a (high order) Gaussian beam, which involves axicons [68] , diffractive optical elements [69] or spatial light modulators [70]. Alternatively, it can be generated with an annular aperture placed on the back focal plane of a converging lens [60].

It can be shown that the electric field of quasi-Bessel beam from a refractive axicon is [71–73]

$$E(r,z) = E(\rho_\gamma)\left(\frac{2\pi k\rho_\gamma \sin\gamma}{\cos^2\gamma}\right)^{1/2} \exp\left[i\left(kz\cos\gamma + \frac{\pi}{4}\right)\right] \times J_0(kr\sin\gamma), \tag{3.2}$$

where γ is the ray approach angle, and $E(\rho_\gamma)$ is the incident field profile, and ρ_γ is determined by

$$\left\{[(z+\rho\tan\gamma)^2+\rho^2]^{\frac{1}{2}} - n\rho\tan\gamma\right\}_{\rho=\rho_\gamma} = z\cos\gamma. \tag{3.3}$$

For producing high intensity Bessel beams, the low damage threshold of spatial light modulators eliminates them from consideration. In this study we use customized reflective axicons for Bessel beam generation. The axicons are 2" diameter conical aluminum substrates with a protected gold coating and an on-axis hole of diameter $d =$

4 mm for injection of probe or guiding beams. The geometric axial length of the Bessel beam focal line is given by $L = \frac{D-d}{2tan\gamma}$.

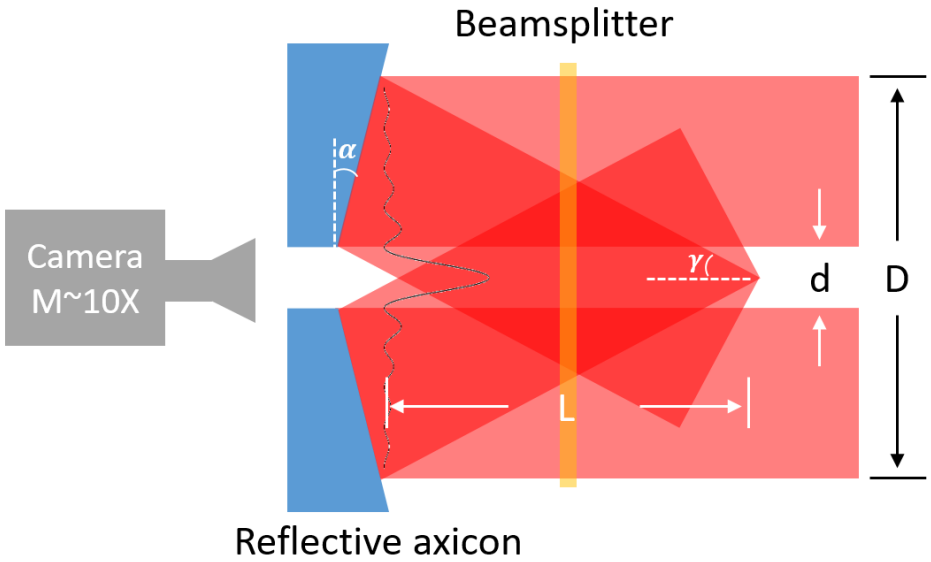

Figure 3.1 Reflective axicon setup. The CCD camera and translatable beamsplitter are used to measure the z-dependent Bessel beam focal profile.

To characterize the Bessel beam profile, a beamsplitter is used to partially reflect the Bessel beam to a CCD camera with ~10X magnification. By scanning the beamsplitter longitudinally on a translation stage, the Bessel beam profile along the whole focal line is measured as shown in Figure 3.2.

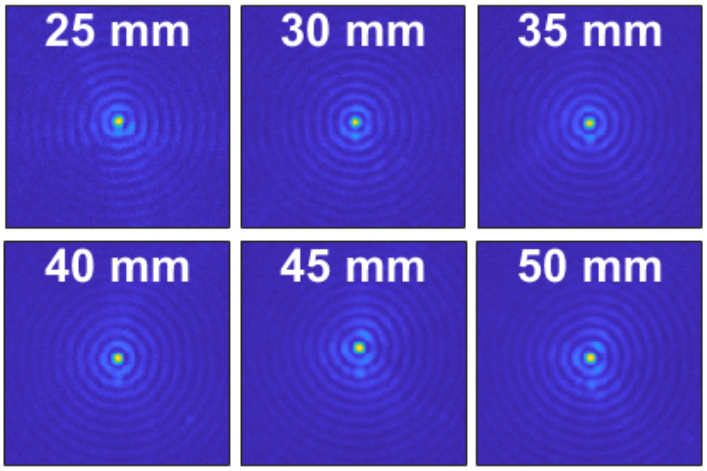

Figure 3.2 Sample longitudinal scan of J_0 Bessel beam profile. The indicated positions are the readings on the translation stage.

3.3 Generation of high order Bessel beams with spiral phase plates

A high order Bessel beam can be generated by illuminating an axicon with a high order Laguerre-Gauss beam [74]. The latter can be generated by imposing a helical phase front on a lowest order Gaussian beam. A helical phase front can be imposed by a spatial light modulator (SLM) [75] or by fixed diffractive optical elements [76] such as a hologram or phase plate. SLMs and typical holograms have a low damage threshold fluence ($\sim 200\ mJ/cm^2$) and a small aperture size ($<4cm^2$), so they are not a good choice for high intensity laser pulses. Here we use fused silica spiral phase plates (SPP) of various orders. The combination of an SPP and an axicon enables generation of high quality high order Bessel beams.

Spiral phase plates are among the large collection of diffractive optical elements (DOE) [77–79]. For a SPP with N steps for each 2π interval, using scalar diffraction theory it can be shown that the diffraction efficiency into the 0^{th} order is [77,79]

$$\eta = \left| sinc\left(\frac{\pi}{N}\right)\right|^2, \tag{3.4}$$

so that the diffraction efficiency of 4, 8 and 16 level SPPs are 0.81, 0.95 and 0.99.

All SPPs used in the experiments of this dissertation were 8-level elements (meaning 8 steps covering each 2π azimuthal interval), fabricated using photolithography and wet-etching [80] in the FabLab at the University of Maryland. We used a chromium coated, soda lime substrate photomask, with $3\mu m$ resolution, fabricated by Front Range LLC. A sketch of the procedure for making a 2-level element is shown in Figure 3.3. Following a similar procedure in two successive steps with finer division binary photomasks (see Figure 3.4) results in 8 levels. For our experiments, we fabricated two SPPs: one with azimuthal phase circulation $16\pi\,(m = 8)$ and the

other with phase circulation $32\pi\,(m = 16)$, or topological charges 8 and 16. The $m =$ 8 plate had 64 discrete phase steps while the $m = 16$ plate had 128 steps.

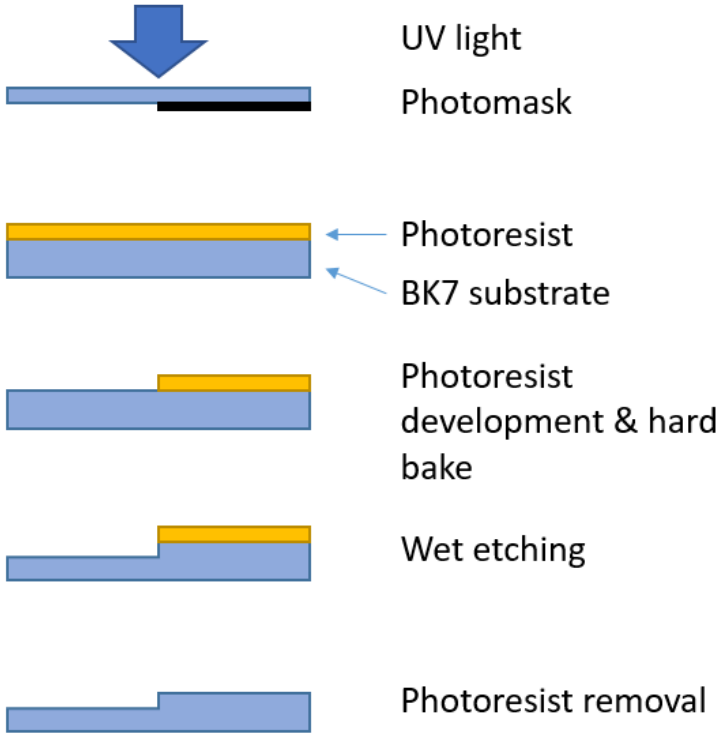

Figure 3.3 Fabrication of 2-level diffractive optical element

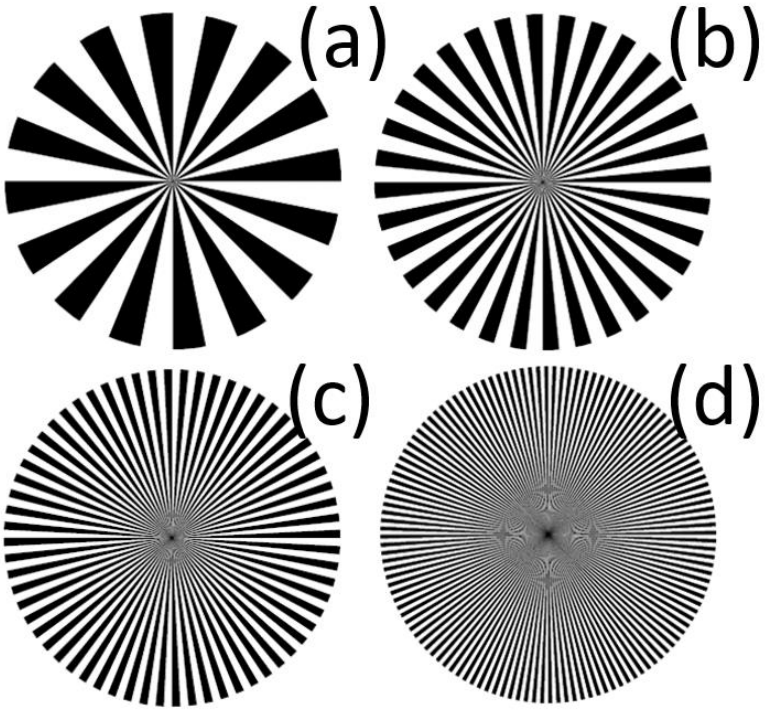

Figure 3.4 (a)-(d) Binary phase masks used in fabrication with 16, 32, 64 and 128 steps.

In order to characterize the quality of our SPPs, we put a $m = 8$ phase plate before a 10° base angle transmissive axicon and measured the focal spot profile generated with λ=780 nm diode laser illumination. From Figure 3.5 it is seen that the SPP combined with an axicon generates a high order Bessel beam (J_8). The azimuthal modulation on the rings originates from the plate's 8-level azimuthal phase profile.

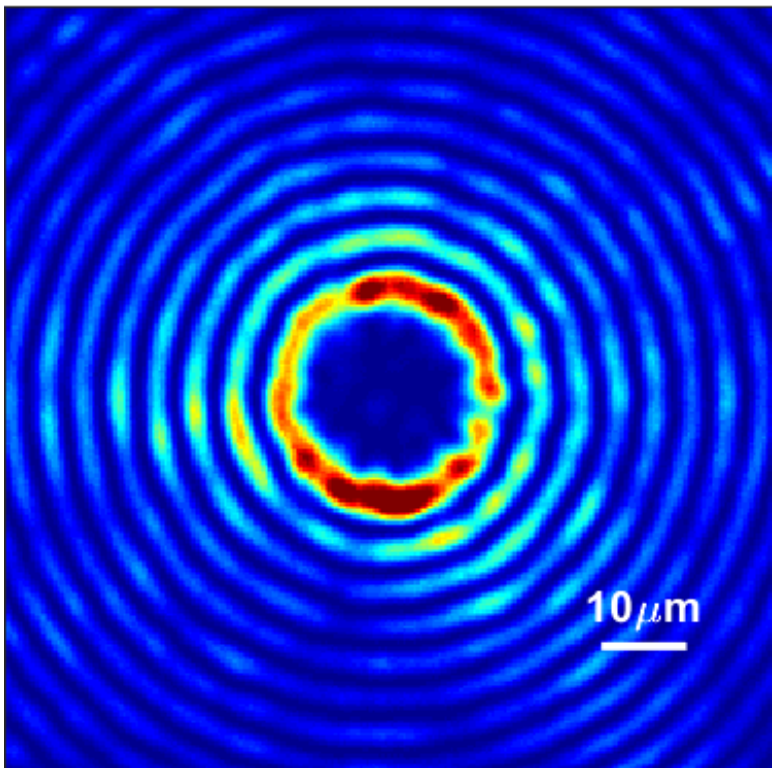

Figure 3.5 Measured J_8 focus from homemade $m = 8$ SPP with a 10° base angle transmissive axicon.

3.4 Bessel beams with aberration

In this section we study the effect of primary aberrations on Bessel beam profiles. Bessel beam aberrations originate not only from aberrations in the illuminating beam, but also from the surface profile and alignment of the axicon. The Bessel beam focus

from axicons under oblique illumination (studied since the 1990s [81,82]) shows a caustic pattern characteristic of astigmatism. The axicon surface profile deviates from an ideal conical surface due to errors in manufacturing, e.g. an elliptical cone instead of a circular cone [83]. The mounting method may also affect the axicon surface profile due to mechanical stress. Common three-prong mirror mounts tend to impose trefoil aberrations on the Bessel beam focal profile.

Assuming the incoming electric field is azimuthally symmetric, $E(\rho,\alpha) = E(\rho)\exp(i\psi(\rho))\exp(i\phi(\rho,\alpha))$, where $\phi(\rho,\alpha) = B(\rho)\cos(m\alpha+\eta)$ represents the aberration and $\psi(\rho) = -2k\rho\tan\vartheta$ is the phase imposed by the axicon (ϑ is the base angle of the axicon, $\vartheta \ll 1$).

A full treatment of aberrations can be found in [56]. For a circular aperture, aberrations are usually expanded by Zernike polynomials $Z_n^m(\rho,\alpha) = R_n^m(\rho)\cos m\alpha$. Aberrations involved in this chapter are shown in Table 3.1.

Type of aberration	n	m	Expression
Spherical aberration	4	0	$\sqrt{5}(6\rho^4 - 6\rho^2 + 1)$
Horizontal Coma	3	1	$\sqrt{8}(3\rho^3 - 2\rho)\cos\alpha$
Vertical Coma	3	-1	$\sqrt{8}(3\rho^3 - 2\rho)\sin\alpha$
Vertical Astigmatism	2	2	$\sqrt{6}\rho^2\cos 2\alpha$
Oblique Astigmatism	2	-2	$\sqrt{6}\rho^2\sin 2\alpha$
Defocus	2	0	$\sqrt{3}(2\rho^3 - 1)$
X-Tilt	1	1	$2\rho\cos\alpha$
Oblique trefoil	3	3	$\sqrt{8}\rho^3\cos 3\alpha$
Vertical trefoil	3	-3	$\sqrt{8}\rho^3\sin 3\alpha$

Table 3.1 Aberrations involved in this chapter.

In practice, for moderately distorted Bessel focus, (see Figure 3.9(b)(e)), $B(\rho) \lesssim 1$. The electric field at a particular plane at z is calculated as

$$U(r,z,\theta) = \iint E(\rho,\alpha)\exp(ikL)/L \ \ \rho d\rho d\alpha. \tag{3.5}$$

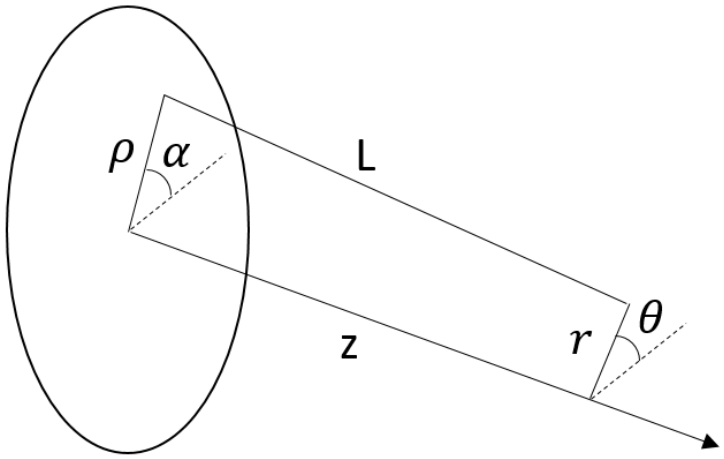

Figure 3.6 Parameters to calculate axicon focal profile.

Applying the paraxial approximation, the integral is simplified as

$$U(r,z,\theta) = \frac{\exp\left(ikz+\frac{ikr^2}{2z}\right)}{z}\iint E(\rho)\exp\Big[ik\Big(\frac{\rho^2}{2z} - 2\rho\tan\beta - \frac{\rho r}{z}\cos(\theta-\alpha) + \phi(\rho,\alpha)\Big)\Big]\rho d\rho d\alpha. \tag{3.6}$$

The exponent term is rewritten with Jacobi-Anger expansion

$$\exp(iz\cos\theta) = \sum_{n=-\infty}^{\infty} i^n J_n(z) e^{in\theta}. \tag{3.7}$$

Therefore,

$$U(r,z,\theta) = \frac{\exp\left(ikz+\frac{ikr^2}{2z}\right)}{z}\int E(\rho)\exp\left[ik\left(\frac{\rho^2}{2z} - 2\rho\tan\vartheta\right)\right]\times \int\Big(\sum_{n=-\infty}^{\infty} i^n J_n\left(-\frac{k\rho r}{z}\right)e^{in(\theta-\alpha)}\Big)\Big(\sum_{q=-\infty}^{\infty} i^q J_q\big(B(\rho)\big)e^{iq(m\alpha+\eta)}\Big)\rho d\rho d\alpha. \tag{3.8}$$

Applying the method of stationary phase and using $\int_0^{2\pi} e^{in\alpha}d\alpha = 2\pi\delta_{n0}$, we obtain

$$U(r,z,\theta) = \frac{\exp\left(ikz+\frac{ikr^2}{2z}\right)}{z}\exp\left(-i\left(k\rho_0\tan\vartheta + \frac{\pi}{4}\right)\right)\left(\frac{(2\pi)^3}{k\rho_0\tan\beta}\right)^{\frac{1}{2}}E(\rho_0)\times \sum_{q=-\infty}^{\infty}(-1)^{qm}i^{q(m+1)}e^{iqm\theta+iq\eta}J_q\left(B(\rho_0)\right)J_{mq}(2kr\tan\vartheta), \tag{3.9}$$

$$\rho_0 = 2z\tan\vartheta. \tag{3.10}$$

We have assumed $r \ll \rho$, which is reasonable in our experiment, as $r{\sim}10\mu m$ and $\rho{\sim}10mm$. For high order Bessel beams, the only change is to replace all the qm terms above as $qm+\mu$, where μ is the order of the Bessel beam, as shown in (3.11).

$$U(r,z,\theta) = \frac{\exp\left(ikz+\frac{ikr^2}{2z}\right)}{z}\exp\left(-i\left(k\rho_0\tan\vartheta + \frac{\pi}{4}\right)\right)\left(\frac{(2\pi)^3}{k\rho_0\tan\beta}\right)^{\frac{1}{2}}E(\rho_0)\times \sum_{q=-\infty}^{\infty}(-1)^{qm+\mu}i^{q(m+1)+\mu}e^{i(qm+\mu)\theta+iq\eta}J_q\left(B(\rho_0)\right)J_{qm+\mu}(2kr\tan\vartheta). \tag{3.11}$$

Therefore, the Bessel focus profile at a particular z is determined by the local phase aberration at $\rho = \rho_0$. Usually, $J_q(B)$ decays quickly for increasing q, as shown in Figure 3.7, so it suffices to cut off q in the sum of (3.9) and (3.11) at $q = 10$.

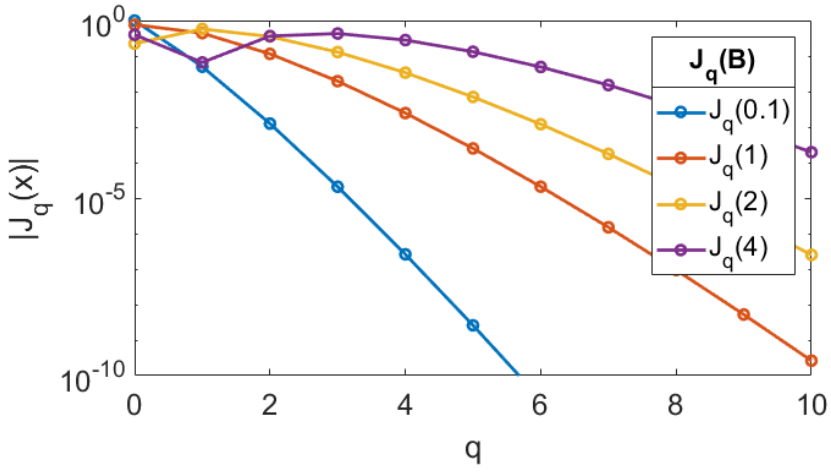

Figure 3.7 Cutoff behavior of $J_q(B)$

We compare the result of the analytical expression (3.9) with the inverse FFT of a spatial frequency space representation of the Bessel beam, taken as a Gaussian ring multiplied by an aberration factor, $f(\mathbf{k}) = \exp\left(-\left(\frac{|\boldsymbol{k}|-k_0}{w}\right)^2\right)\exp(im\alpha + i\phi(\alpha))$, where w is a scale length in wavenumber space same as the FFT grid size. As an example, for oblique trefoil, $\phi(\alpha) = B\cos 3\alpha$. In Figure 3.8, we show the effect of oblique trefoil on a J_0 beam. The numerical result is in good agreement with the (3.9), except for the exponential decay near the periphery of the image due to the finite width of the ring in k-space. This difference can be compensated by imposing an amplitude mask on the beam intensity measurement. Since FFT is easier to handle than (3.11), we use FFT for phase retrieval in this chapter.

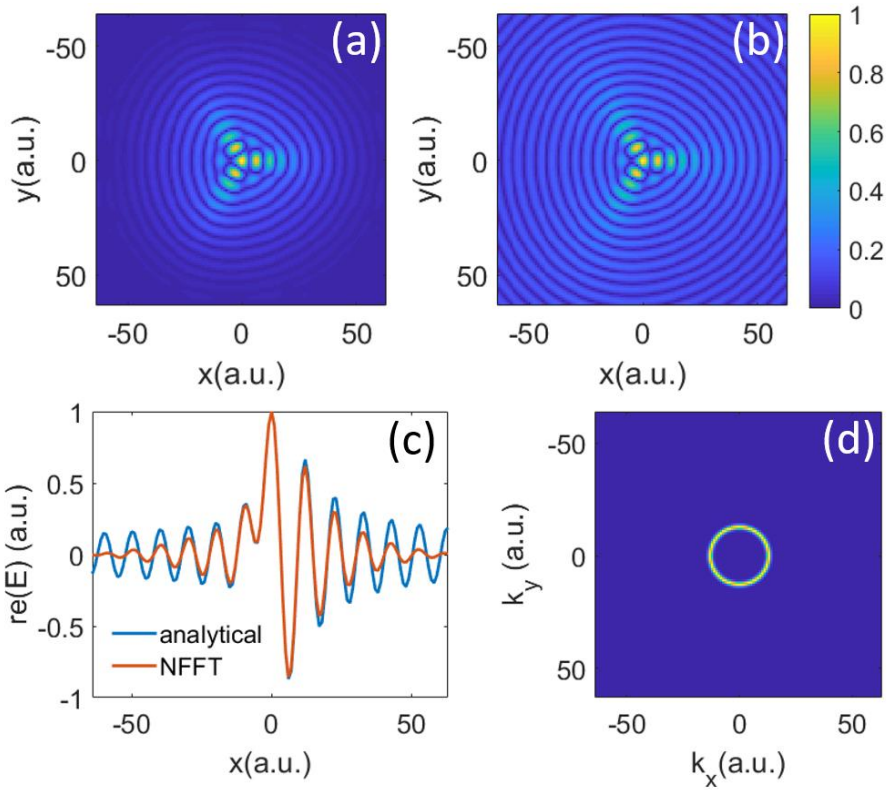

Figure 3.8 Comparison of trefoil-aberrated J_0 focal spot intensity calculated using (a) an inverse FFT and (b) the (3.9) (top right), both for B=1. Panels (a) and (b) share the

same color scale. (c) Lineouts along y=0 in (a) and (b). (d) Spatial frequency spectrum $|f(\mathbf{k})|^2$.

In Figure 3.9 we demonstrate the effect of vertical astigmatism and oblique trefoil on J_0 and J_{16} Bessel beams, with the aberrations modeled as $\phi(\rho, \alpha) = B \cos m\alpha$. As shown in Table 3.1, m=2 for astigmatism and m=3 for trefoil. The results are plotted and compared with experimental measurements. The similarity indicates the presence of clear astigmatism and trefoil that must be corrected in order to improve the focal spot quality.

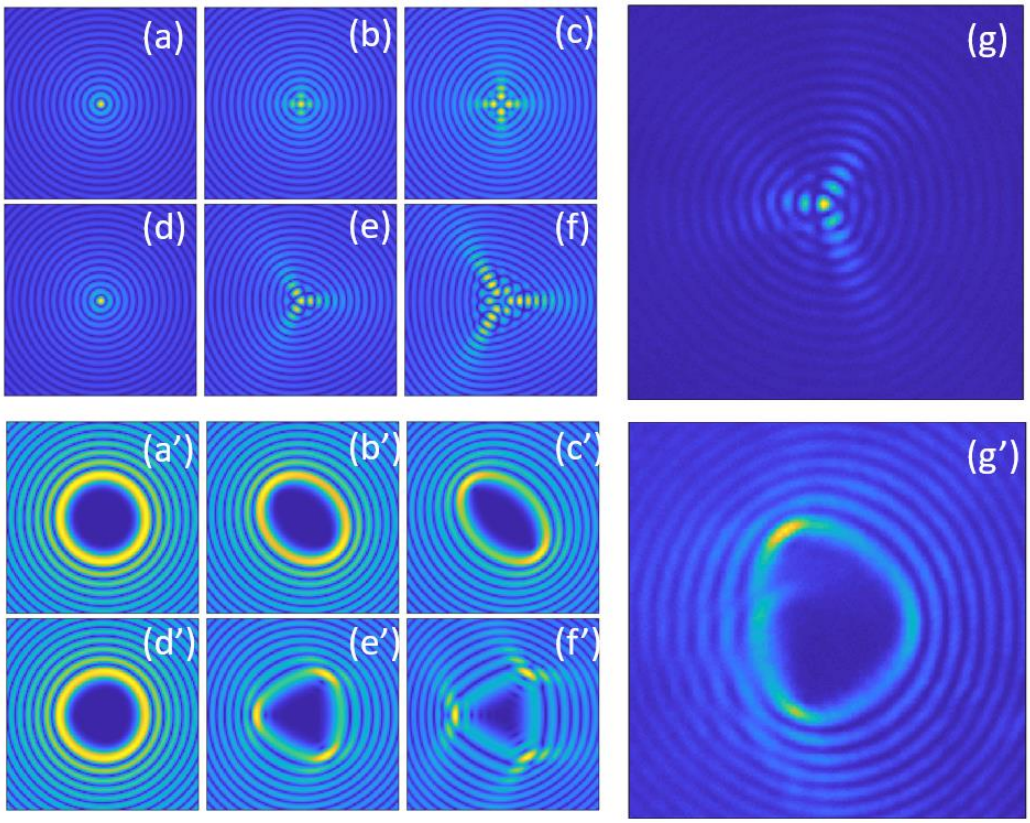

Figure 3.9 Effect of astigmatism and trefoil on Bessel beam of different orders. (a)-(c) show J_0 focus affected by vertical astigmatism with B = 0.1,1 and 2 respectively. (d)-(f) show J_0 focus affected by oblique trefoil with same values of B. (a')-(f') shows J_{16} focus affected by the same aberrations as (a)-(f) respectively. (g) and (g') show measured J_0 and J_{16} focus in experiment.

It is worth noting that coma (see Table 3.1) does not affect the Bessel focal profile but translates the focus in space [84]. Since coma is represented by $\phi(\rho,\alpha) = B(\rho)\cos\alpha$ or $\phi(\rho,\alpha) = B(\rho)\sin\alpha$, when ρ is fixed (a particular z location) it is equivalent to tilt and only causes translation of the focus depending on $B(\rho)$. Effectively, this means that the Bessel beam centroid follows a curved path if $\frac{d^2B}{d\rho^2} \neq 0$ [85]. With a carefully designed $\phi(\rho,\alpha)$, the "curving" Bessel beam may find interesting applications [86].

3.5 Phase retrieval of Bessel beams

A common way to correct aberrations in focused beams is to first measure the phase front using a linear technique. There are numerous ways to measure laser wave front and we list four of them here. The first is the Shack-Hartmann sensor [87], which divides the beam into an array of discrete intensity points using a microlens array. Deviation from reference focal spots field indicates wavefront distortion. The second type is shearing interferometer, where a beam interferes with its spatially shifted replica. The gradient of phase front can be extracted from the interferogram. Both methods have been applied to measurement of Bessel beam or axicon surface profile with sufficiently small approach angle [88–90]. The third way is linear interferometry with a reference wavefront, generated by e.g. computer generated holograms [91] or optical inner surface [92]. The additional reference wavefront, though increasing the accuracy in measurement, makes it less adaptable to Bessel beam of various approach angle. Unlike the three ways mentioned, the fourth way relies only on the intensity measurement of the laser beam along various propagation distance. The gradient of

phase front can be calculated by transport of intensity equation (TIE) [93] $\nabla_\perp \cdot [I(\boldsymbol{r}_\perp, z)\nabla_\perp \phi(\boldsymbol{r}_\perp, z)] = -k\partial_z I(\boldsymbol{r}_\perp, z)$ in an iterative approach [94]. Here the laser propagates along z, ϕ is the phase front, k is the wavenumber and I is laser intensity. This inspired our new method, as proposed below.

Bessel beam is a special case in that the focal spot profile in each z location is determined by the beam at the corresponding radius, according to the last section. The focal spot profile can be derived by Fourier transform of a "ring" shaped spatial frequency spectrum, combined with specific wavefront distortion. Therefore, it is possible to extract the wavefront of Bessel beam over the full aperture by intensity measurement along z alone, by phase retrieval.

In this section, we present a method for optimizing a Bessel beam focal profile based on phase retrieval and adaptive optics. This represents an active manipulation of the Bessel beam focus, which may find application in a wide range of fields.

The problem reduces to finding the intensity and phase of the Bessel beam's spatial frequency representation $\tilde{F}(\mathbf{k})$ given the amplitude of its inverse Fourier transform $|F(\mathbf{r})|$. This is a two-dimensional phase retrieval problem. For most of the problem of interest, such as coherent diffraction imaging, the object function $F(\boldsymbol{r})$ has finite support [95]. Here in 2D the support means the set of points over which the object is not zero. The complex version of the problem demands tighter (sharper) support [96,97].

Fortunately, there exists tight support in k-space, because for an ideal Bessel beam the spatial frequency spectrum is $\tilde{F}(\mathbf{k}) \propto \delta(|\mathbf{k}| - |\mathbf{k}_{\perp 0}|)$, where $|\mathbf{k}_{\perp 0}|$ is the spatial

frequency of the conical wave front of the Bessel beam. This constraint leads to good convergence of phase retrieval, as shown below.

Phase retrieval has been an active field of research over the past 40 years, for which a variety of algorithms have been developed [98]. Some are based on gradient descent, such as Error Reduction (ER) [99] and Hybrid-Input-Output (HIO) [95]. Some are based on convex optimization [100], ptychography [101] and more recently, machine learning [102,103]. There is research on comparing the performance of these algorithms with a common data set [104], where ER and HIO still show best performance in phase retrieval error of a modified air force resolution target [104]. Therefore, we used a combination of ER and HIO for phase retrieval of Bessel beams.

The algorithm is summarized in Figure 3.10. Essentially, it performs projection between the object space constraint and spectral space constraint. In the case of Bessel beams, the object space constraint is the measured Bessel focus profile, and the spectral space constraint is an infinitely thin annulus (replaced by a finite width annulus for computation). We define the object space constraint as F, the spectral space constraint as G, the n^{th} iteration in object space as $f_n^{ER,HIO}$, and the n^{th} iteration in spectral space as $g_n^{ER,HIO}$. Then the projection operator to object space is defined as $P_o(g) = |F|\frac{\mathcal{F}(g)}{|\mathcal{F}(g)|}$, where $\mathcal{F}$ represents Fourier transform.

The projection operator to spectral space for ER is defined as

$$P_s^{ER}(f^{ER}) = |G|\frac{\mathcal{F}^{-1}(f^{ER})}{|\mathcal{F}^{-1}(f^{ER})|}. \tag{3.12}$$

For initialization,

$$G = \begin{cases} S_0, if|S_0| > \epsilon^{ER} \\ 0, otherwise \end{cases}, S_0 = \exp(-\left(\frac{k-k_0}{w}\right)^2). \tag{3.13}$$

The projection operator to spectral space for HIO in the nth iteration is defined as

$$P_s^{HIO}(f^{HIO}) = \begin{cases} S_0\mathcal{F}^{-1}(f^{HIO}), S_0 > \epsilon^{HIO} \\ S_0[g_n^{HIO} - \beta\mathcal{F}^{-1}(f^{HIO})], otherwise \end{cases}. \tag{3.14}$$

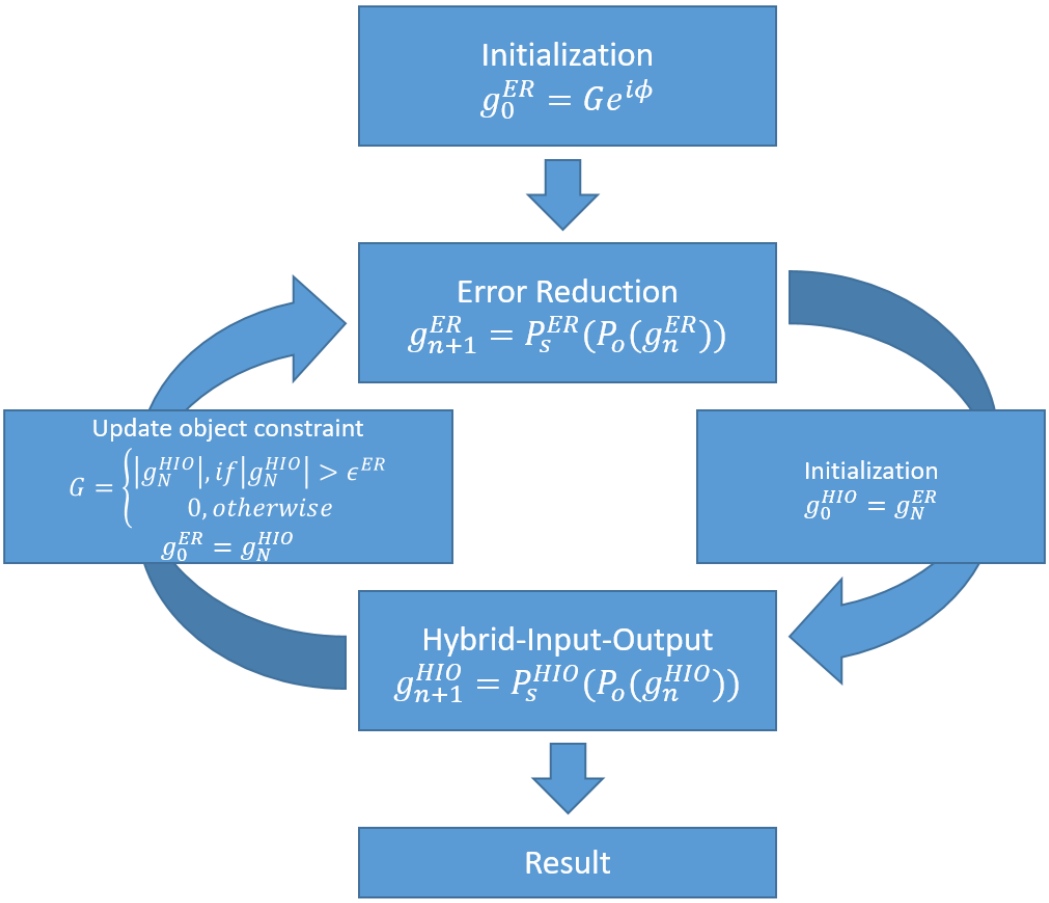

Figure 3.10 Flow chart of the phase retrieval algorithm

The typical choice of parameters is summarized in table 3.1. To initialize, $g_0^{ER} = Ge^{i\phi_{init}}$, where ϕ_{init} is a random matrix of phase. Usually, convergence requires 10 cycles of ER and 20 cycles of HIO. The convergence of calculation is defined as

$convergence = sqrt(min_{\mu} \frac{\sum(|F_{real}|-\mu|F_{rec}|)^2}{\sum|F_{real}|^2})$, where F_{real}, F_{rec} represent the real focus amplitude and reconstructed amplitude. The summation is over the full object domain.

Parameter	ϵ^{ER}	ϵ^{HIO}	β	k_0
Value	1e-6	1e-2	0.9	Determined by Bessel beam profiles

Table 3.2 Typical choice of parameters in the algorithm

There is an intrinsic ambiguity in phase retrieval related to complex conjugation i.e. $|\mathcal{F}^{-1}[g(\boldsymbol{k})]| = |\mathcal{F}^{-1}[g^*(-\boldsymbol{k})]|$. The phase of $g(k)$ can be decomposed into azimuthal modes,

$$g(\boldsymbol{k}) = |g(\boldsymbol{k})| \exp[i\phi(k,\theta)], \tag{3.15}$$

$$\phi(k,\theta) = i\sum_m \mathrm{B_m(k)} \cos(m\theta + \eta_m). \tag{3.16}$$

Then the ambiguity means $|g(\boldsymbol{k})| \exp[i\phi(k,\theta)]$ and $|g(-\boldsymbol{k})| \exp[-i\phi(k,\theta+\pi)]$ have the same inverse Fourier transform amplitude. If $|g(\boldsymbol{k})| = |g(-\boldsymbol{k})|$, which is usually the case for Gaussian beam, the all the even order azimuthal terms of $\phi(k,\theta)$ have a sign ambiguity.

We propose two ways to resolve this ambiguity. First, in practice, if the inversion symmetry of $|g(\boldsymbol{k})|$ can be broken (e.g., dampen some part of the beam experimentally or numerically), then the ambiguity can be resolved by choosing the correct orientation of $|g(\boldsymbol{k})|$ by comparing with input beam profile. Second, we can impose a known helical phase term to $g(\boldsymbol{k}) \rightarrow g(\boldsymbol{k})e^{il\theta}$, which essentially turns the diffraction pattern into high order Bessel beam. Since the helicity of the additional phase is known, it is easy to tell the correct $g(\boldsymbol{k})$ from its complex conjugate.

As a demonstration, we show phase retrieval from the diffraction pattern $g(\mathbf{k}) \approx \delta(|\mathbf{k}| - k_0)(1 + 0.5\cos\theta)\exp(i\cos 3\theta)$ in Figure 3.11. A low-pass filter is applied to remove azimuthal terms above $m = 6$. The case without noise ((c) and (d)) shows better amplitude in spectral space and the root-mean-square (RMS) phase error is 0.096. To test the robustness against noise, we added white noise with maximum as 1% of the peak pixel value. The case with 1% noise ((e) and (f)) shows RMS phase error of ~0.11 rad, although the amplitude in spectral space is only qualitatively close to the model (a). Overall, the method reaches phase accuracy less than 0.02 waves, even with 1% noise.

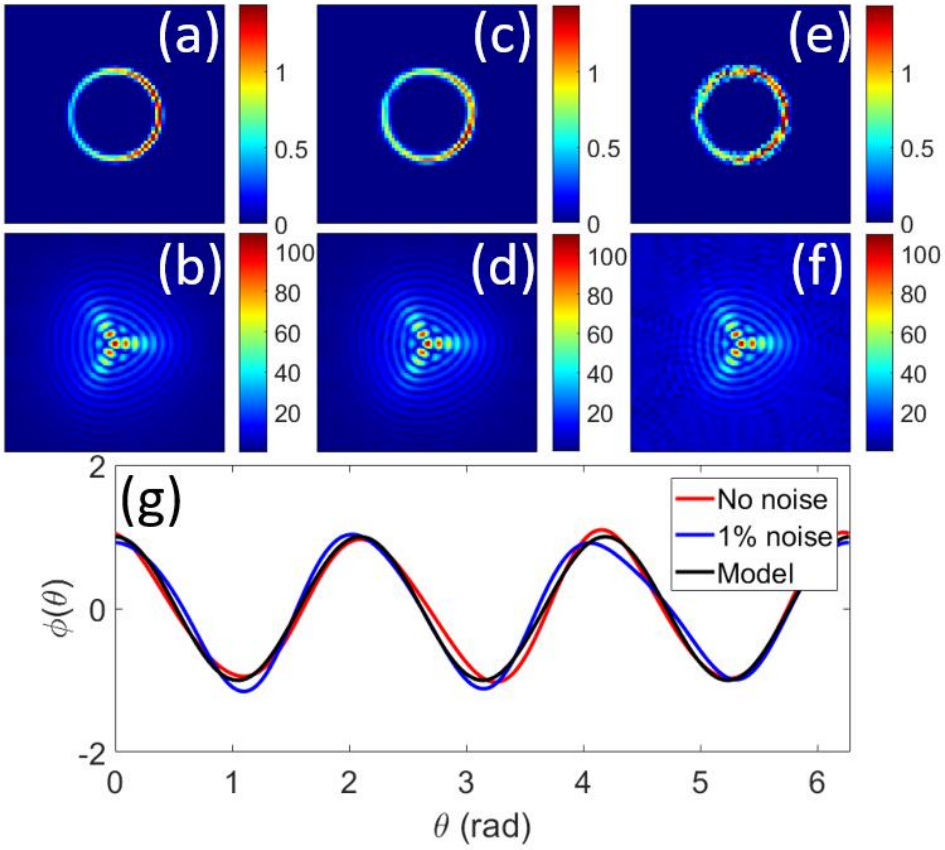

Figure 3.11 Phase retrieval of a model J_0 diffraction pattern with trefoil. (a)(b) Amplitude in spectral and object space. (c)(d) Retrieved amplitude in spectral and object space without noise. (e)(f) Same as (c)(d) but with 1% noise added to (b). (g)

Comparison of extracted phase. The root mean square error of reconstruction is 0.096 and 0.11 without and with 1% additive noise.

High order Bessel beams can be reliably reconstructed as well without ambiguity, if the order is known explicitly. In Figure 3.12, we show phase retrieval of a J_8 beam with astigmatism and trefoil $g(\mathbf{k}) \approx \delta(|\mathbf{k}| - k_0)(1 + 0.5\cos\theta)\exp(i(\cos 2\theta + 0.5\cos 3\theta) + 8i\theta)$. The case without noise ((c) and (d)) shows 0.022 rad RMS phase error, and the case with 1% noise ((e) and (f)) shows ~0.078 rad RMS phase error. With a high order Bessel beam, the retrieved spectral amplitude is much closer to the model. This is probably due to the property of HIO, since it tends to stagnate between the real image and its complex conjugate, which are much easier to distinguish in the case of high order Bessel beams. Overall, with 1% noise, the method reaches phase accuracy of ~0.01 waves.

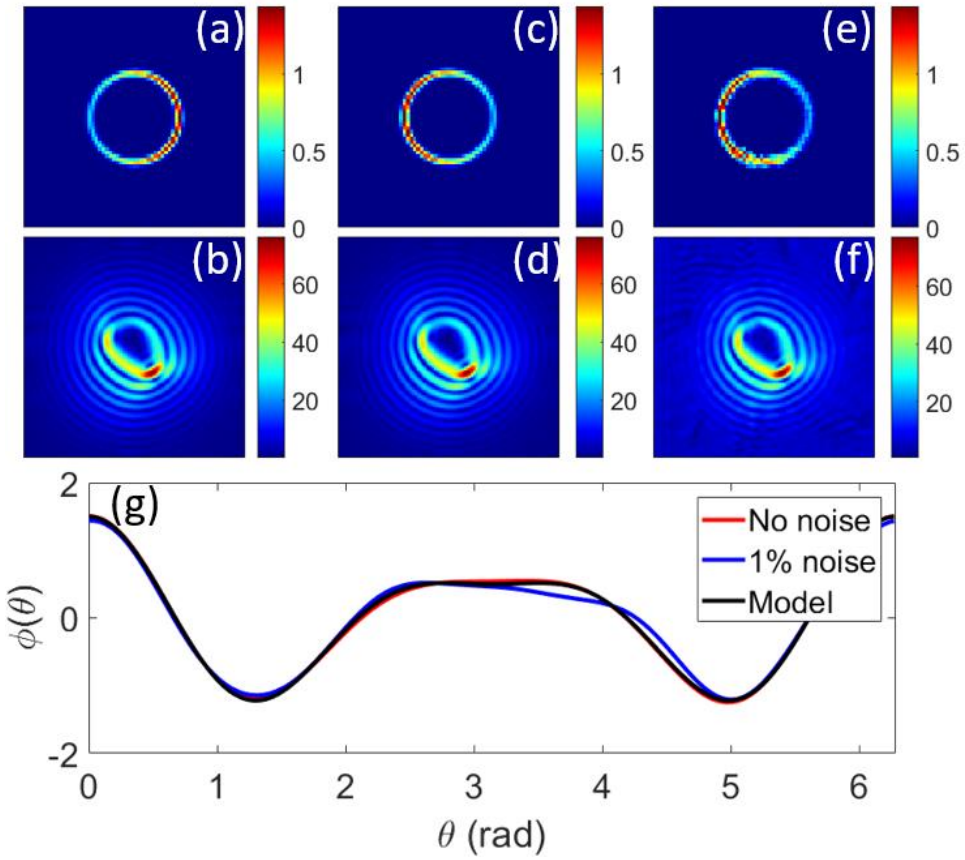

Figure 3.12 Phase retrieval of a model J_8 diffraction pattern with astigmatism and trefoil aberrations. (a) (b) Amplitude in spectral and object space. (c)(d) Retrieved amplitude in spectral and object space without noise. (e)(f) Same as (c)(d) but with 1% noise added to (b). (g) Comparison of extracted phase. The RMS error of reconstruction is 0.022 and 0.078 waves without and with 1% additive noise.

In conclusion, we applied a combination of ER and HIO algorithm to reliably retrieve the phase of Bessel beams of different orders. Phase ambiguities occur, but they can be resolved by breaking the inversion symmetry of the beam. Numerical tests show that the algorithm is accurate up to ~0.1 rad in RMS phase error.

3.6 Optimization of Bessel focal profiles with adaptive optics

In this section, we experimentally optimize Bessel beam focal profiles using a deformable mirror (DM). Previous effort to improve Bessel focal profiles mainly

involved tilting axicon to compensate non-ideal axicons [105], or optimization of the axial profile the on-axis intensity using a SLM [106].

From the results of previous sections, we are able to extract aberrations from the Bessel beam focal profile. The corresponding correction terms are added to the surface profile of a bimorph deformable mirror (NightN). Leakage of the beam through a mirror is sent to a shearing interferometry wavefront sensor (SID4, Phasics) to determine the phase corrections needed to operate the DM. The modified Bessel focus is subsequently analyzed and new correction terms added again to the DM, forming a closed loop and the Bessel focus is iteratively optimized.

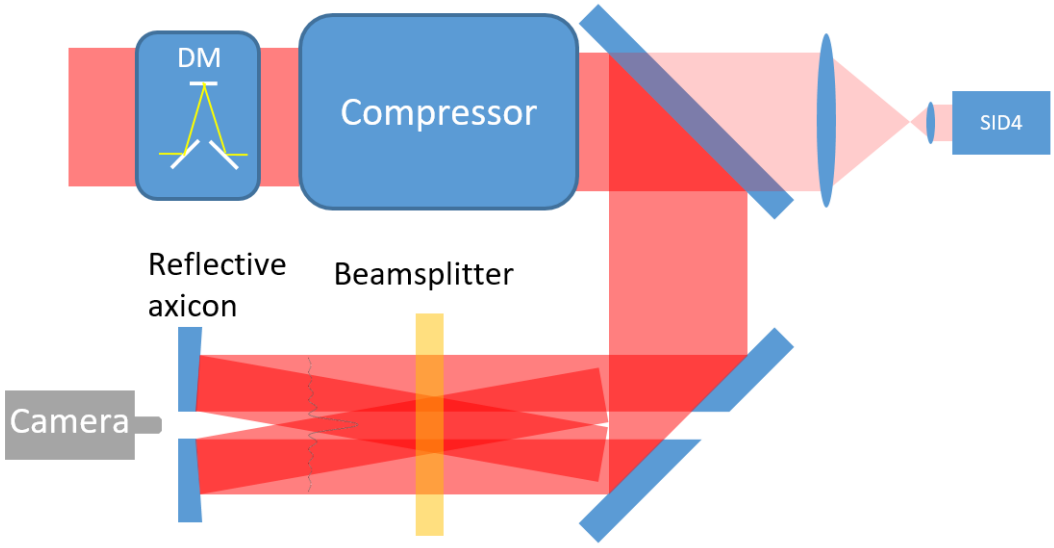

Figure 3.13 Experimental setup for closed loop optimization of Bessel beam focus. "DM" refers to the deformable mirror. The beamsplitter is scanned with a 100-mm travel translation stage (Standa). The reflected Bessel beam is imaged by a camera (Stingray F046B) with a 10X objective.

Since the deformable mirror had a limited number of modes (eigenmodes of the mirror actuator transfer matrix) with high stability (determined by the number of actuators), we only corrected primary astigmatism (see Table 3.1) and trefoil. To start,

we used a J_0 beam. To simplify the procedure, we only corrected the focal spot close to the end of the focal line (see the "90 mm" image in Figure 3.14). Typically, we found the aberration to be most significant at the outer aperture of the axicon. The larger aberration at outer aperture is attributed to axicon manufacturing error and can also be seen from Zernike polynomials (Table 3.1). Strictly speaking, this correction is optimal only for a particular annulus on the axicon, because the radial distribution of aberration is unlikely to follow a single Zernike polynomial. For correction over the full axicon aperture, phase retrieval needs to be carried out along the whole length of the focal line and the correction involves higher order radial and azimuthal terms in Zernike polynomials. There terms are difficult to correct due to the limited actuators on the DM.

With the correction for 90 mm in place, the focal profiles of the Bessel beam were recorded at discrete z positions. At each z position, we turned the DM voltage on and off to record the focal spot profile with and without correction, as shown in Figure 3.14. For correction of a J_{16} Bessel beam, we kept the same DM correction (assuming the SPP imposes negligible aberration), inserted a $m = 16$ spiral phase plate before the deformable mirror, and repeated the same measurement as shown in Figure 3.15.

Correction by the deformable mirror improved the focal spot profile significantly along the whole focal line as we could measure. Before correction, the focal spot profiles in Figure 3.14 and 3.15 indicated astigmatism and trefoil, due to axicon alignment and mounting. After correction, the focal spot profiles near the end of the focal line shows clear maximum on axis for J_0 beam and circular ring for J_{16} beam. The intensity variation on the first bright ring of J_{16} beams was due to the azimuthal non-uniformity of the illuminating laser beam.

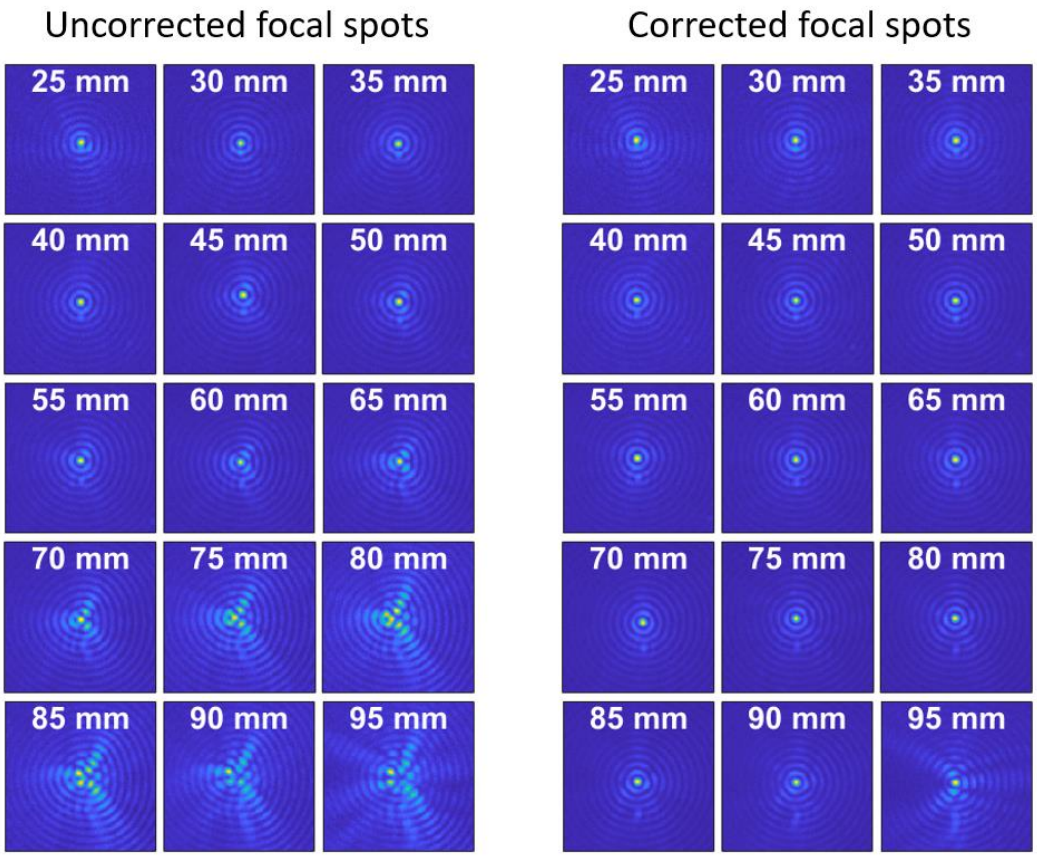

Figure 3.14 Bessel focal profile optimized using a deformable mirror (DM). The columns on the left show uncorrected J_0 focal images taken at the z positions labeled in each panel. The columns on the right show corrected J_0 focal spot images taken at the same positions, using DM settings determined by the correction at 90 mm.

3.7 Conclusion

In this chapter we discussed fundamental and high order Bessel beams with aberrations, and how to diagnose and correct for them. High order Bessel beams were generated using a reflective axicon plus a spiral phase plate. We fabricated discretized spiral phase plates of various orders with lithography and wet etching.

An analytical expression for the aberrated Bessel beam focal profile was developed and compared with numerical calculation. We applied a combination of the Error Reduction and Hybrid-Input-Output algorithms to iteratively retrieve the aberrations of

Bessel beams from intensity profile measurements. Using adaptive optics, we successfully applied the method to correct both low and high order Bessel focal profiles and demonstrated significant improvement.

The techniques developed in this chapter may be important to applications requiring high quality Bessel beams, such as their use in this dissertation for OFI-based plasma waveguide generation. Specifically, corrected Bessel focal profiles are applied in the next chapter to generate long (~10 cm), tubular plasmas as waveguides for intense laser pulses. In addition, the ability to control the phase of a Bessel beam opens the possibility of manipulating Bessel beam propagation.

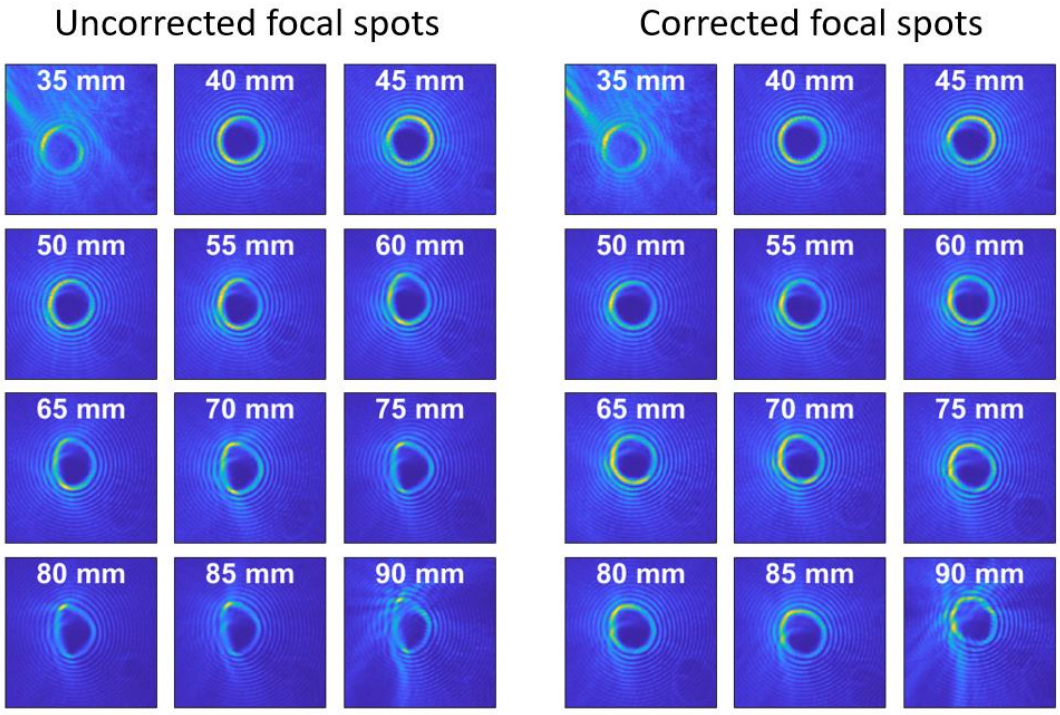

Figure 3.15 Bessel focal profile optimized using a deformable mirror (DM). The columns on the left show uncorrected J_{16} focal spot images taken at the z positions labeled in each panel. The columns on the right show corrected J_{16} focal spot images taken at the same positions, using DM settings determined by the correction at 90 mm for a J_0 beam.

Chapter 4 Generation of low density plasma waveguide

4.1 Introduction to plasma waveguides

Many applications of high intensity lasers demand an extended length of laser-matter interaction. For a Gaussian beam propagating in free space, the laser intensity decreases by half after propagation by a Rayleigh length $Z_R = \pi w_0^2/\lambda$, where w_0 is the beam waist. Without a guiding structure, this interaction length is limited to approximately a confocal parameter (twice the Rayleigh length) due to diffraction. A high intensity laser pulse will cause ionization in a glass dielectric waveguide when $I > \sim 10^{13} W/cm^2$ [107]. Plasma, which is the medium of interest for many high intensity laser experiments, is already ionized and is an important medium for waveguiding structures. In the following, we briefly review the mode structure [108] and some formation schemes for plasma waveguides.

4.1.1 Optical mode structure of the plasma waveguide

We start with the Fourier transformed wave equation

$$\nabla^2 \boldsymbol{E} + \frac{\omega^2}{c^2}\epsilon \boldsymbol{E} = \nabla\left(-\boldsymbol{E} \cdot \frac{\nabla\epsilon}{\epsilon}\right), \tag{4.1}$$

with $\epsilon\mu = n^2$, where ϵ is the dielectric function of the medium, $\mu \sim 1$ is the magnetic permeability for a nonmagnetic medium, and n is the refractive index. For weak variation of ϵ along the propagation direction (z), then the ratio of the RHS (polarization term) to the first term is $\left|\frac{\nabla\left(-\boldsymbol{E}\cdot\frac{\nabla\epsilon}{\epsilon}\right)}{\nabla^2\boldsymbol{E}}\right| \sim \frac{L_t}{L_\epsilon}$, where L_t and L_ϵ are the transverse scale lengths for variation of the electric field and the refractive index. For bound modes of waveguides, the fields are confined well within the transverse

structures so that $L_t \ll L_\epsilon$, and the RHS is usually neglected. Therefore, the solutions to Eq. 4.1 can be TEM modes $E(\mathbf{r}_\perp, z) = u(\mathbf{r}_\perp)e^{i\beta z}$, where β is the waveguide propagation wave number. Substituting into Eq. (4.1) gives

$$(\nabla_\perp^2 - k_\perp^2)u(\boldsymbol{r}_\perp) = 0, \tag{4.2}$$

with

$$k_\perp^2 = \frac{\epsilon\omega^2}{c^2} - \beta^2 = \epsilon k_0^2 - \beta^2, \tag{4.3}$$

where $k_\perp$ is the perpendicular wave number. Assuming cylindrical symmetry, we take $E = u(\boldsymbol{r}_\perp)e^{i\beta z} = R(r)e^{im\phi}e^{i\beta z}$, where r is the radial coordinate, ϕ is the azimuthal angle, and m is the azimuthal index, giving

$$\frac{d^2R}{dr^2} + \frac{1}{r}\frac{dR}{dr} + \left(k_\perp^2 - \frac{m^2}{r^2}\right)R = 0. \tag{4.4}$$

Assuming ϵ has a parabolic profile $= \epsilon_{r0} - \triangle\epsilon\frac{r^2}{r_0^2}$, Eq. 4.3 becomes the Laguerre equation

$$x\, d^2R/dx^2 + dR/dx + \left(-\frac{x}{4} + \frac{2p+m+1}{2} - \frac{m^2}{4x}\right)R = 0, \tag{4.5}$$

where $x = \frac{r^2}{r_0}\sqrt{\Delta\epsilon}$ and requiring $\beta^2 = \beta_{pm}^2 = \epsilon_{r0}k_0^2 - 2\frac{k_0}{r_0}\sqrt{\Delta\epsilon}(2p + m + 1)$, where p and m are non-negative integers and ϵ_{r0} is the dielectric function on axis. The solutions are $R_{pm}(x) = e^{-x/2}x^{m/2}L_p^m(x)$. For a parabolic plasma profile $\epsilon = 1 - \frac{N_e}{N_{cr}}$, $N_e = N_{e0} + \triangle N_e\left(\frac{r}{r_0}\right)^2$, we obtain the propagation wavenumber

$$\beta_{pm}^2 = k_0^2 - 4\pi r_e N_{e0} - (\tfrac{4}{w_{ch}^2})(2p + m + 1), \tag{4.6}$$

where $r_e = e^2/m_e c^2$ is the classical electron radius. The Laguerre-Gauss transverse mode solutions are

$$E_{pm} = a_{pm} e^{-\frac{r^2}{w_{ch}^2}} \left(\frac{2r^2}{w_{ch}^2}\right)^{\frac{m}{2}} L_p^m \left(\frac{2r^2}{w_{ch}^2}\right) e^{im\phi} e^{i\beta_{pm} z}, \tag{4.7}$$

where $w_{ch}^2 = r_0/\sqrt{\pi r_e \Delta N_e}$ and a_{pm} is a modal weighting coefficient.

For a waveguide of "core" radius r_m, a bound mode exists when $k_\perp^2(r < r_m) > 0$, $k_\perp^2(r > r_m) < 0$. In practice, for the waveguides generated here (see below), the plasma density goes to zero at some finite radius $r > r_m$ and $k_\perp^2 < 0$ is satisfied only within a finite radial region. Therefore, all the modes of these plasma waveguide are quasi-bound. As a simple model, consider a plasma density profile where $N_e = N_{e0} + \Delta N_e \left(\frac{r}{r_0}\right)^2$ for $r \leq r_m$ and $N_e(r) = N_e(r_m)$ for $r > r_m$. For bound modes, $k_\perp^2(r > r_m) < 0$. Substituting Eq. (4.6) into Eq. (4.3) gives an approximate cutoff condition for bound modes,

$$\Delta N_e \geq (2p + m + 1)^2/\pi r_e r_m^2. \tag{4.8}$$

Low order modes below this cutoff condition are still well approximated by the solution of the infinite parabolic profile. A numerical method was developed by Clark *et al*. to find the quasi-bound mode of finite plasma waveguide [108]. For a given $N_e(r)$, the method solves the transverse wave equation numerically over a range of β. Outside the plasma-neutral gas boundary, the solution of a particular β, $u(r)$, is matched with the no plasma Bessel beam solution $u_0(r)$ for the same $k_\perp$. For the $m = 0$ modes (where $u_0(r) = J_0(k_\perp r)$) , the solutions have maximum value on-axis, and a coupling efficiency is defined by

$$\eta(k_\perp) = \frac{|u(r=0,k_\perp)|^2|}{|u_0(r=0,k_\perp)|^2}. \tag{4.9}$$

Plotting $\eta(k_\perp)$ against β shows the quasi-resonances, as presented by the peaks, that resemble those of a cylindrical Fabry-Perot cavity. The FWHM of these peaks $\Delta\beta$ gives the propagation loss of these quasi-bound modes owing to leakage, where the electric field attenuates by $1/e$ after propagation of $L_{1/e} = 1/\Delta\beta$.

In order for a plasma waveguide to guide quasi-bound modes, there must be an electron density depression on axis, and there have been two main ways to generate such a density structure, laser driven shock expansion [66] and capillary discharges [109].

4.1.2 Laser-driven shock based plasma waveguide

Plasma waveguides based on hydrodynamic plasma expansion was first demonstrated by Durfee and Milchberg [66]. In this pioneering experiment, a 100 ps laser pulse, in the form of a J_0 Bessel beam, ionized high-Z gas (nitrogen, argon, xenon, etc) by multi-photon and avalanche ionization. During the avalanche phase and beyond, within the pulse temporal envelope, the plasma was heated resistively (inverse bremsstrahlung (IB)) to temperatures ~100 eV. The high temperature plasma column initiates a cylindrical shock wave expansion, driving a significant decrease of electron density on axis accompanied by rising density in the cylindrical shock wall, forming a guiding structure. Because the electron density drops to zero beyond the shock wall, and the refractive index approaches that of the surrounding gas at large radius, these waveguides are “leaky”, supporting only modes that are quasi-bound [108].

There have other variations on the hydrodynamic waveguide. In order to separate the processes of seed electron generation and avalanche ionization and heating,

Volfbeyn *et al.* used an intense femtosecond laser pulse to ionize hydrogen gas with optical field ionization before the 160-ps heater pulse [110]. Gaul *et al*. applied a pulsed electrical discharge to ionize helium gas, followed by a 100-ps laser pulse for IB heating [111]. In these schemes, efficient collisional ionization and IB heating requires high gas density, typically giving minimum waveguide on-axis densities of $N_{e0} > \sim 5 \times 10^{18} cm^{-3}$. However, lower density waveguides are desirable: for wakefield accelerators, low density plasmas minimize dephasing between the accelerated electron bunch and the driving field and result in higher accelerated bunch energy.

Cluster jets offers a route to generation of low density plasma waveguides. Clusters are assemblies of atoms bonded by the van der Waals force. A clustered gas jet can cause self-focusing and strong absorption of femtosecond laser pulses. Kumarappan *et al*. demonstrated that a clustered gas jet could be efficiently heated when end-pumped by a femtosecond laser pulse, which generated a hot plasma column and subsequent shock wave expansion [112]. With a clustered hydrogen gas target, plasma waveguides were generated with axial electron density less than $1 \times 10^{18} cm^{-3}$.

4.1.3 Capillary-based plasma waveguides

Capillary based plasma waveguides were first demonstrated by Ehrlich et al [109]. A plasma was generated by a pulsed ($\sim \mu s$) electrical discharge, ionizing the polypropylene capillary wall material, with further resistive heating of the plasma by the discharge. The quasi-steady state plasma supported by the long discharge is hotter in the centre and cool at the capillary walls, leading to lower electron density at the centre and higher density at the walls, the desired profile for an optical waveguide.

The capillary method was further developed by Spence *et al.* [113] by using hydrogen gas-filled ceramic or sapphire capillaries, with the plasma provided by the gas fill and not the capillary walls. A similar $\sim\mu s$ pulsed discharge ionized the hydrogen gas and heated the plasma, producing a similar plasma profile as above. Discharge simulations give a fundamental mode guided spot size of $w_M[\mu m] \approx 1.48 \times 10^5 \frac{\sqrt{R_0[\mu m]}}{(ZN_{i0}[cm^{-3}])^{1/4}}$ [114], where R_0 is the capillary radius, Z the degree of ionization and N_{i0} the initial ion density. Recently, a 20 cm long capillary discharge plasma waveguide, with the central electron density lowered by auxiliary laser heating, has been demonstrated, with guided laser-driven acceleration to ~8 GeV [15].

4.1.4 Plasma waveguides for laser wakefield acceleration

The use of plasma waveguides for laser wakefield acceleration (LWFA) has achieved guiding over tens of Rayleigh lengths and electron acceleration to multi-GeV energies [14,15]. To understand the effect of a guiding structure on electron acceleration, we recall the discussion of energy scaling in Chapter 1.4.4. Neglecting pump depletion, the electron energy gain in LWFA is limited by dephasing and is proportional to N_e^{-1} in 1D geometry. The energy gain is affected further by higher-dimensional effects in laser propagation. The laser group velocity v_g in a preformed plasma channel is related to the relativistic gamma factor $\gamma_g = \left(1 - v_g^2/c^2\right)^{-1/2} = \left(\frac{\omega_p^2}{\omega^2} + \frac{2c^2}{\omega^2 w_{ch}^2}\right)^{-\frac{1}{2}}$ [32], w_{ch} being the laser beam waist. Multi-GeV laser wakefield accelerators typically require axial electron densities $N_{e0} \sim 10^{17} cm^{-3}$. As a numerical example [40], consider a laser pulse with 40 J energy, peak power P=380 TW, $a_0 =$

$2, \lambda = 0.8\mu m, w_{ch} = 53\mu m$ and $\tau_{FWHM} \approx 69\ fs$, propagating in a plasma waveguide with $\lambda_p = 80\ \mu m$ ($N_{e0} = 2 \times 10^{17} cm^{-3}$ on axis), gives an electron energy gain $\triangle W = 10$ GeV over a dephasing length of $L_d = 40\ cm$.

Plasma waveguides with a requirement for such low axial electron densities poses a challenge due to the inefficiency of resistive heating at low density. The IB or laser-driven resistive heating rate in the absence of losses is $\frac{d\epsilon}{dt} = 2U_p \left(\frac{\omega^2 \nu_m}{\omega^2 + \nu_m^2}\right) \approx 2U_p \nu_m$, where U_p is the ponderomotive potential, and $\nu_m \ll \omega$ is the collision frequency of momentum transfer [73]. Reduced heating at low plasma densities drives weaker shock expansion under the same laser parameters, resulting in narrower and shallower waveguides whose lowest order quasi-bound modes can suffer significant leakage during propagation or may not even exist.

Although capillary-discharge waveguides have been limited to on-axis electron densities $> \sim 10^{18} \mathrm{cm}^{-3}$, auxiliary nanosecond laser heating has been used to further reduce the axial plasma density to as low as $3 \times 10^{17} \mathrm{cm}^{-3}$ [15], with the lowest order mode size $w_{ch} = 60\ \mu m$. Ultimately, the additional laser heating is limited by the decreased collision frequency due to the lower plasma density and higher plasma temperature.

In this chapter, we describe experiments demonstrating a method for generating plasma waveguides satisfying the following requirements: (i) Axial plasma density $N_{e0} \sim 10^{17} cm^{-3}$, (ii) high repetition rate operation, and (iii) sharp longitudinal cutoff to avoid ionization induced defocusing before an injected pulse reaches the waveguide

entrance [115]. These experiments are based on plasmas generated by optical field ionization (OFI).

We first review earlier work on OFI-based plasma waveguides which rely on OFI-based heating and hydrodynamic expansion. We then present results from our experiments, which were first based on OFI heating/hydrodynamic expansion and then transitioned to an approach using OFI to generate prompt electron density structures. As we will describe, this two-pulse method is successful in generating highly confining low density plasma waveguides appropriate for high energy LWFA.

4.2 Plasma channel from optical field ionization (OFI)

As discussed in the previous section, plasma heating is the limiting factor in formation of a low density plasma waveguide. In OFI, newly liberated electrons gain energy based on the ponderomotive potential of the laser pulse [116], independent of the electron density. Assuming a plane monochromatic laser field propagating along z, $\boldsymbol{E}(t) = E_0 e^{i\omega t}(\hat{\mathbf{x}} + \alpha i\hat{\mathbf{y}})$ and time t_f when an electron is liberated, the electron drift momentum is $\boldsymbol{p}_f = e\boldsymbol{A}(t_f)/c$. In the case of linear polarization ($\alpha = 0$), the ionization rate is the highest when the electric field is maximum i.e. $\frac{\partial \boldsymbol{E}}{\partial t} = -\frac{1}{c}\frac{\partial^2 \boldsymbol{A}}{\partial t^2} = \frac{\omega^2}{c}\boldsymbol{A} \approx 0$, so most electrons have no drift momentum. In the case of circular polarization ($\alpha = 1$), the field amplitude and therefore the ionization rate is constant within an optical cycle, and so liberated electrons have drift energy $E_k = |\boldsymbol{p}_f|^2/2m = e^2|\boldsymbol{A}(t_f)|^2/2mc^2 = \frac{e^2E_0^2}{2m\omega^2} = 2U_p$, where $U_p = \frac{e^2E_0^2}{4m\omega^2}$ is the ponderomotive potential, or the optical cycle average "quiver" energy.

OFI heating-based hydrodynamic expansion waveguides have been demonstrated with N_{e0} from $\sim 4 \times 10^{17}\mathrm{cm}^{-3}$ [117] to mid-$10^{18}\mathrm{cm}^{-3}$ [118–120]. In order to have a fully ionized plasma waveguide, these experiments use hydrogen gas. Lemos *et al*. first demonstrated OFI-based plasma waveguides using a Gaussian beam focused by a lens; here $N_{e0} \gtrsim 5 \times 10^{18} cm^{-3}$ [119]. Shalloo *et al*. used an Bessel beam generated by an axicon to create a 16-mm long plasma waveguide with $N_{e0} \gtrsim 4 \times 10^{17} cm^{-3}$ [117]. These developments are important for LWFA to ~10 GeV [16].

Hydrodynamic shock expansion following impulsive OFI-heating of the plasma column depends on the laser energy deposited per unit length. This is expressed by the Sedov-Taylor solution for cylindrical shock position vs. time as a function of energy deposited per unit length [121,122]. If the OFI electrons have a low temperature (when the laser is linearly polarized), or the plasma column quickly cools down due to thermal conduction or ballistic electron transport to surrounding neutral gas, the plasma expansion is weak and the electron density difference $\Delta N_e = N_e(r_m) - N_{e0}$ between the shock wall and the channel center is insufficient to support any quasi-bound modes. In one form of OFI-induced guide, the expanding plasma, while insufficiently heated to form a direct waveguiding structure, generates a peripheral neutral density bump from the expanding shockwave. If an intense injected laser pulse can (partially) ionize the neutral density bump, then an elevated electron density is generated near the periphery of the channel, forming a guiding structure. The injected pulse is effectively self-guided [123].

Without relying on hydrodynamic expansion, a hollow plasma channel can be generated directly by a high order Bessel beam, first demonstrated using avalanche

ionization [124] and later using OFI [125]. As the high order Bessel beam is hollow, it is unavoidable that the on-axis gas region is still neutral, preventing this structure's use as a plasma waveguide for high intensity laser pulses.

To solve this problem, we adopt a 2-beam approach. First, a J_0 Bessel beam ionizes neutral hydrogen gas by OFI and generates a fully ionized plasma column. Plasma expansion then significantly reduces the on-axis plasma density and increases the plasma and neutral gas density near the shock front. Second, a high order Bessel beam (in our case J_8 or J_{16}) ionizes the neutral gas near the shock front when launched at an appropriate delay and creates a large channel depth ΔN_e capable of confining quasi-bound modes.

4.3 Experimental setup

The proposed scheme requires generation of two co-propagating Bessel beam pulses with different orders and independently adjustable delays. To prevent damage to and nonlinear phase pickup in the transmissive optics in the 2-pulse generator, the generator must be placed in advance of the pulse compressor. Second, the two pulses should have the same polarization, because the pulse compressor has negligible transmission for S-polarization. Third, the energy ratio of the 2nd pulse to the 1st pulse should range from 1:1 to 4:1 in order to fully ionize hydrogen molecules with the 1st pulse.

There are various methods for generating a pair of collinear pulses. The most straightforward design is uses the Michelson or Mach-Zehnder design [126], but owing to the design, the highest ratio of output energy to input energy is 50%. A higher

efficiency approach is pulse splitting and recombining with a polarizing beamsplitter, but the output polarizations of the two pulses is orthogonal.

A more efficient design, used in our experiments, is the ring-cavity setup depicted inside the orange dashed circle in Figure 4.1. For a 30R:70T non-polarizing beamsplitter, the output energy fractions in the first two pulses are 0.3 and 0.49, for a generator efficiency of 79%.

This design does have drawbacks. First, the energy splitting ratio is not continuously adjustable and is fixed by the choice of non-polarizing beamsplitter. In the experiments described below, three different beamsplitters were used (reflectivity 0.2, 0.25 and 0.3), giving first pulse/second pulse energy fractions of 0.2 and 0.64 (84% generator efficiency), 0.25 and 0.56 (81% efficiency), and 0.3 and 0.49 (79% efficiency). In the specific geometry on our optical table, the 1st and 2nd pulse have a minimum separation of 0.7 ns. Because adequate hydrodynamic expansion after the first pulses takes ~1 ns, the geometry-limited minimum separation is not a concern.

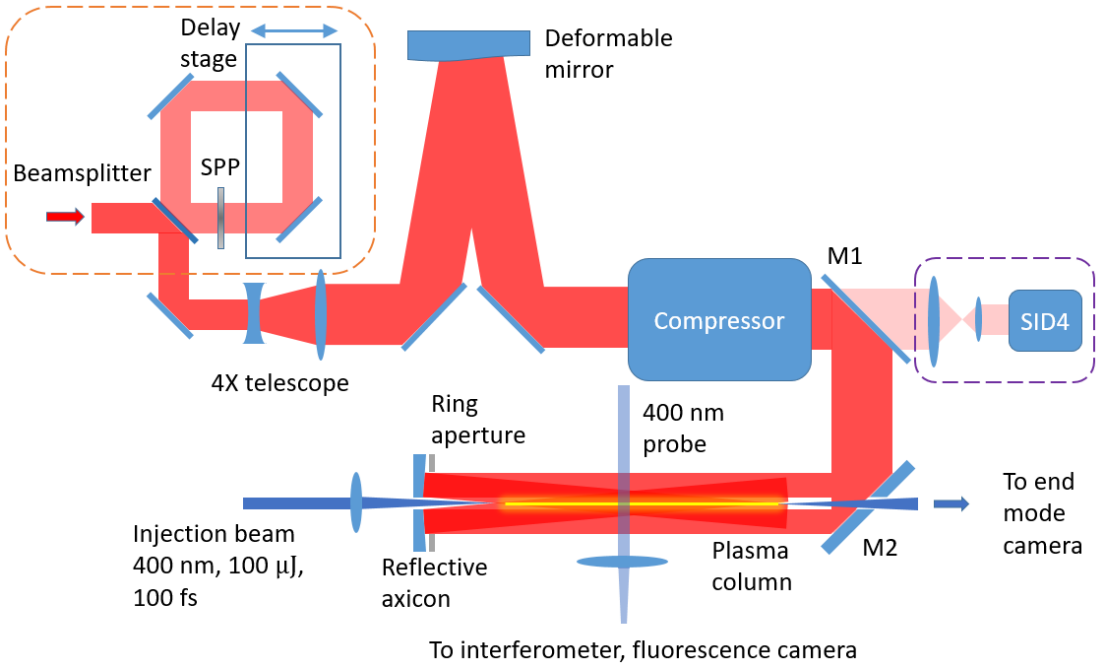

Figure 4.1 Experimental setup. Orange dashed rectangle: Double pulse generator. Purple dashed rectangle: adaptive optics loop. SPP-spiral phase plate.

The full experimental setup is shown in Figure 4.1. First, an amplified laser pulse is converted to a 2-pulse sequence by a non-polarizing plate beamsplitter in a ring optical configuration. The 1st pulse is directly reflected from the beamsplitter. The 2nd pulse, transmitted through the beamsplitter, passes through a spiral phase plate (SPP, to be described below) and an optical delay line before being collinearly recombined at the beamsplitter with the 1st beam. The following weaker pulses from the ring are ignored in this experiment. The two co-propagating pulses are then reflected by a deformable mirror to correct phase front aberrations with an adaptive optics loop (discussed in Chapter 3). After compression, the laser pulses are reflected from mirror M2 (containing a 12.5 mm diameter central hole) and directed to a reflective axicon (diameter 50.8mm with central 4 mm diameter hole) to form two high power Bessel beam pulses (J_0 plus either J_8 or J_{16}). In the following, we refer to axicons by their base angles. The two pulses ionize backfilled hydrogen gas and form a plasma waveguide. A synchronized low intensity femtosecond probe pulse ("injection beam" in Figure 4.1) is focused through the central hole of the axicon at the left end of the plasma as shown in Figure 1. The end mode is imaged through the drilled hole in M2 to measure the quasi-bound mode of the guiding structure. The transverse plasma profile was measured with interferometry using a λ=400 nm, 70 fs probe beam, using well-known phase retrieval techniques [127] followed by Abel inversion [128]. Plasma fluorescence is collected by a CMOS camera (Andor Zyla 5.5) to measure the length and uniformity of the guiding structure. In the following, all the fluorescence profiles were recorded with a band pass filter (400-750 nm).

4.4 Plasma dynamics from a J_0 Bessel beam

In this section we present the plasma evolution after ionization by a J_0 Bessel beam. For this purpose, we removed the beam splitter and SPP from the double pulse generator. The Bessel beam pulse energy was varied from 100 mJ to 300 mJ, and the plasma density profile was extracted from interferometry. The hydrogen backfill pressure was kept at 100 Torr. In order to adjust the plasma temperature, a quarter waveplate was inserted after compression to convert linear polarization to elliptical and circular polarization.

Examples of plasma evolution with two different reflective axicons is shown in Figure 4.2. In Figure 4.2(a) the plasma profile generated by a J_0 pulse produced with a 3° axicon shows hydrodynamic expansion with shock formation. A clear axial density minimum appears 0.5–1.5 ns after ionization. The plasma phase shift profile at a delay of 1.25 ns is shown in Figure 4.2(b). Similar data with a 1.5° axicon is shown in Figure 4.2 (a′)(b′).

There is no straightforward way to characterize the laser intensity profile, with plasma present, at the axial location of the transverse interferometry measurement. For input energy of 300 mJ, an estimate of the peak intensity was obtained by measuring the peak ionization yield in a 100 Torr argon backfilled chamber; interferometry revealed Ar completely ionized to Ar^{3+} for both Bessel beams. Assuming barrier-suppression-ionization [129] (which is reasonable according to [130]), this gives a minimum $I_{peak} \sim \frac{cE^4}{128\pi e^6 Z^2} \sim 1.2 \times 10^{15}\ \mathrm{W/cm^2}$, an intensity sufficient to fully ionize hydrogen molecules in both cases. The plasma density profiles in both cases are very

similar after a delay of 1 ns, likely because the laser energy deposition per unit length from ionization is similar.

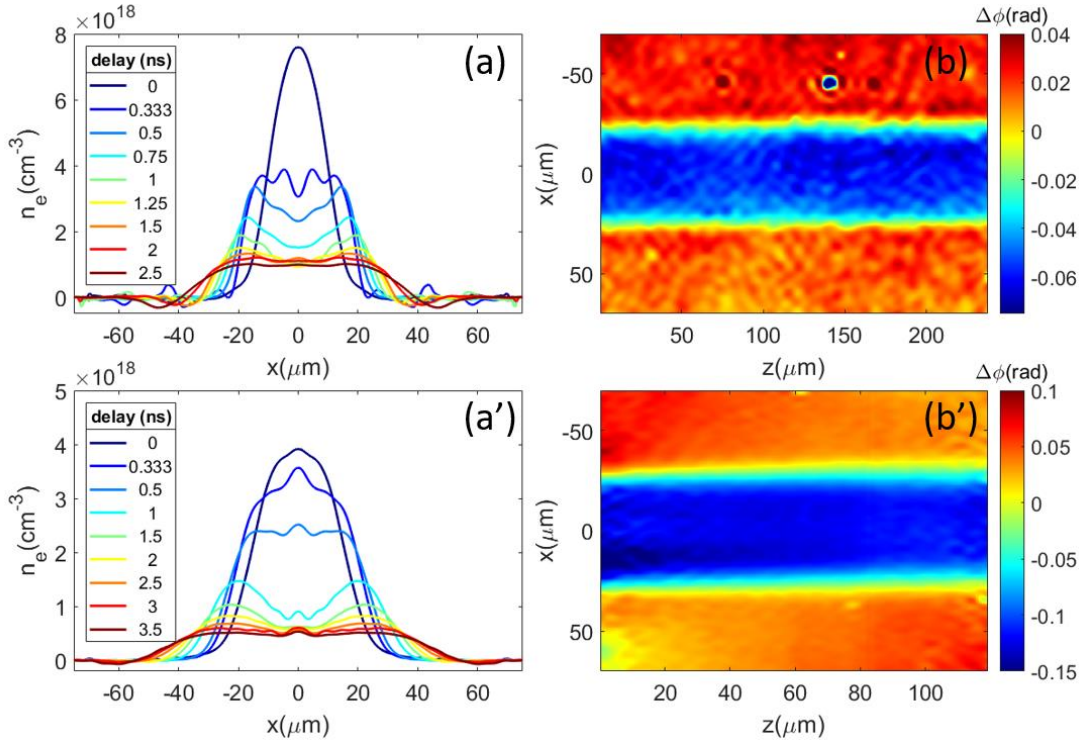

Figure 4.2 Plasma evolution after ionization by J_0 beam. In (a) and (b), the laser pulse energy was 300 mJ. (a)(a′) Electron density evolution with the 3° and 1.5° axicon. (b)(b′) Phase shift profile at 1.25 ns with the 3° and 1.5° axicon. The small peak near x=0 in (a) and (a') is from numerical artifacts in Abel inversion.

The plasma temperature can be measured by interferometric measurement of the shock position vs time, $R_s(t)$, enabling extraction of the laser energy deposited per unit length using the Sedov-Taylor expression for self-similar expansion of cylindrical shock wave [121,122], $R_s(t) = \xi_0 \left(\frac{E}{\rho}\right)^{1/4} t^{1/2}$. Used in the context of an impulsive laser-heated channel, E is the initial laser energy deposited per unit length driving the shock expansion, ρ is the mass density of the ambient medium, and ξ_0 is a dimensionless constant of order unity depending on the specific heat ratio . Fitting the

shock position data of Figure 4.2(a), we found $R_s(t) \propto t^{0.56\pm0.11}$, as shown in Figure 4.3(a) and energy deposition per unit length to be $16\mu J/cm$. The energy deposition per unit length for the data of Figure 4.2(a') is found to be 30% higher, consistent with the similarity in plasma expansion in Figure 4.2(a) and (a'). As the ambient hydrogen gas has negligible pressure compared to the plasma pressure, the shock velocity is determined by the ion acoustic wave speed $c_s \approx \left(\frac{\gamma \bar{Z} T_e}{m_i}\right)^{\frac{1}{2}}$, where $T_e \gg T_i$, the ion temperature. Shock velocity and the corresponding electron temperature are calculated from the fit in Figure 4.3(a) and shown in Figure 4.3(b). From Figure 4.3(a) and (b) it is seen that after ~1 ns the shock propagation stagnates as the electron temperature drops below 1eV.

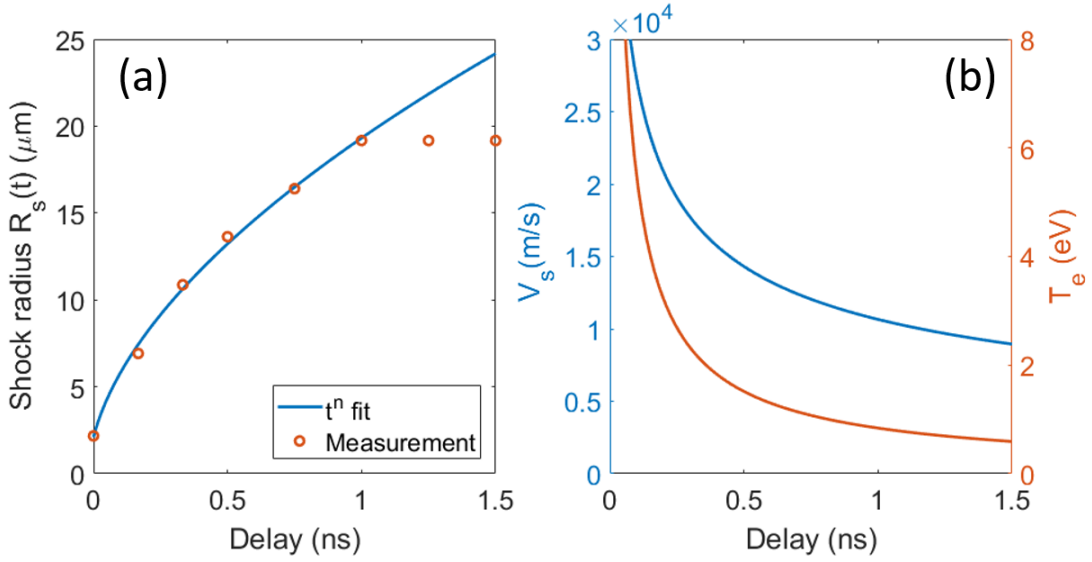

Figure 4.3 (a) Shock velocity (b) Electron temperature of plasma expansion in Figure 4.2(a)

In advance of injection/guiding experiments, we can check the for the quasi-bound mode structure of an interferometrically-measured waveguide using a numerical solver

based on the Helmholtz equation [108]. We apply this to the profile at 1.25 ns delay in Figure 4.2a.

Using a simulated profile which approximates the measured profile, we found a quasi-resonance at $k_{\parallel}/k_0 \approx 0.99975$, where k_0 is the wave number in vacuum, and $k_{\parallel}$ is the longitudinal wave number. as shown in Figure 4.4a. The plasma density profile at 1.25 ns and this quasi-bound mode are shown in Figure 4.4(b), assuming λ_0=800 nm. The mode $1/e$ radius is $w_0 = 12.7\ \mu m$. The width of the resonance peak in Figure 4.4a gives the propagation attenuation length (electric field decrease by $1/e$) of the mode,$L_{1/e} = \frac{1}{\Delta\kappa}$,where $\Delta\kappa = \Delta k_{\parallel,FWHM}/k_0$ [108]. In Figure 4.4(a), $L_{1/e} \approx 5.5$ mm$\approx 6Z_R$ for the mode, which is unsuitable for low density waveguiding over tens of centimeters, the goal for LWFA to ~1 GeV.

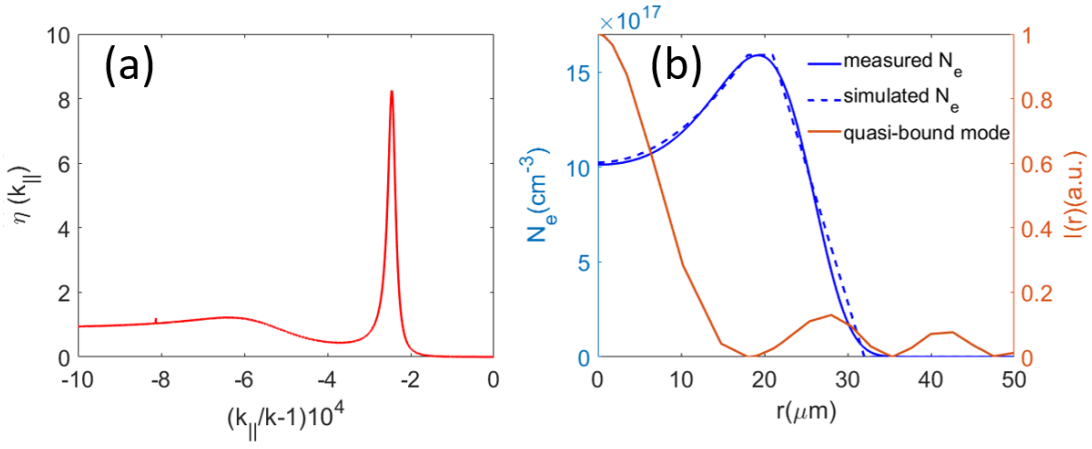

Figure 4.4 Determination of the quasi-bound mode and its attenuation length. (a) Plot showing resonant axial wavenumber $k_{\parallel}$. (b) Measured (solid blue), simulated (dashed blue) plasma density profiles, taken from the 1.25 ns data in Figure 4.2(a). The corresponding quasi-bound mode intensity profile is shown in red.

At delays longer than ~1.5 ns, shock expansion leads to compression of the ambient neutral gas just outside the shock region. Figure 4.5(a) shows the phase shift profile corresponding to the 2.5 ns delay for Figure 4.2(a). Figure 4.5(b) plots the z-averaged

phase profile and refractive index profile extracted by Abel inversion. The positive peripheral index bump from compressed neutral gas indicates that its local density is approximately twice the backfill gas density. According to [123], if an intense laser pulse is incident on such structure, the head of the laser pulse can ionize the neutral peaks and create a plasma waveguide for the rest of the pulse.

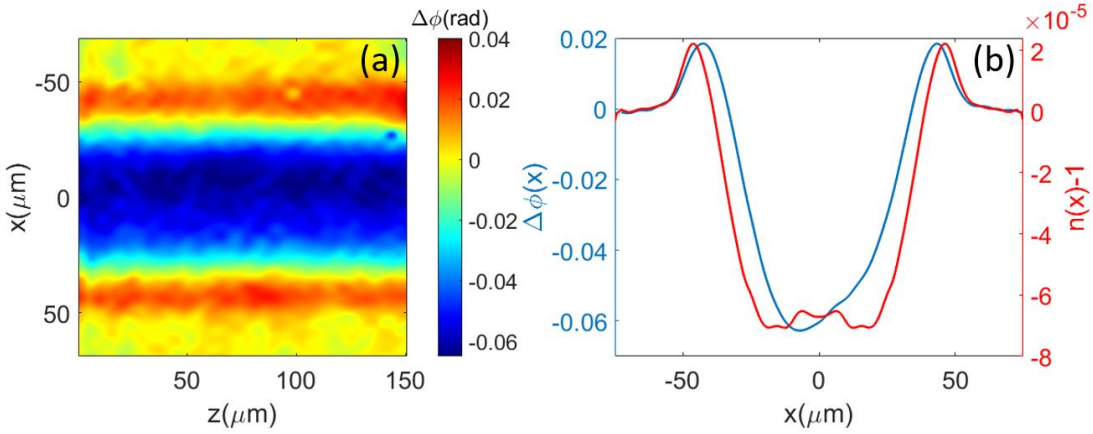

Figure 4.5 Compression of ambient neutral gas due to plasma expansion. (a) Phase shift profile (radians) corresponding to 2.5 ns delay for Figure 4.2(a). (b) Average phase shift along z of Figure 4.5(a) (black) and refractive index profile from Abel inversion (red).

We also compared the effect of heating between circular and linear polarization. The result showed that under the same conditions, circular polarization resulted in ~10% more plasma expansion (measured by shock positions) than linear polarization after ~1 ns. According to [131], the higher-temperature plasma from circular polarization experiences faster cooling due to faster plasma expansion work. Therefore, the difference between circular and linear polarization becomes smaller after ~1 ns.

In summary, we measured plasma waveguide formation from OFI heating by a J_0 Bessel beam in backfill hydrogen. The plasma quickly cools over ~ 1 ns by expansion

and thermal conduction, and the quasi-bound mode has significant attenuation, so such structure is not a good candidate for low density plasma waveguide. In the meantime, we found compressed neutral gas near the shock region, which may be used to generated low-loss guiding s tructure.

4.5 *Plasma dynamics from a high order Bessel beam*

As discussed earlier in this chapter, a higher order Bessel beam can be used to generate plasma profiles without relying on hydrodynamic expansion (and plasma heating). Such beams can be generated using a combination of an axicon and a spiral phase plate. In this section, we demonstrate tubular plasma generation using OFI with a femtosecond J_{16} Bessel beam pulse in 100 Torr hydrogen backfill. The hollow plasma structure is measured by interferometry, and its guiding properties are measured by injecting a low intensity probe pulse. As we are interested here in the maximum prompt ionization yield and not in heating, the Bessel beam is linearly polarized.

Figure 4.6(a) shows the imaged J_{16} focal profile produced by a 3° base angle axicon and an $l = 8$ spiral phase plate. Figure 4.6(b) shows the plasma phase shift for laser energy 200 mJ. Abel inversion shows a hollow plasma channel, as a function of delay, with negligible ionization on axis, as seen in Figure 4.6(c). The channel density profile evolution is shown in (c). It is seen that within 0.5 ns, the plasma ring expands radially both inwards and outwards, and the peak density drops by a factor of ~2. An energy scan of Bessel beam pulse energy in Figure 4.6 (d) for delay 0 ns shows high quality plasma tube generation over a wide range of energy.

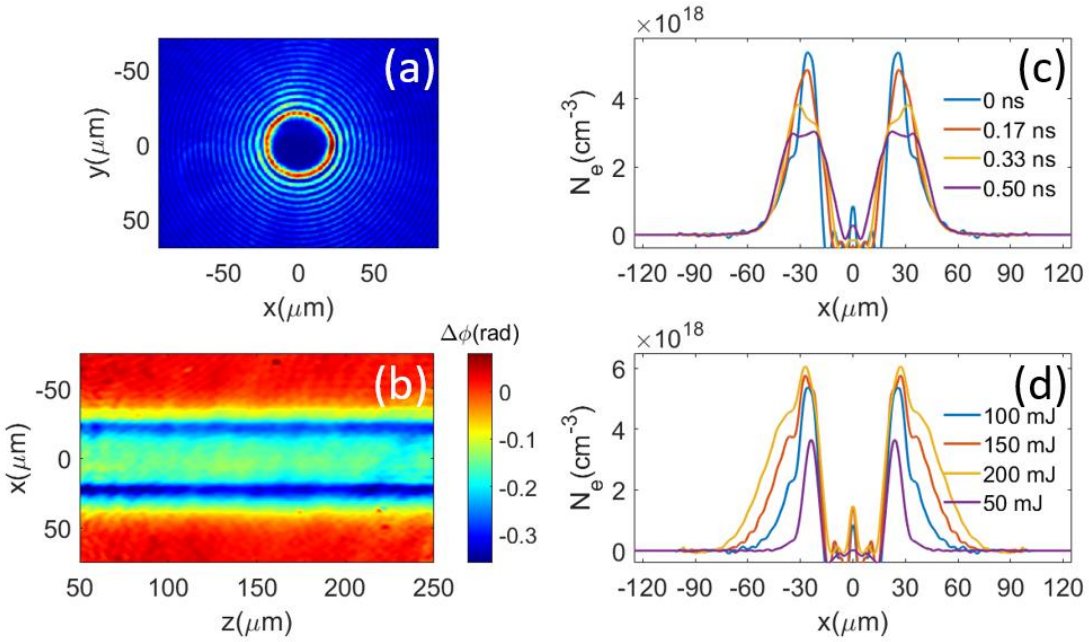

Figure 4.6 Interferometric measurements of hollow plasma channels generated by a J_{16} Bessel beam. (a) Sample J_{16} Bessel beam profile generated by a 3° base angle axicon. (b) Plasma phase shift from Bessel beam ionization for pulse energy 200 mJ. (c) Electron density evolution with 100 mJ laser energy. (d) Electron density profiles at delay 0 ns as a function of laser energy.

A low intensity probe pulse (400 nm, pulse energy ~100 μJ, pulse length~100 fs) was guided in ~40 mm long hollow plasma channels and the end mode was imaged with a CCD camera as shown in Figure 4.1. In Figure 4.7(a)-(f), guided end mode profiles averaged over 50 consecutive shots are shown as a function of Bessel beam energy, where the panels share the same colormap (except in (a), where the scale is 50× in order to show the unguided profile). The probe beam is injected within 100 ps delay with respect to the Bessel beam. The images show leakage on the top right, due to azimuthal asymmetry in the J_{16} focus, leading to an asymmetric plasma tube. As the Bessel beam energy increased, the plasma tube became less sensitive to this asymmetry and leakage was reduced. It is worth noting that the images in (a)-(f) were resolution-

limited due to limitation of the imaging aperture by the 6mm diameter hole in mirror M2.

Guiding stability is shown in Figure 4.7(g), where image slices of guided beams from 50 consecutive shots are plotted (for 150 mJ Bessel beam energy). The intensity variation was partly caused by fluctuations in the frequency doubled λ=400 nm pulse energy, which is sensitive to variations in the fundamental pulse energy. Other contributions to guided mode fluctuation are pointing fluctuation in the Bessel beam and injection beam, resulting in variation of coupling efficiency. Plasma fluorescence was used to measure the plasma waveguide length (Figure 4.7(h)) for the 3° base angle axicon to be ~40 mm. In Figure 4.7(h), the Bessel beam pulse propagates in the –z direction, and the modulation in fluorescence intensity is caused by axial beam modulations from edge diffraction from a Teflon ring aperture in front of the reflective axicon.

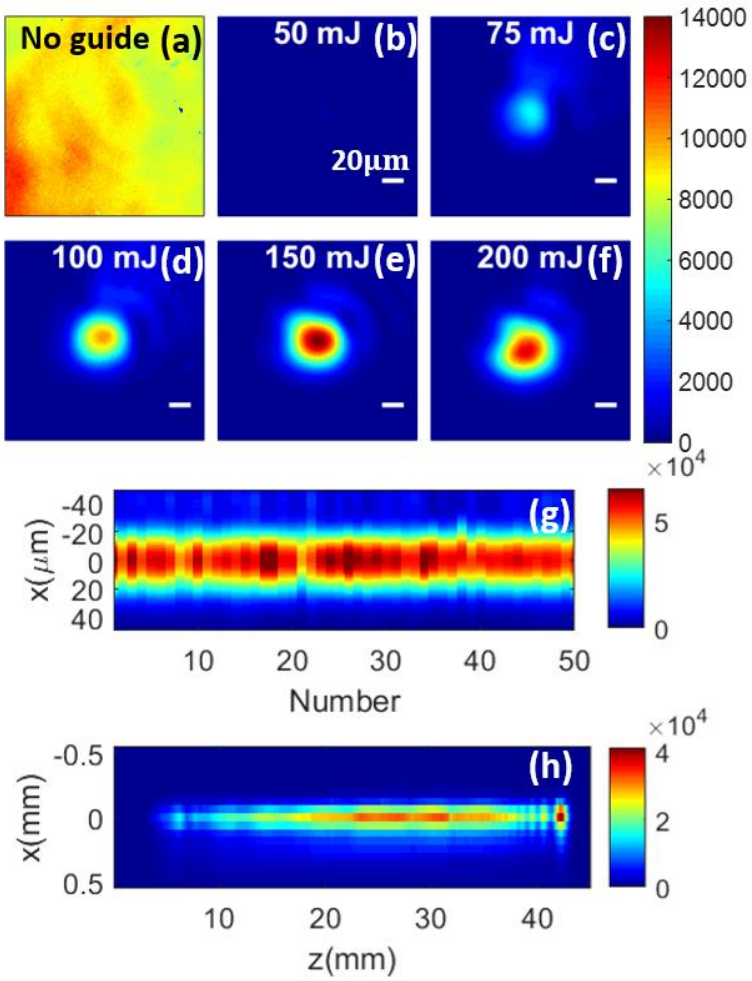

Figure 4.7 (a)-(f) Guided modes of a hollow plasma channel generated by a J_{16} Bessel beam pulse as a function of Bessel beam energy. The image of panel (a) is multiplied by 50. (a)-(f) share the same color map. (g) Slices of end mode images from 50 consecutive shots (150 mJ Bessel beam pulse energy). (h) axially resolved plasma fluorescence integrated from 400~750 nm (100 mJ Bessel beam energy), from which a plasma waveguide length of ~40 mm is measured.

The tubular plasma radius can be adjusted by either the axicon base angle or the spiral phase plate (SPP) order. Here we demonstrate the first approach using a 1.5° axicon with an $l = 16$ phase plate. An image of the Bessel beam focal profile is shown in Figure 4.8(a), where a hot spot section is seen near the top of the ring, which directly translates to the top-bottom asymmetry of plasma-induced probe phase shift in Figure 4.8(b). Figure 4.8(c) shows the electron density profile extracted from Abel inversion

of the z-averaged phase shift profile (Abel inversion removes the phase image asymmetry).

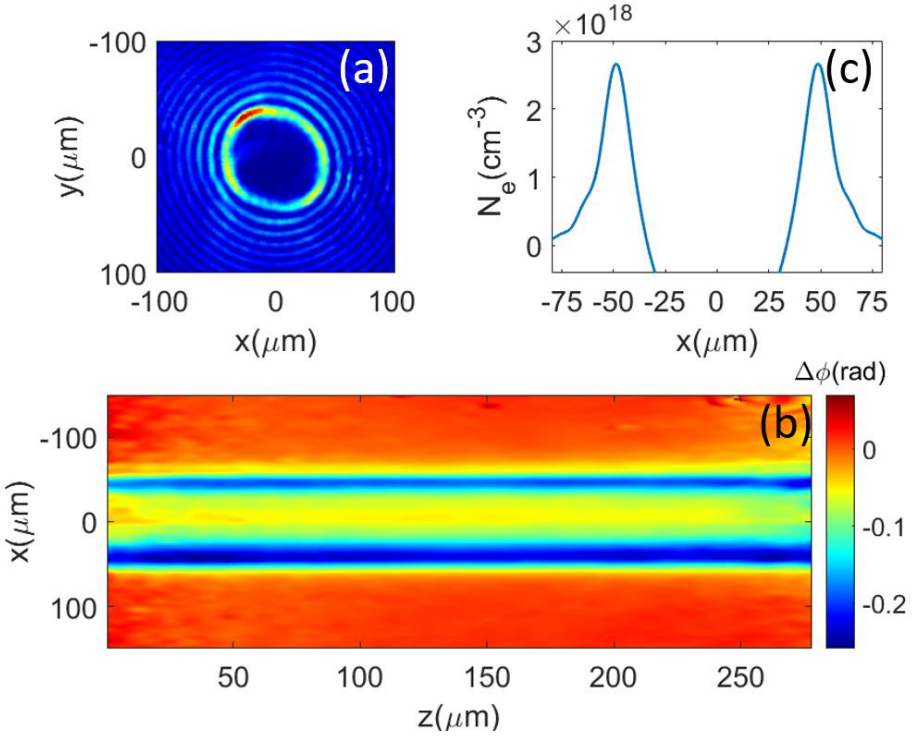

Figure 4.8 Characterization of hollow plasma channel generated by a J_{16} Bessel beam with a 1.5° axicon and a $l = 16$ spiral phase plate. (a) J_{16} Bessel focal profile (b) transverse probe phase shift profile; the color bar shows absolute phase shift (c) Electron density profile extracted from Abel inversion of the z-averaged phase profile.

Guided mode images as a function of Bessel beam energy are shown in Figure 4.9(a)-(d), where the color bar shows absolute energy (arbitrary units). The injection beam was the same as Figure 4.7. The possible cause for less transmission in (c) is coupling of the injection beam. In this measurement, the drilled mirror M2 (Figure 4.1) has a 12.5-mm diameter hole. This improves the resolution of the waveguide exit mode imaging system to ~10 μm. Guiding stability is shown in Figure 4.9(e), where the stability is mostly limited by laser pointing drift. The plasma channel length is measured by plasma fluorescence in Figure 4.9(f) to be $\gtrsim$12 cm. It is worth noting that

we later determined there had been vignette of the right half of the fluorescence image due to a geometric constraint on light collection.

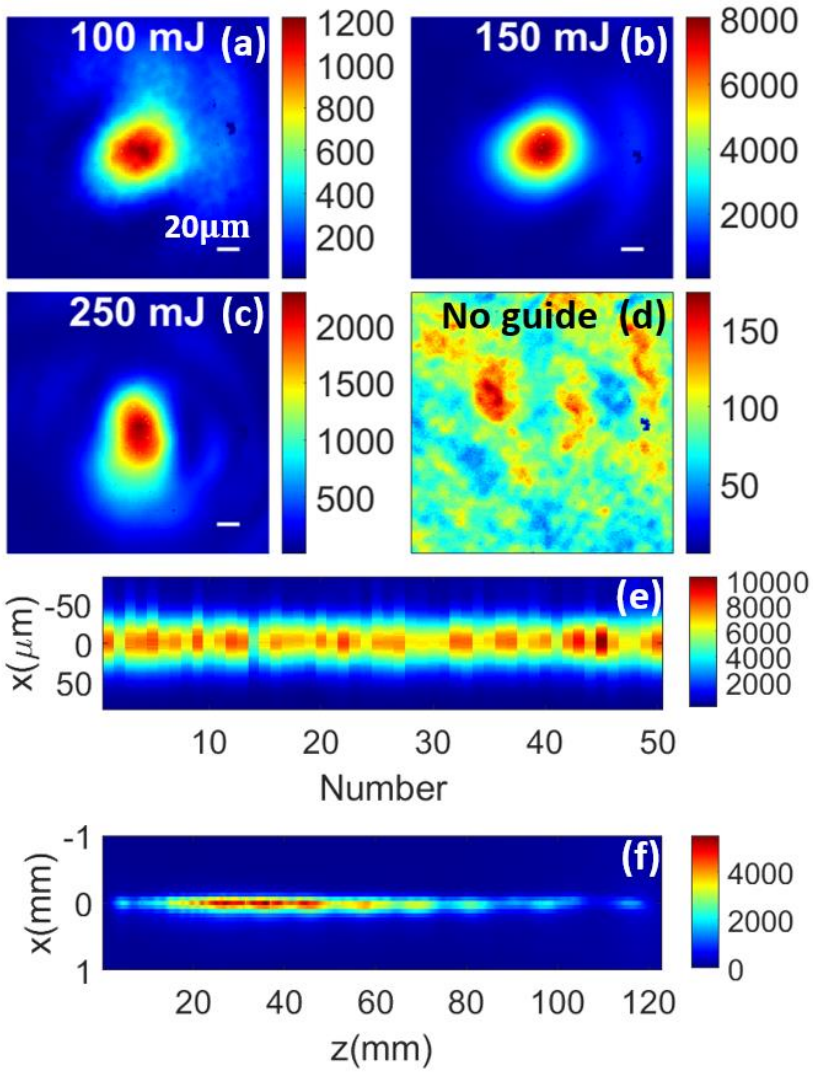

Figure 4.9 Guided mode of hollow plasma channel using a 1.5° reflective axicon and a $l = 8$ SPP. (a)-(d) End mode images as a function of Bessel beam energy. (e) Slices of end mode images for 50 consecutive shots from (150 mJ Bessel beam energy). (f) Plasma fluorescence image integrated from 400~750 nm with 100 mJ Bessel beam energy.

In summary, we demonstrated hollow plasma channel generation with high order Bessel beam. The guiding structure dimension is adjustable by either changing the axicon base angle, or the order of Bessel beam. The center of the guiding structure,

however, is still neutral hydrogen gas, so this is not useful for guiding high intensity laser pulses. In the next section, we combine the methods from the previous two sections to generate fully ionized plasma waveguide.

4.6 *Two-pulse method for plasma waveguide generation*

From the results of the previous two sections, a two-pulse method is developed to generate a low-attenuation plasma guiding structure. The two pulses are generated using the ring configuration of Figure 4.1 (orange dashed rectangle). The first pulse is a J_0 Bessel beam, which ionizes the axial neutral gas completely, driving plasma expansion as shown in Figure 4.2. The second pulse is a high order Bessel beam (here J_8 or J_{16}) launched at a delay after the first pulse when its highest intensity ring overlaps the expanding shock. A guiding structure is then formed which lasts ~0.5 ns due to expansion of the plasma ring. Here we demonstrate guiding of low intensity λ=400 nm laser pulses over 25 Rayleigh lengths in plasma waveguides generated using the two-pulse method.

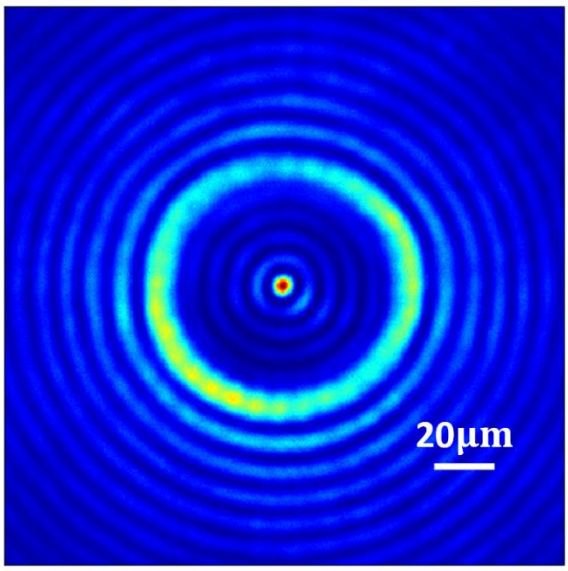

Figure 4.10 Alignment of J_0 and J_{16} beams generated by the ring configuration in Figure 4.1 and a 3° base angle axicon. The $l = 16$ SPP in one arm of the ring contributes to the J_{16} beam.

We used a 3° axicon with a PTFE ring aperture (OD= 35 mm, ID= 19 mm) that limited the plasma length to ~6 cm (measured by fluorescence). The function of the ring aperture is to provide sharp cutoff of plasma for better coupling of the injection beam. The two pulses were aligned such that the beam profiles overlap and the Bessel focus are concentric, as shown in Figure 4.10. The energy in the first (J_0) and second (J_{16}) pulse was 170 mJ and 152 mJ respectively. The two pulses were separated by 2.4 ns, which allowed the shock front to propagate to a radial position $\gtrsim 25\ \mu m$ (measured by interferometry), overlapping with the first ring position of the J_{16} beam. The first pulse is intense enough to fully ionize hydrogen molecules on axis, and the axial plasma density decreased by a factor of ~5 due to plasma expansion of 2.4 ns, measured by interferometry in the case of Figure 4.11(c) and 4.11(e).

A guiding structure was formed immediately after ionization by the J_{16} pulse. Guiding was observed over a 0.5 ns delay after the J_{16} pulse, consistent with the relaxation time of the tubular plasma (see Figure 4.6(c)). Guided beam mode profiles at the waveguide exit for λ=400nm injected pulses (delayed by <100 ps from the Bessel beam) as a function of hydrogen backfill pressure are shown in Figure 4.11(a)-(f). The guided beam peak intensity was affected by coupling, plasma density tapering at the entrance, and leakage. Gaussian fits to the quasi-bound modes of (a)-(e) give guided beam waist w_{ch} ranging from 31 μm to 18 μm, as the backfill pressure increased from 16 Torr to 100 Torr. For Figure 4.11(b) at 35 Torr backfill pressure, the axial plasma density is estimated to be $n_e = 4 \times 10^{17} cm^{-3}$ upon ionization from the 2nd (J_{16}) pulse.

In this case, for a measured guided beam waist $w_{ch} = 24\ \mu m$, the injected beam was guided over $13Z_R$. The backfill pressure can be further decreased, resulting in even lower axial plasma density, but finally the quasi-bound mode size, determined by the channel depth, exceeds the waveguide size, causing significant leakage, as shown in Figure 4.11(a). To demonstrate the stability of guiding, we plot the post-aligned central slices of 50 consecutive shots at 35 Torr backfill pressure in Figure 4.11(g).

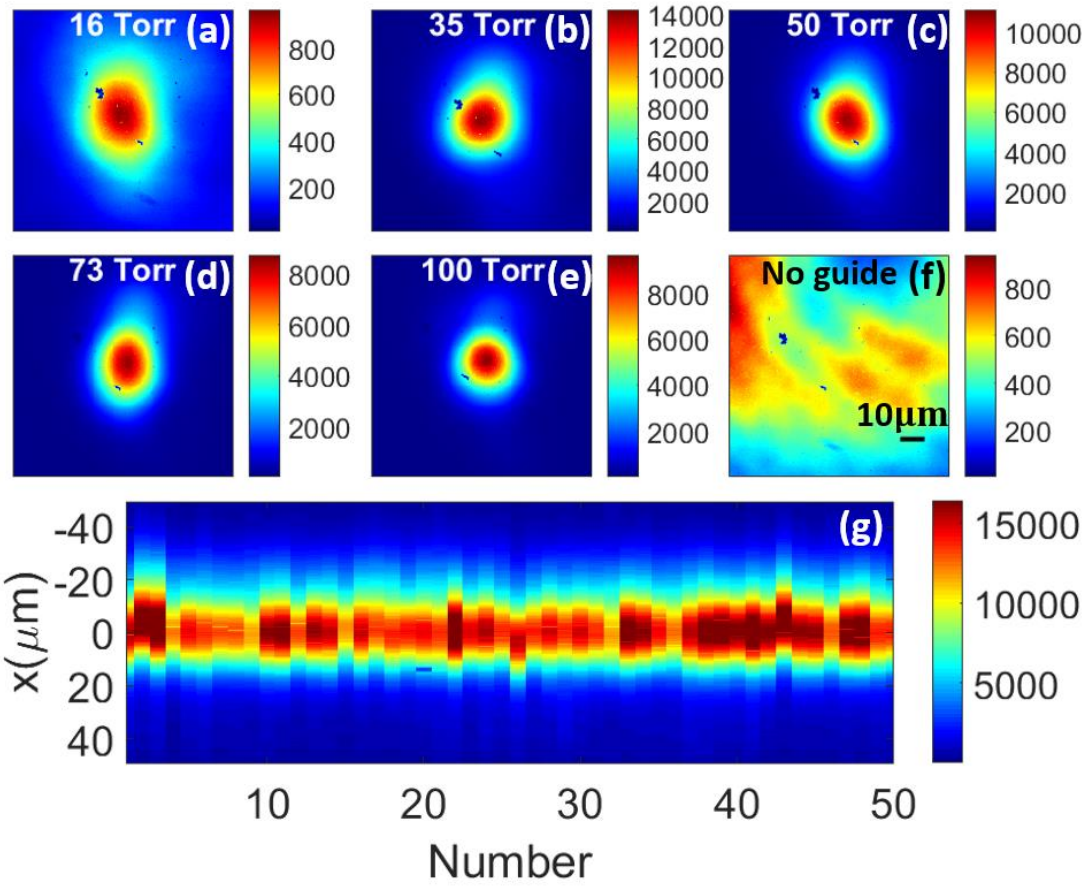

Figure 4.11 Guiding of λ=400 nm pulses in two-pulse method-generated plasma waveguides, using a 3° axicon. (a)-(f) Guided mode vs. hydrogen backfill pressure. (g) Central slices of guided output modes for 50 consecutive shots.

The plasma waveguide length can be extended using an axicon with a smaller base angle. As an example, with results shown in Figure 4.12, we used a 1.5° axicon, with

100 mJ and 235 mJ energy in the first (J_0) and second (J_8) pulse (energy measured before the ring aperture). The pulse separation was 2.4 ns. Here an $l = 8$ SPP was used in the ring configuration in Figure 4.1. The hydrogen backfill pressure was 50 Torr and the plasma length was estimated to be longer than 15 cm based on plasma fluorescence (see Figure 4.13, which is a photo of hydrogen plasma in the vacuum chamber). The guided beam of Figure 4.12(a) has $w_{ch} \approx 26\mu m$, indicating guiding over ~30 z_R. Here, the J_8 pulse ionized the neutral gas surrounding the expanding plasma, as seen in Figure 4.12(c). Extracting the electron density immediately after the J_8 pulse by Abel inversion, seen in Figure 4.12(d), shows a tubular plasma that is roughly aligned with the second ring ($r \sim 36\ \mu m$) of the J_8 focus. The absence of significant ionization from the first ring ($r \sim 23\ \mu m$) suggests that the expanded "core" of the plasma, generated by the J_0 pulse, was fully ionized. Figure 4.12(d) shows a 80-μm diameter plasma waveguide with axial plasma density $N_{e0} \approx 4 \times 10^{17} cm^{-3}$ and maximum plasma density $N_{e,max} \approx 4.5 \times 10^{18} cm^{-3}$ at the wall, extending over 15 cm.

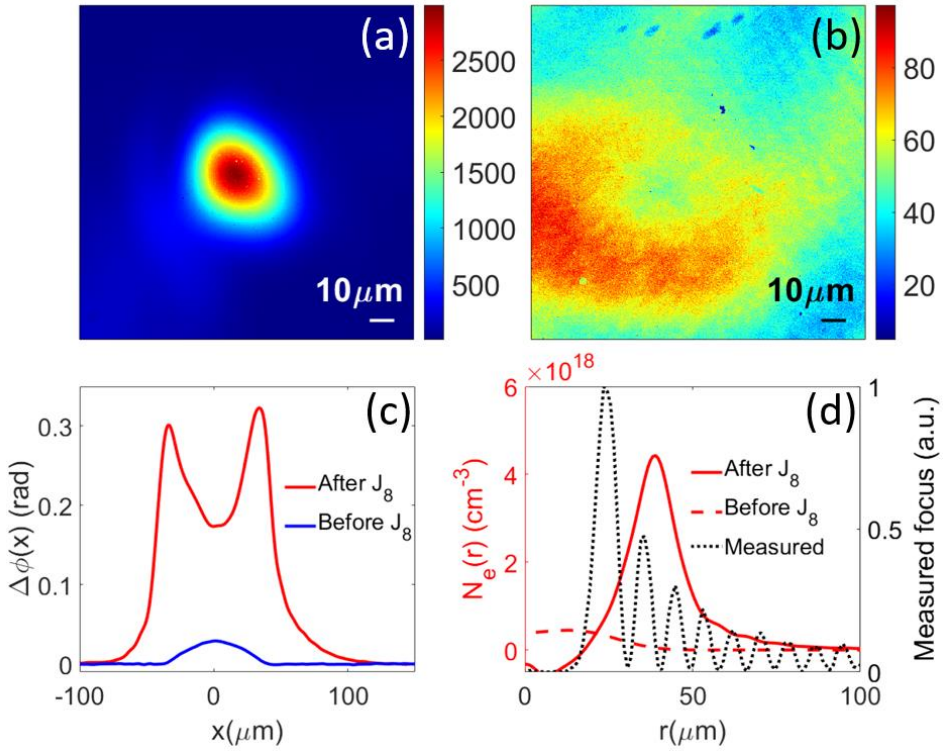

Figure 4.12 Guiding of λ=400 nm probe pulses in plasma waveguides generated using the two-pulse method, using a 1.5° axicon. (a) Guided mode with $w_{ch} \approx 26\mu m$ at plasma waveguide exit. (b) probe profile with no waveguide. (c) Plasma-induced interferometric probe phase shift immediately before (after) the J_8 pulse. The measurement was taken near the front end of the plasma (d) Extracted plasma density immediately before (after) the J_8 pulse. The black dashed line shows the measured intensity profile of the J_8 focus.

Plasma waveguides generated by the two-pulse method are tunable in multiple ways. First, the axial plasma density can be adjusted by gas pressure and delay time of the second pulse. The width of the guide is determined by the order of Bessel beam, the axicon base angle, and (weakly) on the delay between the two pulses. The formation of the high density tubular electron "cladding" is directly generated by optical field ionization rather than by a hydrodynamic shock wave. The high plasma density in the cladding enables low attenuation guiding, which is essential for applications such as LWFA that depend strongly on maintaining guided pulse energy and peak intensity

over many Rayleigh ranges. We note that modulation of plasma density is possible through engineered gas jet, or Bessel beam shaping, allowing extra control of group velocity of the guided beam for quasi phase matching [132–134].

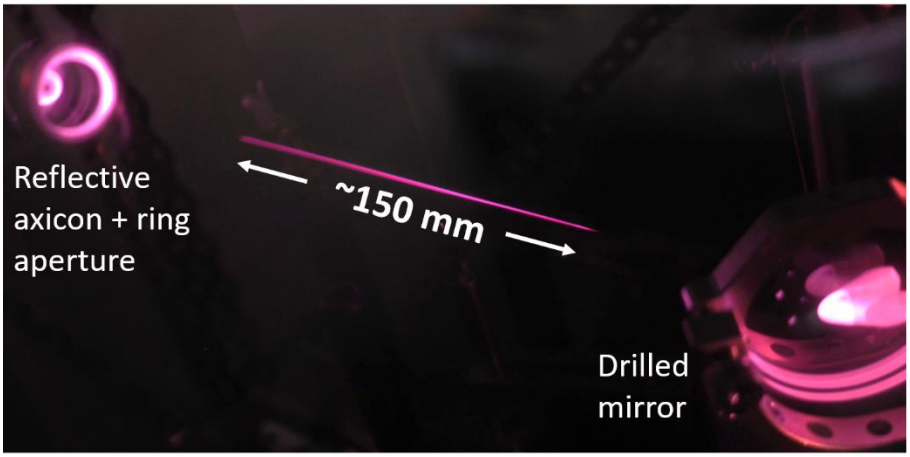

Figure 4.13 Plasma fluorescence with a 1.5° reflective axicon.

4.7 Discussion

Here we discuss some practical issues concerning the implementation of this method.

4.7.1 Propagation of high order Bessel beams through an existing plasma column

A question arises regarding the propagation of the second pulse. The existing plasma column from the J_0 pulse may affect the formation of a high order Bessel beam. In a simplified treatment, we assume a high order Bessel beam focusing on a uniform plasma column of radius $a = 30\mu m$ and peak density as $1 \times 10^{18} cm^{-3}$. The parameters are chosen to approximate typical experimental conditions. Following the treatment of Marcuse [135], inside the plasma column ($r < a$),

$$E_z = \frac{iB\sigma}{2\beta}[J_{m+1}(\sigma r)e^{i(m+1)\theta} - J_{m-1}(\sigma r)e^{i(m-1)\theta}], \quad (4.8)$$

$$H_z = \frac{B\sigma}{2\omega\mu}[J_{m+1}(\sigma r)e^{i(m+1)\theta} + J_{m-1}(\sigma r)e^{i(m-1)\theta}], \tag{4.9}$$

$$E_x = BJ_m(\sigma r)e^{im\theta}, \tag{4.10}$$

$$\sigma^2 = \epsilon k_0^2 - \beta^2, \tag{4.11}$$

where the incident beam is linearly polarized along x, B is a constant, β is the longitudinal wavenumber. Outside the plasma column ($r > a$)

$$E_z = \frac{iC\rho}{2\beta}\left\{\left[H_{m+1}^{(1)}(\rho r) + FH_{m+1}^{(2)}(\rho r)\right]e^{i(m+1)\theta} - \left[H_{m-1}^{(1)}(\rho r) + FH_{m-1}^{(2)}(\rho r)\right]e^{i(m-1)\theta}\right\}, \tag{4.12}$$

$$H_z = \frac{C\rho}{2\omega\mu}\left\{\left[H_{m+1}^{(1)}(\rho r) + FH_{m+1}^{(2)}(\rho r)\right]e^{i(m+1)\theta} + \left[H_{m-1}^{(1)}(\rho r) + FH_{m-1}^{(2)}(\rho r)\right]e^{i(m-1)\theta}\right\}, \tag{4.13}$$

$$E_x = C\left[H_{m+1}^{(1)}(\rho r) + FH_{m+1}^{(2)}(\rho r)\right]e^{im\theta}, \tag{4.14}$$

$$\rho^2 = \epsilon k_0^2 - \beta^2, \tag{4.15}$$

where C is a constant and the H are Hankel functions. Applying the boundary conditions (continuity of E_z and H_z) leads to

$$C = \frac{ia\pi}{4}\left[\sigma J_{m+1}(\sigma a)H_m^{(2)}(\rho a) - \rho J_m(\sigma a)H_{m+1}^{(2)}(\rho a)\right]B, \tag{4.16}$$

$$F = -\frac{\sigma J_{m+1}(\sigma a)H_m^{(1)}(\rho a) - \rho J_m(\sigma a)H_{m+1}^{(1)}(\rho a)}{\sigma J_{m+1}(\sigma a)H_m^{(2)}(\rho a) - \rho J_m(\sigma a)H_{m+1}^{(2)}(\rho a)}. \tag{4.17}$$

In Figure 4.14 we plot the numerical results for $m = 0$, 8 and 16, alongside the Bessel beams J_0, J_8 and J_{16}. It is seen that the amplitude of the solution in the presence of the plasma cylinder is similar to the plasma-free Bessel beam but the peaks shift radially. The effect of the plasma column becomes negligible for sufficiently high order Bessel beams.

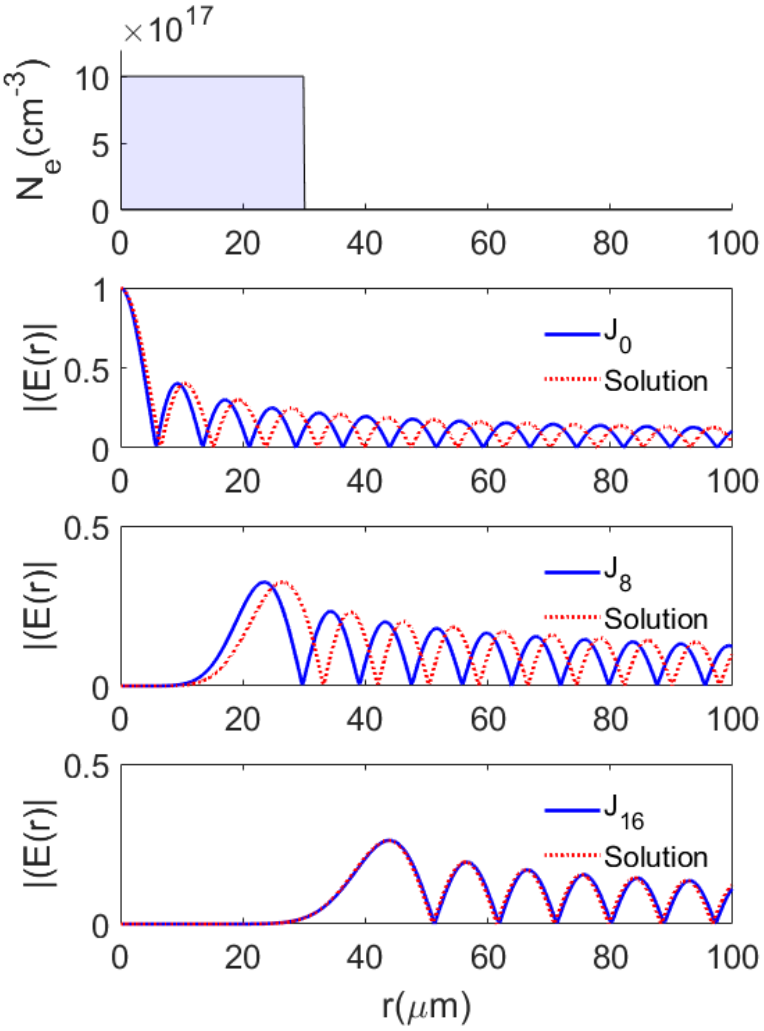

Figure 4.14 Effect of existing plasma column on the formation of Bessel beam.

4.7.2 Attenuation of plasma waveguides generated using the two-pulse method

A high ionization fraction from the second, high order, Bessel beam is important for a sufficiently confining waveguide cladding to ensure low-loss propagation of a quasi-bound mode over a long propagation distance. Here we take the 35 torr case of Figure 4.11(b) as an example. For 100% ionization by the J_{16} beam, the waveguide attenuation length $L_{1/e}$ can reach ~75 cm, depending on details of the cladding (calculated using $\eta(k_{\parallel})$ as in Figure 4.4). In Figure 4.15, two guiding structures are plotted with the same peak cladding density, but with 10- and 20-μm linear decay

ramps (solid and dashed blue lines) to model the radial fall off in electron density outside the cladding, as seen in Figure 4.6(d). While the quasi-bound modes of the two profiles are indistinguishable, with guided beam waist $w_{ch} \approx 15\ \mu m$, the attenuation lengths are quite different: 25 cm vs. 75 cm depending on the cladding density radial fall off.

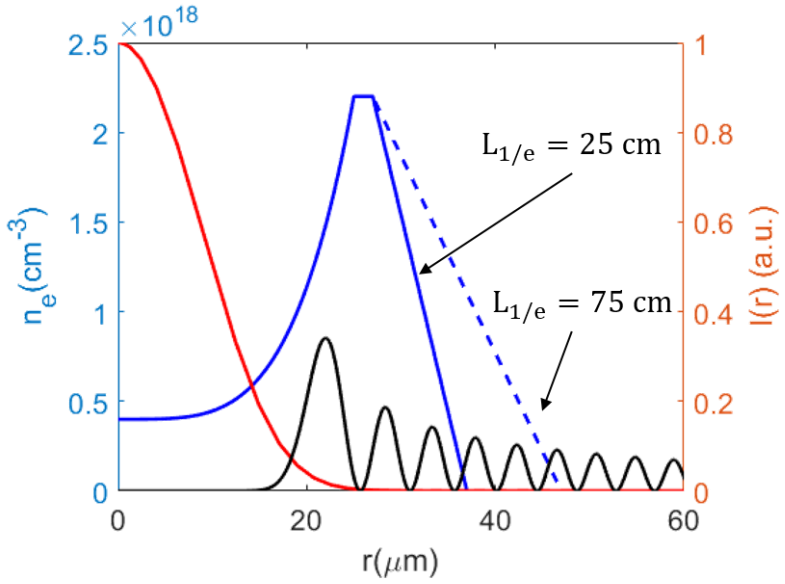

Figure 4.15 Estimate of the attenuation length of the plasma waveguide calculated using $\eta(k_{\parallel})$ as in Figure 4.4. The plasma profile is set to resemble the case for Figure 4.11(b). The solid (dashed) blue lines shows the plasma density profile with 10- (20-) μm linear decay ramp, with 25 (75) cm attenuation length for its lowest order quasi-bound mode (red solid curve). For reference, the black curve shows the intensity profile of a J_{16} Bessel beam focused by a 3° reflective axicon.

4.7.3 Laser energy requirements for plasma waveguide generation

The energy required in the second, high order, Bessel beam to fully ionize hydrogen gas is calculated using an empirically modified ADK model [129,136,137] to better fit barrier-suppression ionization. The modified ionization rate W_{TBI} for a linearly polarized electric field is expressed in atomic units as

$$W_{TBI}(F) = W_{TI}(F)e^{-\alpha(Z^2/I_p)(F/F_0)}. \quad (4.18)$$

Here, $W_{TI}(F)$ is the ADK rates, expressed as [138]

$$W_{TI}(F) = \left(\frac{3F}{\pi F_0}\right)^{\frac{1}{2}} |C_{nl}|^2 \left(\frac{2F_0}{F}\right)^{2n-|m|-1} f(l,m)\exp(-\frac{2F_0}{3F}), \tag{4.19}$$

where $F_0 = \left(2I_p\right)^{3/2}, n = Z\left(2I_p\right)^{-1/2}$, I_p is the ionization energy, Z is the charge of the resulting ion and F is the external electric field. For circular polarization, the factor $\left(\frac{3F}{\pi F_0}\right)^{\frac{1}{2}}$ is removed. $f(l,m)$ and C_{nl} are expressed as

$$f(l,m) = \frac{(2l+1)(l+|m|)!}{2^{|m|}(|m|)!(l-|m|)!}, \tag{4.20}$$

$$|C_{nl}|^2 = \frac{2^{2n}}{n(n+l)!(n-l-1)!}. \tag{4.21}$$

For arbitrary atoms the principle quantum number is replaced by the effective principle quantum number $n^* = Z\left(2I_p\right)^{-1/2}$. The exponential parameter α is obtained by fitting the expression to a numerical simulation using the time dependent Schrodinger equation (TDSE) in the single active electron (SAE) approximation [137]. For hydrogen, $\alpha = 6$. The ionization yield is calculated as $Y = 1 - \exp(-\int_{-\infty}^{\infty} W[|F(t)|]\, dt$. To calculate Y for the hydrogen molecule by a laser pulse, we assume the hydrogen molecules and atoms are in the ground electronic state. We apply the dissociation energy ($H_2 \rightarrow H_2^+ + e^-$) of the hydrogen molecule [139,140] to the hydrogen atom with ionization energy $I_p = 15.4\ eV$ [120]. In Figure 4.16, for a 50 fs FWHM Gaussian plus, we plot Y vs. peak laser intensity. For linear polarization (LP), ionization saturates at $I_{sat} \approx 4.5 \times 10^{14} W/cm^2$ (95% ionization yield).

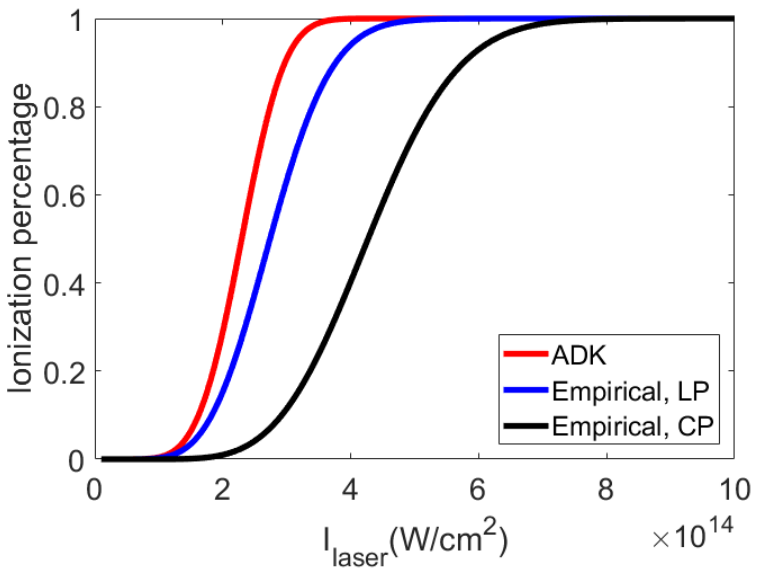

Figure 4.16 Ionization percentage of hydrogen atoms by a 50-fs laser pulses.

We further examine the laser parameters require to generate an elongated Bessel beam focus at the saturation intensity. We assume the Bessel beam is generated by a 3° reflective axicon (and an $l = 16$ SPP), illuminated by a Gaussian beam with $w_0 = 2.5\ cm, \tau_{FWHM} = 50\ fs,$ and $E = 150\ mJ$. The intensity of the Bessel beam along z can be derived from [72,73,141,142], or from chapter 3 as $I(r,z) = I(\rho_\beta)\frac{2\pi k \rho_\beta \sin\beta}{\cos^2\beta} J_m^2(kr\sin\beta)$.

For small β, $\rho_\beta \approx 2z\tan\beta$. The peak intensity of the J_{16} focus vs. z is plotted in Figure 4.17. Saturation intensity is achieved over ~15 cm on the focal line. Therefore, the laser energy required per centimeter is on the order of 10 mJ as an estimate of upper bound.

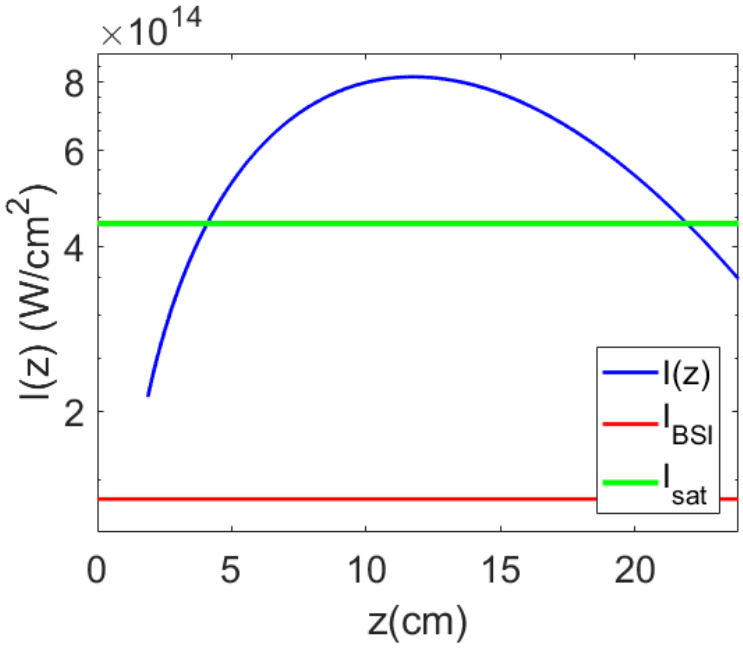

Figure 4.17 Peak intensity distribution of J_{16} focus. Blue line: calculated intensity in the first ring of Bessel beam. Green line: Saturation intensity $I_{sat} = 4.5 \times 10^{14} W/cm^2$. Red line: critical intensity of barrier suppression ionization of hydrogen atoms

4.8 Conclusion

In summary, we presented a two-pulse method to generate long (>10 cm) plasma waveguide with low axial plasma density ($n_e \lesssim 4 \times 10^{17} cm^{-3}$). The guiding structure is widely tunable and low-loss, making it a prospective component for research areas requiring extended laser matter interaction, such as laser particle acceleration [14,15,125], frequency conversion [143].

Chapter 5 Summary and future work

5.1 Summary

The research in this dissertation covers physics relevant to laser wakefield acceleration efforts on two widely different experimental scales set by the peak laser power employed: (1) For terawatt and sub-terawatt lasers applied to compact, high repetition rate LFWA to tens of MeV, we studied the coherent laser-assisted injection "flash" radiation characteristic of near-critical density gas jet interactions. (2) In experiments aimed for future application at larger scale petawatt laser facilities, we developed a new method for generation of low density plasma waveguides that can be as long as tens of centimeters, enabling acceleration to multi-GeV energies.

Chapter 2 described our experiments studying the flash radiation from electron injection into wakefields in near-critical density gas jets. We characterized the properties of this ultrafast pulsed radiation, demonstrating its spectral coherence using spectral interferometry and determining its pulse length using single-shot supercontinuum spectral interferometry (SSSI). The measured spectral modulation of the radiation is evidence of electron injection into multiple buckets, or beam loading. The flash radiation polarization was dominantly along the wake-driving laser polarization, and its angular distribution was dominantly in the forward direction. These features point to the electron injection as laser-assisted, a scenario verified by particle-in-cell simulations.

In chapter 3, in preparatory work for our plasma waveguide generation and guiding experiments, we fabricated spiral phase plates and generated high order Bessel beams with peak intensity in excess of $10^{15}\mathrm{W/cm^2}$ using reflective axicons.

Wavefront aberration from various described sources was responsible for imperfect Bessel focal profiles; these aberrations were measured with phase retrieval for the first time. This information was used to apply phase front corrections, using a deformable mirror, to improve the Bessel beam focal profile quality.

In chapter 4, we applied phase front-corrected and optimized (high order) Bessel beams to generate hydrogen plasma waveguides using femtosecond optical field ionization. The plasma evolution was measured via transverse interferometry. It was shown that plasma heating by field ionization was insufficient to form, via hydrodynamic expansion, a low-loss guiding structure from single J_0 pulses. To solve this problem, we developed and demonstrated a two-pulse technique, combining a J_0 pulse with a delayed J_8 or J_{16} pulse, to generate a low axial density plasma waveguide with a surrounding high electron density tubular "cladding". This new method minimizes the role that hydrodynamic expansion plays in waveguide generation. Low intensity λ=400 nm probe pulses were guided over 30 Rayleigh lengths in these waveguides in a relatively small mode. These low plasma density yet highly confining guiding structures—made possible by the field ionization induced by the high order Bessel beam--show great promise for application to multi-GeV-scale acceleration with petawatt scale lasers..

5.2 Future work

So far, only low intensity λ=400 nm probe pulses were guided in in our two-pulse generated plasma waveguides. As the guide is fully ionized, we expect that much higher intensity pulses will be successfully guided. For this purpose, a sharp plasma-vacuum boundary is necessary to avoid ionization of ambient gas before the high

intensity laser enters the plasma waveguide. Such a boundary can be realized with a gas jet, as detailed in the Appendix, or a gas cell.

Work is underway to incorporate a 10-cm long supersonic gas jet into high intensity laser guiding experiments. As the Bessel beam focus is affected by such elongated an obstruction, the laser wavefront must be engineered using methods discussed in Chapter 3 to mitigate this issue.

The low density plasma waveguide provides a possible candidate as hollow plasma channel, if generated from suitable gas density. For application to a positron acceleration experiment, Gessner *et al.* [125] generated a hollow plasma in lithium vapour using a high order Bessel beam, but the central part of the channel remained neutral gas. In comparison, our technique generates a plasma channel with lower axial density by plasma expansion (<20% of the original gas density), providing a stronger wakefield and leading to an even more promising candidate for electron beam-driven acceleration of positrons.

Appendices

A.1 Elongated gas jet for low density plasma waveguide

High intensity laser guiding requires a sharp vacuum-plasma boundary to allow pulse injection into the plasma waveguide without ionization-induced refraction occurring in ambient gas in advance of the waveguide. This can be achieved by generating the plasma waveguide in a gas jet. Such elongated gas jets have been demonstrated over a ~1 cm scale [72,144,145] both in unclustered and clustered gases [146–148]. Here, we present results for 10-cm long supersonic gas jet for generation of low density plasma waveguides described in Chapter 4. The jet gas flow is designed to be supersonic so that gas-vacuum boundaries are sharp and so that the gas density at a fixed distance above the orifice is higher than it would be with sonic flow.

The gas jet design consists of a gas reservoir and a converging-diverging nozzle fed by two solenoid valves, as seen in Figure A.1 The nozzle shape was designed using the method of characteristics [149] with a 50 μm throat and Mach number $M = 4$. The whole block was assembled by two aluminum pieces by CNC machining. The millisecond rise time solenoid valves ensured a proper gas flow rate for high output gas density. All the tests of the gas jet were completed in a vacuum chamber.

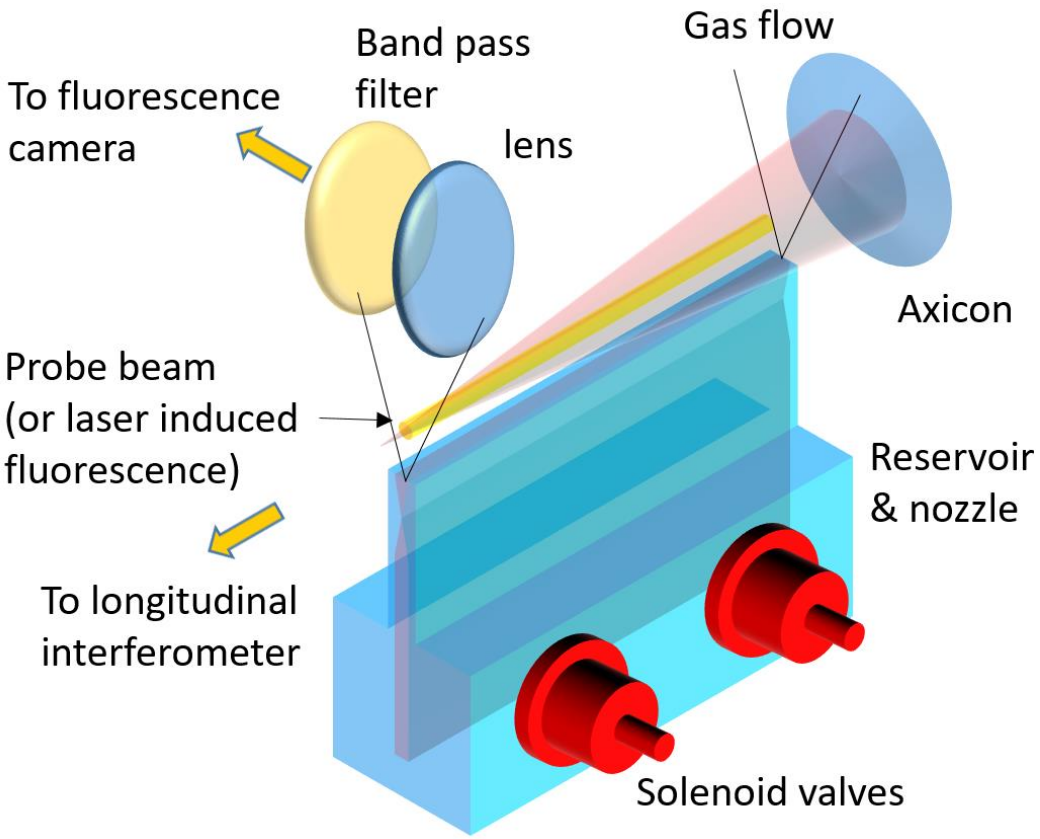

Figure A.1 Diagram of 10-cm elongated supersonic gas jet, longitudinal interferometric probe beam, and transverse collection of laser induced fluorescence.

The gas jet density profile was measured using two methods. In the first method, a collimated interferometric probe beam propagated through the gas plume parallel to the elongated nozzle orifice. The integrated phase was measured by shearing interferometry and was corrected with a linear beam propagation simulation to correct for gas profile-induced refraction. This measurement yields the averaged gas density along the nozzle.

A sample axially averaged gas density profile extracted from longitudinal interferometry probe is shown in Figure A.2. In this measurement, we used nitrogen gas with 200-1000 psi solenoid valve backing pressure. The trigger and shutter time

($\sim 100\mu s$) of the camera was adjusted such that the recorded CW probe beam (λ=532 nm) arrived after the gas flow reached steady state. Two gas plume profiles are seen in the phase shift image due to limited shear between the two arms of the interferometer (Figure(A.2(a)). From interferometry, the phase shift image of the two arms were sheared and subtracted, resulting in two "plumes", one positive and the other negative. To assist the phase extraction, we fit each row in Figure A.2(a) with double super Gaussian functions in every row, with the result shown in Figure A.2(b). The integrated phase shift, $\Delta\phi$, then gives the axially averaged nitrogen gas density profile $N_g = \frac{\Delta\phi}{kl}\frac{N_g^{NTP}}{n_g^{NTP}}\,\eta$, where l is the gas jet length, N_g^{NTP}, n_g^{NTP} are the nitrogen gas density and refractive index at standard temperature and pressure, and η is a refraction factor (see below), with the result plotted in Figure A.2(c). Beam propagation simulations [150] were performed to compare the phase of the probe beam after propagation to the 1D phase pickup $\Delta\phi =$. It was found that the actual phase shift is lower than the 1D result by 20%, so here we use $\eta \sim 0.8$. The gas density 1 mm above the nozzle was nearly linear with solenoid valve backing pressure, as shown in Figure A.3.

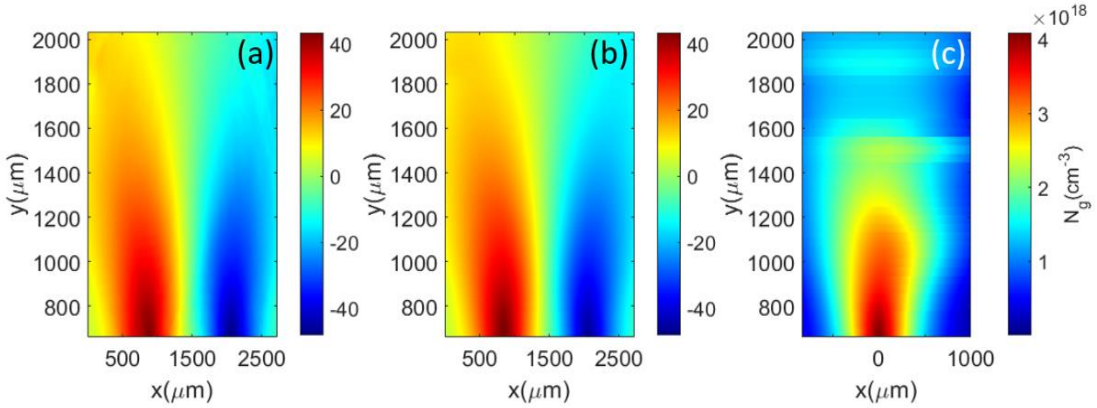

Figure A.2 Longitudinal interferometry with 1000 psi backing pressure. (a) Measured phase shift (b) Phase shift with super Gaussian fitting (c) Extracted nitrogen molecule density. The origin in this plot is the center of the nozzle exit.

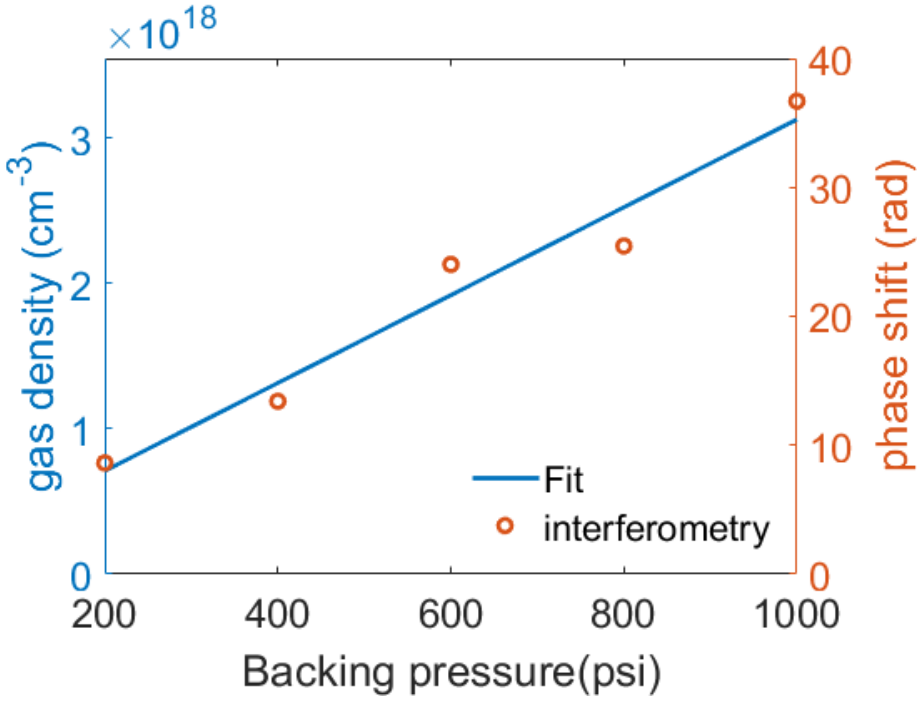

Figure A.3 axially averaged gas (N_2) density 1mm above the nozzle orifice as a function of solenoid valve backing pressure.

In the second method for gas density measurement, a high intensity J_0 Bessel beam formed a line focus in the gas jet (N_2) plume 1 mm above the nozzle orifice, generating a plasma along its entire length. The plasma fluorescence was imaged by a CCD camera (Andor Zyla 5.5) through a band pass filter (400-750 nm) with 0.1X magnification. With the gas jet off, the chamber was then backfilled with nitrogen at varying pressures and the Bessel beam again generated plasma, with the plasma fluorescence this time acting as a reference for axially uniform gas density, providing a normalization for the jet-on measurements. This enabled absolute measurement of axially dependent gas density.

In Figure A.4(a) the plasma fluorescence from the gas jet with 1000 psi valve backing pressure was compared with that from various nitrogen backfills. The gas density extracted by interpolation is shown in Figure A.4(b). The density drop near z=125 mm was due to small particles blocking the nozzle, which was later cleared and the fluorescence showed continuous intensity, as shown in Figure A.4(e). Apart from the drop at z = 125 mm, the gas density is nearly uniform with $\sim \pm 15\%$ fluctuation across the 10 cm distance. The gas density cutoff length is ~4 mm (10%~90%). The large cutoff length could stem from gas leakage or imperfect surface profile near the end of the nozzle. Another possible reason is the thick adhesive layer between the two mating pieces of the nozzle, causing lower Mach number flow than designed. These issues are to be fixed by upgraded design of nozzle profile near the end and better selection of adhesives for sealing. One of the important goals of the fluorescence measurements is to check the longitudinal uniformity of gas density. In practice, the imaging system resolution ($\sim 100\ \mu m$) is limited by its large field of view. The oscillation of fluorescence intensity near z=80 mm is due to diffraction caused by the drilled hole on the reflective axicon (see chapter 3).

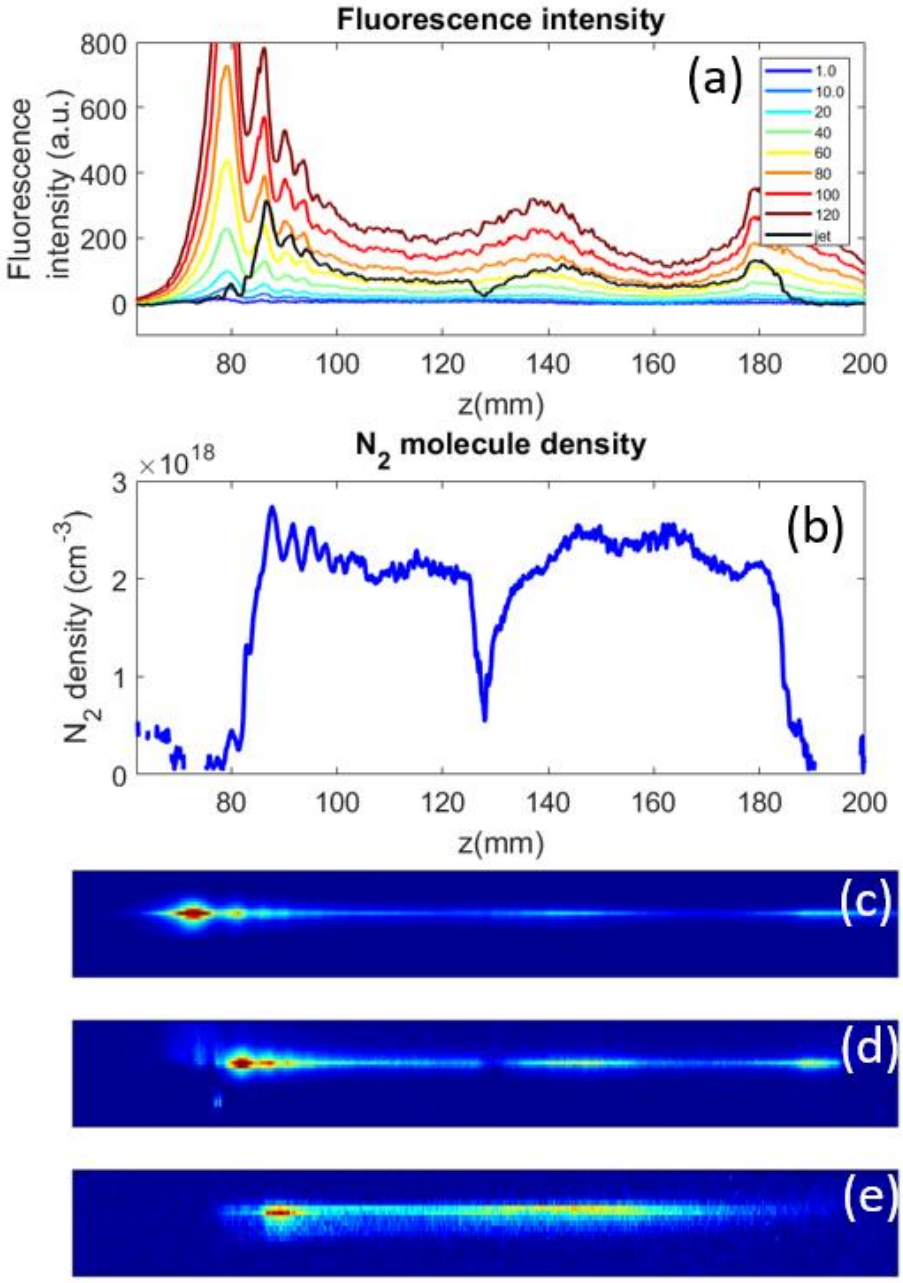

Figure A.4 Fluorescence-based measurement axially-resolved gas jet density. (a) Plasma fluorescence from the gas jet and various nitrogen backfill pressures. The legend shows the backfill nitrogen pressure. (b) Interpolated nitrogen gas density. The density dip in the middle was due to a small particle blockage in the nozzle orifice. (c) Sample fluorescence in 100 Torr nitrogen backfill (d) Sample fluorescence of nitrogen gas jet, 100 psi backing pressure (e) Sample fluorescence in hydrogen, after fixing the nozzle blockage. The nozzle axial position was slightly shifted compared with (d).

In conclusion, we have demonstrated a supersonic gas jet of 10 cm length. The jet showed a reasonably uniform longitudinal gas density profile and can reach densities of several $10^{18}\mathrm{cm}^{-3}$. Application of the 10-cm gas jet to plasma waveguide generation will be an ongoing topic of research.

Bibliography

[1] E. O. Lawrence and M. S. Livingston, Phys. Rev. **40**, 19 (1932).

[2] M. K. Gaillard, P. D. Grannis, and F. J. Sciulli, Rev. Mod. Phys. **71**, S96 (1999).

[3] W. A. Hendrickson, Trends Biochem. Sci. **25**, 637 (2000).

[4] S. Benedetti, A. Grudiev, and A. Latina, Phys. Rev. Accel. Beams **20**, 040101 (2017).

[5] R. Van Noorden, Nature **504**, 202 (2013).

[6] P. Suortti and W. Thomlinson, Phys. Med. Biol. **48**, R1 (2003).

[7] www.symmetrymagazine.org/article/a-primer-on-particle-accelerators, (2019).

[8] www6.slac.stanford.edu/about/contact-slac, (2019).

[9] T. Tajima and J. M. Dawson, Phys. Rev. Lett. **43**, 267 (1979).

[10] P. Sprangle, E. Esarey, A. Ting, and G. Joyce, Appl. Phys. Lett. **53**, 2146 (1988).

[11] S. P. D. Mangles, A. G. R. Thomas, M. C. Kaluza, O. Lundh, F. Lindau, A. Persson, F. S. Tsung, Z. Najmudin, W. B. Mori, C.-G. Wahlström, and K. Krushelnick, Phys. Rev. Lett. **96**, 215001 (2006).

[12] C. G. R. Geddes, C. Toth, J. van Tilborg, E. Esarey, C. B. Schroeder, D. Bruhwiler, C. Nieter, J. Cary, and W. P. Leemans, Nature **431**, 538 (2004).

[13] J. Faure, Y. Glinec, A. Pukhov, S. Kiselev, S. Gordienko, E. Lefebvre, J.-P. Rousseau, F. Burgy, and V. Malka, Nature **431**, 541 (2004).

[14] W. P. Leemans, A. J. Gonsalves, H.-S. Mao, K. Nakamura, C. Benedetti, C. B. Schroeder, C. Tóth, J. Daniels, D. E. Mittelberger, S. S. Bulanov, J.-L. Vay, C.

G. R. Geddes, and E. Esarey, Phys. Rev. Lett. **113**, 245002 (2014).

[15] A. J. Gonsalves, K. Nakamura, J. Daniels, C. Benedetti, C. Pieronek, T. C. H. de Raadt, S. Steinke, J. H. Bin, S. S. Bulanov, J. van Tilborg, C. G. R. Geddes, C. B. Schroeder, C. Tóth, E. Esarey, K. Swanson, L. Fan-Chiang, G. Bagdasarov, N. Bobrova, V. Gasilov, G. Korn, P. Sasorov, and W. P. Leemans, Phys. Rev. Lett. **122**, 084801 (2019).

[16] W. P. Leemans, R. Duarte, E. Esarey, S. Fournier, C. G. R. Geddes, D. Lockhart, C. B. Schroeder, C. Toth, J.-L. Vay, S. Zimmermann, S. H. Gold, and G. S. Nusinovich, AIP Conf. Proc. **1299**, 3 (2010).

[17] www.lasernetus.org, (2018).

[18] www.eli-beams.eu, (2020).

[19] www.eli-np.ro, (2019).

[20] www.eli-alps.hu, (2019).

[21] A. J. Goers, G. A. Hine, L. Feder, B. Miao, F. Salehi, J. K. Wahlstrand, and H. M. Milchberg, Phys. Rev. Lett. **115**, (2015).

[22] F. Salehi, A. J. Goers, G. A. Hine, L. Feder, D. Kuk, B. Miao, D. Woodbury, K. Y. Kim, and H. M. Milchberg, Opt. Lett. **42**, (2017).

[23] D. Guénot, D. Gustas, A. Vernier, B. Beaurepaire, F. Böhle, M. Bocoum, M. Lozano, A. Jullien, R. Lopez-Martens, A. Lifschitz, and J. Faure, Nat. Photonics **11**, 293 (2017).

[24] F. Salehi, M. Le, and H. M. Milchberg, in *Front. Opt. + Laser Sci. APS/DLS* (OSA, Washington, D.C., 2019), p. JW4A.116.

[25] P. B. Corkum, Phys. Rev. Lett. **71**, 1994 (1993).

[26] N. B. Delone and V. P. Krainov, Physics-Uspekhi **41**, 469 (1998).

[27] L. V Keldysh, Sov. Phys. JETP **20**, 1307 (1965).

[28] P. Sprangle, E. Esarey, J. Krall, and G. Joyce, Phys. Rev. Lett. **69**, 2200 (1992).

[29] L. M. Gorbunov and V. I. Kirsanov, JETP **66**, 290 (1987).

[30] P. Sprangle, E. Esarey, and A. Ting, Phys. Rev. Lett. **64**, 2011 (1990).

[31] S. V Bulanov, V. I. Kirsanov, and A. S. Sakharov, Phys. Scr. **T30**, 208 (1990).

[32] E. Esarey and W. P. Leemans, Phys. Rev. E **59**, 1082 (1999).

[33] T. M. Antonsen and P. Mora, Phys. Rev. Lett. **69**, 2204 (1992).

[34] A. Pak, K. A. Marsh, S. F. Martins, W. Lu, W. B. Mori, and C. Joshi, Phys. Rev. Lett. **104**, 025003 (2010).

[35] M. Chen, E. Esarey, C. B. Schroeder, C. G. R. Geddes, and W. P. Leemans, Phys. Plasmas **19**, 033101 (2012).

[36] L.-L. Yu, E. Esarey, C. B. Schroeder, J.-L. Vay, C. Benedetti, C. G. R. Geddes, M. Chen, and W. P. Leemans, Phys. Rev. Lett. **112**, 125001 (2014).

[37] A. Akhiezer and R. Polovin, Sov. Phys. JETP **Vol: 30**, 915 (1956).

[38] J. M. Dawson, Phys. Rev. **113**, 383 (1959).

[39] S. V. Bulanov, F. Pegoraro, A. M. Pukhov, and A. S. Sakharov, Phys. Rev. Lett. **78**, 4205 (1997).

[40] E. Esarey, C. B. Schroeder, and W. P. Leemans, Rev. Mod. Phys. **81**, 1229 (2009).

[41] E. Esarey, B. A. Shadwick, C. B. Schroeder, and W. P. Leemans, AIP Conf. Proc. **737**, 578 (2004).

[42] I. Kostyukov, E. Nerush, A. Pukhov, and V. Seredov, Phys. Rev. Lett. **103**, 175003 (2009).

[43] F. S. Tsung, W. Lu, M. Tzoufras, W. B. Mori, C. Joshi, J. M. Vieira, L. O. Silva, and R. A. Fonseca, Phys. Plasmas **13**, 056708 (2006).

[44] S. Corde, C. Thaury, A. Lifschitz, G. Lambert, K. Ta Phuoc, X. Davoine, R. Lehe, D. Douillet, A. Rousse, and V. Malka, Nat. Commun. **4**, 1501 (2013).

[45] A. G. R. Thomas, S. P. D. Mangles, Z. Najmudin, M. C. Kaluza, C. D. Murphy, and K. Krushelnick, Phys. Rev. Lett. **98**, 054802 (2007).

[46] A. J. Goers, G. A. Hine, L. Feder, B. Miao, F. Salehi, J. K. Wahlstrand, and H. M. Milchberg, Phys. Rev. Lett. **115**, 194802 (2015).

[47] D. Mitra, J. Gil, and G. I. Melikidze, Astrophys. J. **696**, L141 (2009).

[48] A. Bergmann and P. Mulser, Phys. Rev. E **47**, 3585 (1993).

[49] K. Y. Kim, I. Alexeev, and H. M. Milchberg, Appl. Phys. Lett. **81**, 4124 (2002).

[50] J. K. Wahlstrand, S. Zahedpour, and H. M. Milchberg, J. Opt. Soc. Am. B **33**, 1476 (2016).

[51] lasermatter.umd.edu/publications.html#flash_supplementary, (2018).

[52] J. van Tilborg, C. B. Schroeder, C. V. Filip, C. Tóth, C. G. R. Geddes, G. Fubiani, R. Huber, R. A. Kaindl, E. Esarey, and W. P. Leemans, Phys. Rev. Lett. **96**, 014801 (2006).

[53] S. Corde, K. Ta Phuoc, G. Lambert, R. Fitour, V. Malka, A. Rousse, A. Beck, and E. Lefebvre, Rev. Mod. Phys. **85**, 1 (2013).

[54] T. Matsuoka, C. McGuffey, P. G. Cummings, Y. Horovitz, F. Dollar, V.

Chvykov, G. Kalintchenko, P. Rousseau, V. Yanovsky, S. S. Bulanov, A. G. R. Thomas, A. Maksimchuk, and K. Krushelnick, Phys. Rev. Lett. **105**, 034801 (2010).

[55] M. Kempe and W. Rudolph, Phys. Rev. A **48**, 4721 (1993).

[56] M. Born and E. Wolf, *Principles of Optics : Electromagnetic Theory of Propagation, Interference and Diffraction of Light* (Pergamon Press, 1980).

[57] physics.nist.gov/PhysRefData/Handbook/Tables/hydrogentable3.htm, (2019).

[58] D. F. Gordon, W. B. Mori, and T. M. Antonsen, IEEE Trans. Plasma Sci. **28**, 1135 (2000).

[59] J. D. Jackson, *Classical Electrodynamics* (Wiley, 1999).

[60] J. Durnin, J. J. Miceli, and J. H. Eberly, Phys. Rev. Lett. **58**, 1499 (1987).

[61] D. McGloin and K. Dholakia, Contemp. Phys. **46**, 15 (2005).

[62] J. Arlt, V. Garces-Chavez, W. Sibbett, and K. Dholakia, Opt. Commun. **197**, 239 (2001).

[63] M. K. Bhuyan, F. Courvoisier, P. A. Lacourt, M. Jacquot, R. Salut, L. Furfaro, and J. M. Dudley, Appl. Phys. Lett. **97**, 081102 (2010).

[64] J. Dudutis, R. Stonys, G. Račiukaitis, P. Gečys, J. Lopez, K. Mishchik, B. Chassagne, C. Javaux-Leger, C. Honninger, E. Mottay, R. Kling, S. Russ, M. Wendel, J. Kleiner, D. Grossmann, and K. Bergner, 60 (2015).

[65] K.-S. Lee and J. P. Rolland, Opt. Lett. **33**, 1696 (2008).

[66] C. G. Durfee and H. M. Milchberg, Phys. Rev. Lett. **71**, 2409 (1993).

[67] H. M. Milchberg, C. G. Durfee III, and T. J. McIlrath, Phys. Rev. Lett. **75**, 2494 (1995).

[68] J. H. McLeod, J. Opt. Soc. Am. **44**, 592 (1954).

[69] J. Turunen, A. Vasara, and A. T. Friberg, Appl. Opt. **27**, 3959 (1988).

[70] N. Chattrapiban, E. A. Rogers, D. Cofield, W. T. Hill, III, and R. Roy, Opt. Lett. **28**, 2183 (2003).

[71] R. M. Herman and T. A. Wiggins, J. Opt. Soc. Am. A **8**, 932 (1991).

[72] J. Fan, Propagation of Intense Bessel Beams in Underdense Plasmas and Applications, University of Maryland, College Park, 2002.

[73] C. G. Durfee, J. Lynch, and H. M. Milchberg, Phys. Rev. E **51**, 2368 (1995).

[74] J. Arlt and K. Dholakia, Opt. Commun. **177**, 297 (2000).

[75] J. A. Davis, E. Carcole, and D. M. Cottrell, Appl. Opt. **35**, 599 (1996).

[76] S. S. R. Oemrawsingh, J. A. W. van Houwelingen, E. R. Eliel, J. P. Woerdman, E. J. K. Verstegen, J. G. Kloosterboer, and G. W. 't Hooft, Appl. Opt. **43**, 688 (2004).

[77] G. J. Swanson, *Binary Optics Technology: The Theory and Design of Multi-Level Diffractive Optical Elements* (1989).

[78] G. J. Swanson, *Binary Optics Technology: Theoretical Limits on the Diffraction Efficiency of Multilevel Diffractive Optical Elements* (1991).

[79] D. C. O'Shea, T. J. Suleski, A. D. Kathman, D. W. Prather, and Society of Photo-optical Instrumentation Engineers., *Diffractive Optics : Design, Fabrication, and Test* (SPIE, 2004).

[80] A. Grosse, M. Grewe, and H. Fouckhardt, J. Micromechanics Microengineering **11**, 257 (2001).

[81] Z. Bin and L. Zhu, Appl. Opt. **37**, 2563 (1998).

[82] A. Thaning, Z. Jaroszewicz, and A. T. Friberg, Appl. Opt. **42**, 9 (2003).

[83] P. Boucher, J. Del Hoyo, C. Billet, O. Pinel, G. Labroille, and F. Courvoisier, Appl. Opt. **57**, 6725 (2018).

[84] T. Tanaka and S. Yamamoto, Opt. Commun. **184**, 113 (2000).

[85] J. E. Morris, T. Čižmár, H. I. C. Dalgarno, R. F. Marchington, F. J. Gunn-Moore, and K. Dholakia, J. Opt. **12**, 124002 (2010).

[86] F. Courvoisier, R. Stoian, and A. Couairon, Opt. Laser Technol. **80**, 125 (2016).

[87] B. C. Platt and R. Shack, J. Refract. Surg. **17**, S573 (2001).

[88] D. Kupka, P. Schlup, and R. A. Bartels, Appl. Opt. **47**, 1200 (2008).

[89] F. Bonaretti, D. Faccio, M. Clerici, J. Biegert, and P. Di Trapani, Opt. Express **17**, 9804 (2009).

[90] S. Chatterjee and Y. P. Kumar, Appl. Opt. **50**, 6057 (2011).

[91] J. Ma, C. Pruss, R. Zhu, Z. Gao, C. Yuan, and W. Osten, Opt. Lett. **36**, 2005 (2011).

[92] H. Gao, X. Zhang, and F. Fang, Meas. Sci. Technol. **28**, 095204 (2017).

[93] M. R. Teague, J. Opt. Soc. Am. **73**, 1434 (1983).

[94] L. J. Allen and M. P. Oxley, Opt. Commun. **199**, 65 (2001).

[95] J. R. Fienup, Appl. Opt. **21**, 2758 (1982).

[96] J. R. Fienup and A. M. Kowalczyk, J. Opt. Soc. Am. A **7**, 450 (1990).

[97] J. R. Fienup, J. Opt. Soc. Am. A **4**, 118 (1987).

[98] S. Marchesini, Rev. Sci. Instrum. **78**, 011301 (2007).

[99] R. W. Gerchberg and W. O. Saxton, Optik (Stuttg). **35**, 237 (1972).

[100] H. H. Bauschke, P. L. Combettes, and D. R. Luke, J. Opt. Soc. Am. A **19**, 1334 (2002).

[101] H. Chang, P. Enfedaque, and S. Marchesini, SIAM J. Imaging Sci. **12**, 153 (2019).

[102] C. Metzler, P. Schniter, A. Veeraraghavan, and richard baraniuk, in *Proc. 35th Int. Conf. Mach. Learn.*, edited by J. Dy and A. Krause (PMLR, Stockholmsmässan, Stockholm Sweden, 2018), pp. 3501–3510.

[103] H. Zhang, Y. Chi, and Y. Liang, in *Proc. 33rd Int. Conf. Mach. Learn.*, edited by M. F. Balcan and K. Q. Weinberger (PMLR, New York, New York, USA, 2016), pp. 1022–1031.

[104] R. Chandra, Z. Zhong, J. Hontz, V. McCulloch, C. Studer, and T. Goldstein, in *2017 51st Asilomar Conf. Signals, Syst. Comput.* (IEEE, 2017), pp. 1617–1621.

[105] J. Dudutis, R. Stonys, G. Račiukaitis, and P. Gečys, Opt. Express **26**, 3627 (2018).

[106] D. Kawaguchi, M. Nakano, R. Sugio, T. Hirose, and K. Araki, US20160052088A1 (13 March 2014).

[107] R. R. Gattass and E. Mazur, Nat. Photonics **2**, 219 (2008).

[108] T. R. Clark and H. M. Milchberg, Phys. Rev. E **61**, 1954 (2000).

[109] Y. Ehrlich, C. Cohen, A. Zigler, J. Krall, P. Sprangle, and E. Esarey, Phys. Rev. Lett. **77**, 4186 (1996).

[110] P. Volfbeyn, E. Esarey, and W. P. Leemans, Phys. Plasmas **6**, 2269 (1999).

[111] E. W. Gaul, S. P. Le Blanc, A. R. Rundquist, R. Zgadzaj, H. Langhoff, and M. C. Downer, Appl. Phys. Lett. **77**, 4112 (2000).

[112] V. Kumarappan, K. Y. Kim, and H. M. Milchberg, Phys. Rev. Lett. **94**, 205004 (2005).

[113] D. J. Spence, A. Butler, and S. M. Hooker, J. Phys. B At. Mol. Opt. Phys. **34**, 4103 (2001).

[114] N. A. Bobrova, A. A. Esaulov, J.-I. Sakai, P. V. Sasorov, D. J. Spence, A. Butler, S. M. Hooker, and S. V. Bulanov, Phys. Rev. E **65**, 016407 (2001).

[115] S. P. Nikitin, T. M. Antonsen, T. R. Clark, Y. Li, and H. M. Milchberg, Opt. Lett. **22**, 1787 (1997).

[116] P. B. Corkum, N. H. Burnett, and F. Brunel, Phys. Rev. Lett. **62**, 1259 (1989).

[117] R. J. Shalloo, C. Arran, A. Picksley, A. von Boetticher, L. Corner, J. Holloway, G. Hine, J. Jonnerby, H. M. Milchberg, C. Thornton, R. Walczak, and S. M. Hooker, Phys. Rev. Accel. Beams **22**, 041302 (2019).

[118] N. Lemos, L. Cardoso, J. Geada, G. Figueira, F. Albert, and J. M. Dias, Sci. Rep. **8**, 3165 (2018).

[119] N. Lemos, T. Grismayer, L. Cardoso, G. Figueira, R. Issac, D. A. Jaroszynski, and J. M. Dias, Phys. Plasmas **20**, 063102 (2013).

[120] R. J. Shalloo, C. Arran, L. Corner, J. Holloway, J. Jonnerby, R. Walczak, H. M. Milchberg, and S. M. Hooker, Phys. Rev. E **97**, 053203 (2018).

[121] I. B. (IĂŁkov B. Zel′dovich and I. P. (ÎUriĭ P. Raĭzer, *Physics of Shock Waves and High-Temperature Hydrodynamic Phenomena* (Dover Publications, 2002).

[122] T. R. Clark and H. M. Milchberg, Phys. Rev. Lett. **78**, 2373 (1997).

[123] A. Morozov, A. Goltsov, Q. Chen, M. Scully, and S. Suckewer, Phys. Plasmas **25**, 053110 (2018).

[124] J. Fan, E. Parra, I. Alexeev, K. Y. Kim, H. M. Milchberg, L. Y. Margolin, and L. N. Pyatnitskii, Phys. Rev. E **62**, R7603 (2000).

[125] S. Gessner, E. Adli, J. M. Allen, W. An, C. I. Clarke, C. E. Clayton, S. Corde, J. P. Delahaye, J. Frederico, S. Z. Green, C. Hast, M. J. Hogan, C. Joshi, C. A. Lindstrøm, N. Lipkowitz, M. Litos, W. Lu, K. A. Marsh, W. B. Mori, B. O'Shea, N. Vafaei-Najafabadi, D. Walz, V. Yakimenko, and G. Yocky, Nat. Commun. **7**, 11785 (2016).

[126] C. W. Siders, J. L. W. Siders, A. J. Taylor, S.-G. Park, and A. M. Weiner, Appl. Opt. **37**, 5302 (1998).

[127] M. Takeda, H. Ina, and S. Kobayashi, J. Opt. Soc. Am. **72**, 156 (1982).

[128] M. Kalal and K. Nugent, Appl. Opt. **27**, 1956 (1988).

[129] N. B. Delone and V. P. Krainov, Physics-Uspekhi **41**, 469 (1998).

[130] S. Augst, D. D. Meyerhofer, D. Strickland, and S. L. Chint, J. Opt. Soc. Am. B **8**, 858 (1991).

[131] N. Lemos, T. Grismayer, L. Cardoso, J. Geada, G. Figueira, and J. M. Dias, Phys. Plasmas **20**, 103109 (2013).

[132] S. J. Yoon, J. P. Palastro, and H. M. Milchberg, Phys. Rev. Lett. **112**, 134803 (2014).

[133] B. D. Layer, A. York, T. M. Antonsen, S. Varma, Y.-H. Chen, Y. Leng, and H. M. Milchberg, Phys. Rev. Lett. **99**, 035001 (2007).

[134] A. G. York, H. M. Milchberg, J. P. Palastro, and T. M. Antonsen, Phys. Rev. Lett. **100**, 195001 (2008).

[135] D. Marcuse, *Theory of Dielectric Optical Waveguides* (Academic Press, 1991).

[136] M. V Ammosov, N. 8 Delone, and V. P. Krainov, Zh. Eksp. Teor. Fiz **91**, (2008).

[137] X. M. Tong and C. D. Lin, J. Phys. B At. Mol. Opt. Phys. **38**, 2593 (2005).

[138] F. A. Ilkov,', J. E. Decker, and S. L. Chin, J. Phys. B At. Mol. Opt. Phys **25**, 4005 (1992).

[139] G. B. Field, W. B. Somerville, and K. Dressler, Annu. Rev. Astron. Astrophys. **4**, 207 (1966).

[140] T. E. Sharp, At. Data Nucl. Data Tables **2**, 119 (1970).

[141] R. M. Herman and T. A. Wiggins, J. Opt. Soc. Am. A **8**, 932 (1991).

[142] Y. Wang, S. Yan, A. T. Friberg, D. Kuebel, and T. D. Visser, (2017).

[143] A. J. Howard, D. Turnbull, A. S. Davies, P. Franke, D. H. Froula, and J. P. Palastro, Phys. Rev. Lett. **123**, 124801 (2019).

[144] J. Fan, T. R. Clark, and H. M. Milchberg, Appl. Phys. Lett. **73**, 3064 (1998).

[145] T. Hosokai, K. Kinoshita, T. Watanabe, K. Yoshii, T. Ueda, A. Zhidokov, M. Uesaka, K. Nakajima, M. Kando, and H. Kotaki, in *Proc. Eighth Eur. Part. Accel. Conf.* (2002).

[146] H. Sheng, K. Y. Kim, V. Kumarappan, B. D. Layer, and H. M. Milchberg, Phys. Rev. E **72**, 036411 (2005).

[147] V. Kumarappan, K. Y. Kim, and H. M. Milchberg, Phys. Rev. Lett. **94**, 205004 (2005).

[148] H. . Milchberg, K. . Kim, V. Kumarappan, B. . Layer, and H. Sheng, Philos. Trans. R. Soc. A Math. Phys. Eng. Sci. **364**, 647 (2006).

[149] J. D. Anderson, *Modern Compressible Flow : With Historical Perspective*

(McGraw-Hill, 2003).

[150] K. Okamoto, *Fundamentals of Optical Waveguides* (Academic Press, 2005).